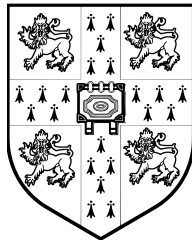


# FEEDBACK CONTROL OF OSCILLATIONS IN COMBUSTION AND CAVITY FLOWS

Simon J. Illingworth  
Magdalene College  
University of Cambridge



A dissertation submitted for the degree of  
Doctor of Philosophy  
November 2009



## PREFACE

Except where indicated below, this dissertation is the result of my own work and includes nothing which is the outcome of work done in collaboration. This dissertation is not substantially the same as any that I have submitted for a degree or diploma or other qualification at any other University.

The work reported in chapters 5 & 6 on cavity oscillations was carried out in collaboration with Professor Clarence Rowley at Princeton University.

On the subject of spelling, the author sides with the Oxford English Dictionary, who justify their consistent use of the termination *-ize* as opposed to *-ise* by observing that “some have used the spelling *-ise* in English, as in French. . . But the suffix itself, whatever the element to which it is added, is in its origin the Greek *-izein*, Latin *-izare*; and, as the pronunciation is also with *z*, there is no reason why in English the special French spelling should be followed, in opposition to that which is at once etymological and phonetic.”

This dissertation contains 50 figures, 3 tables and approximately 32,000 words.

Simon Illingworth  
11<sup>th</sup> November 2009  
Cambridge, U.K.



## ACKNOWLEDGEMENTS

Dr Aimee Morgans has been a fantastic supervisor, and I cannot thank her enough for her support, guidance, patience, and for being so generous with her time. Her contributions both to this thesis and to my happiness at Cambridge these last few years are very gratefully acknowledged. I also thank my advisor Professor Dame Ann Dowling for her time and support, and Dr Simon Stow for help with his low order model.

Over the course of my PhD, it was my great pleasure to spend two months at Princeton University, where Professor Clarence Rowley shared his time, his expertise on cavity oscillations, and his DNS code. I also thank Dr Anuradha Annaswamy, who kindly hosted me at the Massachusetts Institute of Technology and shared her great insight into adaptive control.

Financial support from the EPSRC and Rolls-Royce plc is gratefully acknowledged.

I have met some wonderful people here in Cambridge. I am very grateful to my friends for their encouragement, and for making my time in Cambridge so happy and memorable.

This thesis is dedicated to my Mum, for loving me and supporting me in everything that I have wanted to do.



## ABSTRACT

This thesis considers the control of combustion oscillations, motivated by the susceptibility of lean premixed combustion to such oscillations, and the long and expensive development and commissioning times that this is giving rise to. The controller used is both closed-loop, employing an actuator to modify some system parameter in response to a measured signal, and adaptive, meaning that it is able to maintain control over a wide range of operating conditions. The controller is applied to combustion systems with annular geometries, where instabilities can occur both longitudinally and azimuthally, and which require multiple sensors and multiple actuators for control.

One of the requirements of Lyapunov-based adaptive control which is particularly troublesome for combustion systems is then addressed: that the sign of the high-frequency gain of the open-loop system is known. We address it by using an adaptive controller which employs a Nussbaum gain, and successfully apply it experimentally to combustion oscillations in a Rijke tube.

Another type of fluid-acoustic resonance is then considered: the compressible flow past a shallow cavity. We start by finding a linear model of the cavity flow's dynamics, or its 'transfer function', which we identify from direct numerical simulations. We compare this measured transfer function to that given by a conceptual model which is based on the Rossiter mechanism, and which models each component of the flow physics separately.

We then look at using closed-loop control to eliminate these cavity oscillations. We start by designing a robust  $\mathcal{H}_2$  controller based on a balanced reduced order model of the system, the model being provided by the Eigensystem Realization Algorithm (ERA). The robust controller provides closed-loop stability over a much wider Mach number range than seen in previous studies. Finally, we look at the suitability of the adaptive controller, earlier developed for combustion oscillations, for the cavity. Based on some general properties of the cavity flow, and by using collocated control, the oscillations are eliminated at all Mach numbers tested in the range  $0.4 \leq M \leq 0.8$ .



## CONTENTS

<b>1</b>	<b>INTRODUCTION</b>	<b>1</b>
1.1	Motivation . . . . .	1
1.2	Overview . . . . .	2
<b>2</b>	<b>COMBUSTION OSCILLATIONS AND THEIR CONTROL</b>	<b>5</b>
2.1	Historical perspective . . . . .	5
2.2	Physics of combustion oscillations . . . . .	5
2.3	Control strategies . . . . .	8
2.4	Feedback control of combustion oscillations . . . . .	9
2.4.1	Adaptive feedback control . . . . .	11
2.5	Practical implementation and challenges of feedback control . . . . .	12
2.5.1	Sensors . . . . .	12
2.5.2	Actuators . . . . .	13
2.5.3	Time delays . . . . .	14
2.5.4	The origin of secondary peaks . . . . .	14
2.6	General properties of longitudinal combustion systems . . . . .	17
<b>3</b>	<b>ADAPTIVE CONTROL OF ANNULAR COMBUSTION SYSTEMS</b>	<b>21</b>
3.1	Introductory remarks on circumferential modes . . . . .	21
3.2	Open-loop transfer function for control purposes . . . . .	22
3.2.1	Modal open-loop transfer function . . . . .	24
3.3	Lyapunov adaptive control . . . . .	25
3.3.1	An adaptive controller for a class of combustion systems . . . . .	25
3.3.2	Adaptation rates . . . . .	31
3.4	Modal adaptive controller . . . . .	33
3.5	Description of the thermoacoustic network model . . . . .	35
3.6	Adaptive control of an annular combustor in LOTAN . . . . .	37
3.6.1	Combustor geometries . . . . .	37
3.6.2	Single circumferential mode . . . . .	38
3.6.3	Changing operating conditions . . . . .	40
3.6.4	Multiple unstable modes . . . . .	41
3.7	Control using fewer transducers and actuators . . . . .	43
3.8	Concluding remarks . . . . .	47

<b>4</b>	<b>ADAPTIVE CONTROL FOR UNKNOWN CONTROL DIRECTION</b>	<b>49</b>
4.1	Importance of the high-frequency gain . . . . .	49
4.1.1	Physical significance of the high-frequency gain . . . . .	50
4.1.2	Importance for feedback control . . . . .	51
4.1.3	Importance for Lyapunov-based adaptive control . . . . .	52
4.2	Adaptive control using a Nussbaum gain . . . . .	52
4.3	Nussbaum gain adaptive control applied to a Rijke tube . . . . .	54
4.3.1	Experimental arrangement . . . . .	54
4.3.2	Nussbaum adaptive controller . . . . .	55
4.4	Experimental results . . . . .	57
4.4.1	Fixed operating conditions . . . . .	57
4.4.2	Varying operating conditions . . . . .	57
4.5	Concluding remarks . . . . .	60
<b>5</b>	<b>DYNAMICS OF CAVITY OSCILLATIONS</b>	<b>61</b>
5.1	Introduction and historical perspective . . . . .	61
5.2	Cavity geometry and numerical method . . . . .	63
5.3	System identification of the cavity flow . . . . .	64
5.4	Linear models for control of cavity oscillations . . . . .	67
5.4.1	Constituent transfer functions . . . . .	68
5.4.2	Overall linear model . . . . .	73
5.4.3	High-frequency dynamics . . . . .	76
5.5	Properties of the cavity transfer function . . . . .	79
5.5.1	Transfer function zeros . . . . .	80
5.5.2	Relative degree . . . . .	82
5.6	Suitability of the adaptive controller for cavity oscillations . . . . .	85
5.7	Concluding remarks . . . . .	87
<b>6</b>	<b>FEEDBACK CONTROL OF CAVITY OSCILLATIONS</b>	<b>89</b>
6.1	Reduced order modeling for fluids . . . . .	89
6.2	Balanced reduced order modeling . . . . .	91
6.2.1	Controllability . . . . .	91
6.2.2	Observability . . . . .	92
6.2.3	Eigensystem realization algorithm . . . . .	93
6.3	Application of the ERA to the cavity flow . . . . .	96
6.4	LQG control . . . . .	97
6.4.1	Controller design . . . . .	98
6.4.2	Results . . . . .	100
6.4.3	Gain scheduling . . . . .	105
6.5	Adaptive control . . . . .	108
6.6	Concluding remarks . . . . .	109

<b>7</b>	<b>CONCLUSIONS</b>	<b>115</b>
7.1	Summary . . . . .	115
7.2	Suggestions for future work . . . . .	117
<b>A</b>	<b>GENERAL PROPERTIES OF COMBUSTION SYSTEMS</b>	<b>119</b>
<b>B</b>	<b><math>X</math> AND <math>Y</math> MATRICES</b>	<b>125</b>
<b>C</b>	<b>PROOF OF CLOSED-LOOP STABILITY FOR A NUSSBAUM GAIN</b>	<b>127</b>
<b>D</b>	<b>ADAPTATION RATES FOR THE NUSSBAUM GAIN</b>	<b>129</b>
	<b>BIBLIOGRAPHY</b>	<b>132</b>

## LIST OF FIGURES

2.1	A control volume of perfect gas within a combustor . . . . .	6
2.2	Classification of control strategies . . . . .	8
2.3	Typical feedback control arrangement for a combustion system . . . . .	10
2.4	Examples of secondary peaks seen in experimental studies . . . . .	15
2.5	General combustion system with a feedback controller . . . . .	18
3.1	Circumferential mode shapes for increasing values of $n$ . . . . .	23
3.2	Open-loop transfer function for an annular combustion system . . . . .	23
3.3	Block diagram of the adaptive controller . . . . .	29
3.4	Modification of the data vector . . . . .	30
3.5	Modal adaptive control algorithm . . . . .	35
3.6	Annular combustor geometry . . . . .	38
3.7	Bode diagram of the modal transfer function $P^{\pm 1}(s)$ . . . . .	39
3.8	Pressure mode shape of the $n = \pm 1$ spinning mode . . . . .	40
3.9	Adaptive control of the $n = \pm 1$ unstable mode . . . . .	41
3.10	Adaptive control of the $n = \pm 1$ unstable mode: zoomed-in section . . . . .	42
3.11	Adaptive control for changing flame transfer function . . . . .	43
3.12	Bode diagram of the modal transfer functions $P^0(s)$ and $P^{\pm 1}(s)$ . . . . .	44
3.13	Adaptive control of the $n = 0$ and $n = \pm 1$ unstable modes . . . . .	45
3.14	Adaptive control using fewer transducers and actuators . . . . .	46
4.1	Feedback arrangement using a feedback gain . . . . .	51
4.2	Experimental set-up of the Rijke tube . . . . .	55
4.3	Experimental results for fixed operating conditions . . . . .	58
4.4	Experimental results for varying tube length . . . . .	59
5.1	Basic configuration of a cavity flow . . . . .	62
5.2	System identification arrangement for the cavity . . . . .	65
5.3	Transfer functions measured from direct numerical simulations . . . . .	66
5.4	Linear model of the cavity flow . . . . .	68
5.5	Shear layer transfer function $G(s)$ . . . . .	70
5.6	Acoustic transfer function $A(s)$ . . . . .	71
5.7	Scattering transfer function $S(s)$ . . . . .	72

5.8	Receptivity transfer function $R(s)$ . . . . .	73
5.9	Bode diagram comparison of the open-loop transfer function . . . . .	74
5.10	Nyquist diagram comparison of the open-loop transfer function . . . . .	75
5.11	Modified linear model including a body force transfer function . . . . .	78
5.12	Bode diagram comparison of the modified open-loop transfer function . . . . .	79
5.13	Collocated control arrangement for adaptive control . . . . .	87
6.1	Open-loop Bode diagram comparison for the ERA . . . . .	97
6.2	Closed-loop cavity arrangement . . . . .	98
6.3	Bode diagram of the LQG regulator . . . . .	101
6.4	Nyquist diagram of the LQG regulator . . . . .	102
6.5	Closed-loop control using the LQG regulator at $M = 0.60$ . . . . .	103
6.6	Performance of the LQG regulator at off-design Mach numbers . . . . .	104
6.7	Time delay phase portraits of the LQG regulator . . . . .	105
6.8	Performance of the gain-scheduled LQG regulator . . . . .	107
6.9	Adaptive control for $M = 0.40$ . . . . .	110
6.10	Adaptive control for $M = 0.50$ . . . . .	111
6.11	Adaptive control for $M = 0.60$ . . . . .	112
6.12	Adaptive control for $M = 0.70$ . . . . .	113
6.13	Adaptive control for $M = 0.80$ . . . . .	114
A.1	Disturbances in a combustion chamber . . . . .	120

## LIST OF TABLES

3.1	Summary of unstable combustor's key parameters . . . . .	37
3.2	Frequencies and growth rates of the two unstable modes . . . . .	43
6.1	Corresponding fixed controller at each of the five Mach numbers . . . . .	109



# CHAPTER 1

## INTRODUCTION

### 1.1 MOTIVATION

Combustion oscillations can occur in any system where combustion takes place within an acoustic resonator, and are caused by a coupling between unsteady heat release and acoustic waves. Unsteady combustion is an efficient acoustic source (Dowling & Ffowcs Williams, 1983) and combustors tend to be highly resonant systems, which together can lead to self-excited oscillations by the following mechanism. Pressure waves, generated by unsteady heat release at the flame, reflect from the combustor boundaries and arrive back at the flame. If the phase relationship is suitable, their interaction with the flame gives rise to further unsteady heat release, which in turn generates more pressure waves.

Gas turbines, aeroengine afterburners, ramjets, boilers and furnaces are all susceptible to combustion oscillations, with the most common laboratory-scale example being an open-ended vertical tube with a heat source in the lower half, known as a Rijke tube (Rayleigh, 1945). Combustion oscillations are of particular concern, however, for the new generation of gas turbines operating under lean premixed prevaporized (LPP) conditions. LPP combustion reduces emissions of oxides of Nitrogen ( $\text{NO}_x$ ), but is especially prone to combustion oscillations (Richards & Janus, 1998).

To eliminate combustion oscillations, the coupling between unsteady heat release and pressure waves must be interrupted, and this can be achieved in a number of ways. Using feedback control – where an actuator modifies some system parameter in response to some measured signal – is one option, and allows many powerful tools from

control theory to be applied to the problem.

This thesis focuses on eliminating combustion oscillations using feedback control. The emphasis is on robust and adaptive feedback control, motivated by the requirement that any control scheme be effective over a wide range of combustor operating conditions. We then look at using feedback control methods to eliminate another type of self-excited oscillations: those induced by the compressible flow past an open cavity.

## 1.2 OVERVIEW

This thesis considers two quite different self-excited systems. What binds it together is the common challenges faced in applying feedback control – the overwhelming majority of literature for which is concerned with linear, finite-dimensional systems – to systems that are governed by the Navier-Stokes equations, a set of non-linear, partial differential equations.<sup>1</sup>

The main contributions of this thesis are as follows:

- The development of an adaptive feedback controller for unstable combustors with annular geometries, where both longitudinal and circumferential modes are possible.
- The adaptive control – demonstrated experimentally – of combustion oscillations for unknown sign of the high-frequency gain (or ‘control direction’) by using a *Nussbaum gain*.
- The identification of the linear frequency response (or ‘transfer function’) of the compressible flow past a two-dimensional cavity which is useful for feedback control design, and its comparison with a simple linear model.
- The determination of a *balanced* low-order model of the cavity flow, and its utilization to form a robust controller using  $\mathcal{H}_2$  robust control methods.
- The *adaptive* control of cavity oscillations using a Lyapunov-based adaptive controller.

---

<sup>1</sup>Clearly, combustion oscillations introduce the added complexity of flame dynamics.

Chapters 2–4 look at feedback control of combustion oscillations, whilst chapters 5 & 6 (which are self-contained) look at feedback control of cavity oscillations.

Chapter 2 collects together relevant material from the literature. We start by looking at the physics of combustion oscillations, before summarizing and categorizing methods for their control. In the latter half of the chapter we focus specifically on *feedback* control methods for combustion oscillations. We first look at the challenges and fundamental limitations of feedback control, and then at some general properties of combustion systems that are important for the adaptive feedback controller of chapter 3.

Chapter 3 focuses on adaptive feedback control of combustion systems with annular geometries. We first look at a Lyapunov-based adaptive controller previously developed for longitudinal combustion systems, before developing it further for application to annular geometries. The adaptive controller is then applied to a number of annular combustor geometries in a low-order thermoacoustic network model.

Chapter 4 looks at one of the fundamental requirements of Lyapunov-based adaptive control: that the sign of the high-frequency gain of the open-loop system is known. We first give physical significance to the high-frequency gain of a system. A novel method for adaptive stabilization without knowledge of the sign of the high-frequency gain is then introduced, before being applied experimentally to a Rijke tube.

In chapter 5 we turn our attention to feedback control of cavity oscillations. In this chapter we focus on linear models that are useful for feedback control purposes, and we do this in two ways. First, direct numerical simulations of the cavity flow are used to characterize its linear dynamics (or ‘transfer function’). Second, we compare the transfer function found in direct numerical simulations to that given by a simple linear model.

Chapter 6 first builds on chapter 5 by forming a reduced order model of the cavity flow. This model is then used for the design of an  $\mathcal{H}_2$  robust controller, which provides stability over a larger Mach number range than seen previously in the literature. Finally, we apply *adaptive* feedback control to the cavity, and see that it provides stability over an even larger range of free-stream Mach numbers.

Chapter 7 contains concluding remarks and suggestions for future work.



## CHAPTER 2

### COMBUSTION OSCILLATIONS AND THEIR CONTROL

#### 2.1 HISTORICAL PERSPECTIVE

Rayleigh (1945) was the first to describe the mechanism for combustion oscillations. Rayleigh pointed out that an acoustic wave will gain energy if heat is added in phase with pressure, but will lose energy if heat is added out of phase with pressure, and these observations constitute Rayleigh's criterion.

Many of the earliest studies of combustion oscillations were for liquid-propellant rocket motors in the 1950s and 1960s (Crocco & Cheng, 1956; Crocco, 1965), research that was motivated by the stability problems encountered in these devices. More recently, the problem of combustion stability has been encountered in low NO<sub>x</sub> gas turbine applications, where using lean premixed combustion makes the combustor especially prone to combustion oscillations (Correa, 1998; Richards & Janus, 1998), and this has motivated a great deal of research on the subject (Keller, 1995; Fleifil *et al.*, 1996; Lieuwen *et al.*, 1998; Broda *et al.*, 1998).

More details about combustion oscillations in general can be found in the review articles of McManus *et al.* (1993), Candel (2002) and Ducruix *et al.* (2003).

#### 2.2 PHYSICS OF COMBUSTION OSCILLATIONS

We now look at a generalization of Rayleigh's criterion made by Chu (1964), which looks at the energy balance within a thermoacoustic system, and includes the effect of boundary conditions. The inequality that we find provides insight into combustion oscillations and methods for their control, and was earlier used by Dowling & Morgans

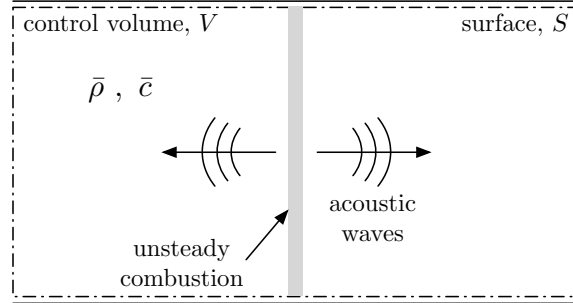


FIGURE 2.1: A control volume of perfect gas within a combustor.

(2005) for the same purpose.

Consider a perfect gas contained in a volume  $V$  and surface  $S$ , shown in figure 2.1. For simplicity, assume that the gas is linearly disturbed from rest (no mean flow), that there is no mean heat release, and that viscous forces are negligible. We use  $\rho$ ,  $\mathbf{u}$ ,  $p$ ,  $c$ ,  $q$  and  $\gamma$  to denote the density, particle velocity, pressure, speed of sound, heat release rate per unit volume and ratio of specific heat capacities respectively. An over-bar denotes a mean value, while a prime denotes a perturbation.

An inhomogeneous wave equation can then be obtained from the equations of continuity of mass and momentum:

$$\frac{1}{\bar{c}^2} \frac{\partial^2 p'}{\partial t^2} - \frac{\partial^2 p'}{\partial x^2} = \frac{\partial^2}{\partial t^2} \left( \frac{p'}{\bar{c}^2} - \rho' \right). \quad (2.1)$$

Expressing the source term on the right-hand side of (2.1) in terms of the heat release, which occurs in the combustion zone only

$$\frac{\partial^2}{\partial t^2} \left( \frac{p'}{\bar{c}^2} - \rho' \right) = \frac{\gamma - 1}{\bar{c}^2} \frac{\partial q}{\partial t},$$

integrating with respect to time, and multiplying by  $p'/\bar{c}\bar{\rho}$ , one arrives at a *local* balance equation for the acoustic energy:

$$\frac{\partial}{\partial t} \left( \frac{p'^2}{2\bar{\rho}\bar{c}^2} + \frac{1}{2}\bar{\rho}u^2 \right) + \frac{\partial p'u}{\partial x} = \frac{\gamma - 1}{\bar{\rho}\bar{c}^2} p'q.$$

A balance equation for the whole control volume is obtained by integrating over that volume, giving

$$\frac{\partial}{\partial t} \int_V \left( \frac{1}{2} \bar{\rho} u^2 + \frac{p'^2}{2\bar{\rho}c^2} \right) dV = \int_V \frac{(\gamma-1)p'q}{\bar{\rho}c^2} dV - \int_S p' \mathbf{u} d\mathbf{S}. \quad (2.2)$$

The left-hand side of (2.2) is the rate of change of the sum of the kinetic and potential energies in the volume  $V$ . The first term on the right-hand side represents the exchange of energy between combustion and acoustic waves, while the final term corresponds to energy lost by the gas in doing work on the bounding surface  $S$ . There is another source of energy loss: that due to the momentum and thermal boundary layers of the combustor (Landau & Lifshitz, 1959; Matveev, 2003) – whose influence could be important in a Rijke tube, for example – but we neglect this here.

We now see Rayleigh's criterion in a more quantitative form: for the energy of the gas to increase with time, the product  $p'q$  must be positive and such that

$$\int_V \frac{(\gamma-1)\overline{p'q}}{\bar{\rho}c^2} dV > \int_S \overline{p' \mathbf{u}} d\mathbf{S}, \quad (2.3)$$

where the over-bar denotes an average over one period of oscillation. Therefore the phase difference between  $p'$  and  $q$  must lie in the range  $[-90^\circ, +90^\circ]$ , and their product over a cycle must be sufficiently large to overcome damping, for self-excited oscillations to occur. This simplified example gives valuable insight into both the causes of combustion instabilities and ways in which they can be mitigated.

The range of phenomena leading to combustion instabilities in real gas turbines is much richer, including vortex dynamics, hydrodynamic instabilities and pulsations of the flame front – although the underlying coupling mechanism still comes from pressure waves in the vast majority of cases. For a review of these processes, see Candel (1992).

Combustion instabilities will grow until their amplitude is such that non-linear effects become important. The dominant non-linearity occurs in the heat release rate, which essentially saturates: the amplitudes of the pressure fluctuations are sufficiently small that the acoustic waves remain linear (Dowling, 1997). In some combustion sys-

tems, however, such as solid rocket motors, non-linearity of the acoustic waves can also be important (Culick, 1971).

### 2.3 CONTROL STRATEGIES

From (2.3), it is clear that there are two broad strategies for eliminating combustion oscillations: one can either target the left-hand side of (2.3) by modifying the phase relationship between  $p'$  and  $q$ , or target the right-hand side by increasing the level of damping in the system.

Techniques to suppress combustion oscillations can be categorized in many different ways, and this can lead to some ambiguity in the terms ‘passive control’ and ‘active control’. Here we choose the classification shown in figure 2.2, which is consistent with that used in active noise and vibration control. According to this definition, active control provides *external* energy to the system via an actuator, whilst passive control techniques do not. Active control can be further divided into open- and closed-loop strategies. By its very definition closed-loop control involves a feedback loop, where an actuator modifies some system parameter in response to some measured signal.<sup>1</sup> Open-loop control, although incorporating an actuator, involves no such feedback loop.

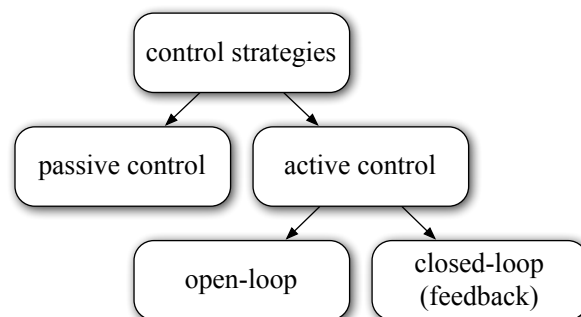


FIGURE 2.2: Classification of control strategies.

In practice, passive control is achieved either by reducing the susceptibility to in-

<sup>1</sup>Within closed-loop schemes, a further distinction can be made based on the time scales of the controller response (McManus *et al.*, 1993). We make no such distinction here, instead assuming that the controller is acting on the same time scales as the oscillations, unless otherwise stated.

stability via, for example, modifications to the combustor geometry or to the fuel injection system (Richards & Janus, 1998; Steele *et al.*, 2000), or by removing energy from the acoustic waves using, for example, acoustic liners (Eldredge & Dowling, 2003) or Helmholtz resonators (Gysling *et al.*, 2000; Bellucci *et al.*, 2004). The disadvantages of passive control are that it tends to be effective only over a limited range of operating conditions, and so instability could still occur at off-design conditions; and it is ineffective at the low frequencies at which some combustion oscillations can occur.

There have been relatively few studies of active, open-loop control of combustion oscillations. Those that exist typically use an oscillatory signal with a fixed amplitude and frequency, and the open-loop actuation is provided either by modulation of the fuel mass flow rate (Richards *et al.*, 1997; Prasanth *et al.*, 2002) or by direct excitation of the shear layer (McManus *et al.*, 1990). For a review of open-loop (and early closed-loop) control studies, see McManus *et al.* (1993).

It is important to understand that the mechanism of suppression used by open-loop control approaches is fundamentally different to that used by closed-loop control. The dynamics of a linear system cannot be changed by open-loop control, and so any open-loop actuator that modifies combustion oscillations must do so at finite amplitudes, typically at amplitudes similar to those of the oscillations being suppressed.

By contrast, closed-loop control can act to change the dynamics of a linear system, which implies that very small-amplitude actuation can be used, especially once the initial large-amplitude oscillations have been suppressed. (This is shown clearly by Tachibana *et al.* (2007), who compare open-loop and closed-loop control strategies using secondary fuel injection.) Furthermore, a rich literature exists on robust and adaptive feedback control, whose techniques can be used to design feedback controllers that are effective over a wide range of operating conditions. There are many studies of closed-loop control in the literature, and we now look at this particular strategy in more detail.

## 2.4 FEEDBACK CONTROL OF COMBUSTION OSCILLATIONS

Figure 2.3 shows the effect of a generic closed-loop control scheme on a combustion system: an actuator modifies some system parameter in response to some measured

signal. In this way, the dynamics of the overall system are modified and an unstable combustor can be stabilized.

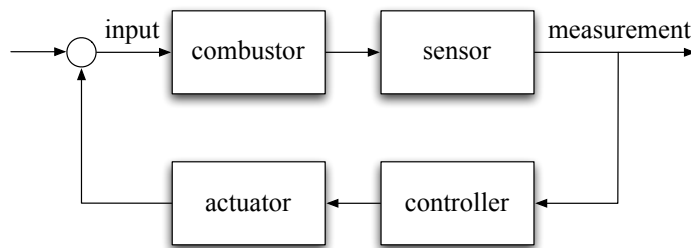


FIGURE 2.3: Typical feedback control arrangement for a combustion system.

Many studies of closed-loop control of combustion oscillations have been performed, and no attempt is made to list them all here. Rather, an overview of closed-loop control strategies in the literature is given. For an excellent recent review of the subject, see Dowling & Morgans (2005).

The concept of using closed-loop, feedback control to eliminate combustion oscillations is not new, dating back to the 1950s when it was applied theoretically to low-frequency oscillations in liquid-propellant rockets (Tsien, 1952). Closed-loop control was first applied experimentally to the Rijke tube by Dines (1983) and then by Lang *et al.* (1987) and Heckl (1988), and shortly afterwards to an afterburner (Bloxsidge *et al.*, 1988; Langhorne *et al.*, 1990) and to a turbulent ducted flame (Poinsot *et al.*, 1989). (See also Paschereit *et al.* (1998) for application to a swirl-stabilized combustor.)

Those early studies all involved very simple phase-shift or time-delay control loops. Gulati & Mani (1992) showed the inadequacies of such controllers, and demonstrated the improved closed-loop performance of a controller designed using the frequency response of the system and Nyquist techniques. Since then, model-based control techniques have been promoted (Anaswamy *et al.*, 2000; Morgans & Dowling, 2007) and many such studies have been performed. In any model-based control scheme, there are two pertinent issues to address. First, a model of the system must be available, and this can come from a physics-based model (Hathout *et al.*, 1998; Chu *et al.*, 2003; Campos-Delgado *et al.*, 2003a,b) or, less commonly, directly from experiments us-

ing system identification techniques (Tierno & Doyle, 1992; Murugappan *et al.*, 2003; Kjær *et al.*, 2006; Niederberger *et al.*, 2009). (The dynamical processes involved in large- and full-scale systems, such as combustion and turbulence, are too complex for physics-based models to be useful, and so system identification techniques are crucial for model-based control at these scales.) Such system identification techniques are useful for describing the *linear* dynamics of the combustion system. Recently, a unified framework for incorporating flame non-linearities into a model of combustion oscillations has been proposed (Noiray *et al.*, 2008). Second, a framework for the controller design must be chosen, and this has typically involved Linear Quadratic control or some variant (Hathout *et al.*, 1998; Murugappan *et al.*, 2003) or  $\mathcal{H}_\infty$  loop-shaping techniques (Tierno & Doyle, 1992; Hong *et al.*, 2000; Chu *et al.*, 2003). More recently, model predictive control techniques have been applied (Gelbert *et al.*, 2008).

#### 2.4.1 ADAPTIVE FEEDBACK CONTROL

A particularly attractive type of control scheme is adaptive control, where the controller adapts to changes in the system, thereby maintaining control over a wide range of operating conditions.

Perhaps the earliest adaptive control study for combustion oscillations was performed by Brouwer *et al.* (1991), but here the characteristic timescales of the control signal were much longer than those of the instability – a type of feedback control often referred to as trim adjustment (McManus *et al.*, 1993).

The first ‘dynamic’ adaptive controllers for combustion oscillations, using concomitant sensing and actuation timescales, were Least Mean Squares (LMS) controllers (Billoud *et al.*, 1992). Since then neural networks (Liu & Daley, 1999; Blonbou *et al.*, 2000) and observer-based adaptive controllers (Neumeier & Zinn, 1996; Sattinger *et al.*, 2000) have also been considered.

More recently, a class of self-tuning regulators has been considered (Krstic *et al.*, 1999). The adaptive tuning of the parameters of the controller is based on finding a Lyapunov function that reduces in amplitude with time when the control parameters are updated in the right way. Annaswamy *et al.* (1998) looked at such an adaptation scheme for a specific combustion system, and Evesque *et al.* (2003b) followed by

considering a scheme that was valid for a whole class of combustion systems.

Determining an accurate model of a combustion system which is useful for feedback control purposes is one of the most difficult aspects of model-based feedback control, and so the advantages of adaptive control are clear. No such model is required, and instead only minimal information about the system is needed. This is particularly true of the self-tuning regulators of Annaswamy *et al.* (1998) and Evesque *et al.* (2003b), since only some very general assumptions about the combustion system are made. We will look at this class of self-tuning regulators in more detail in chapter 3.

## 2.5 PRACTICAL IMPLEMENTATION AND CHALLENGES OF FEEDBACK CONTROL

The practical implementation of feedback control in combustion systems presents many challenges. These include turbulence and combustion, which are too complex to be modeled accurately; significant time delays brought about by the combustion process and by acoustic propagation times; and non-linear dynamics. Despite these challenges, both large- and full-scale demonstrations of closed-loop control already exist (Seume *et al.*, 1998; Moran *et al.*, 2000; Johnson *et al.*, 2001).

Two of the defining features of any feedback control system are the measurement of a feedback signal and the actuation of some system parameter, and the sensing and actuation that these necessitate are two of the greatest challenges of closed-loop control of combustion oscillations. We now look at the subjects of sensing and of actuation in more detail.

### 2.5.1 SENSORS

Experimental feedback control studies have most commonly used microphones and pressure transducers for sensing. Since pressure waves propagate throughout the entire combustor, they do not need to be placed near the high temperatures of the heat release zone (although increasing this distance will increase the acoustic time delay). They offer high bandwidth and reasonable robustness. Examples of their use range from the early experiments of Heckl (1988) and Lang *et al.* (1987) to full-scale demonstrations

by Seume *et al.* (1998) and Moran *et al.* (2000).

An alternative sensing approach is to measure the light emitted by certain progress chemicals in the flame. Such sensors are independent of mode shape unlike pressure sensors, but require optical access to the system, and may be susceptible to changes in the flame location. Examples of this approach include the earliest experimental demonstration on a Rijke tube by Dines (1983) and a diesel-fueled turbulent combustor (Hermann *et al.*, 1996).

For a review of sensors for combustion control, see Docquier & Candel (2002).

### 2.5.2 ACTUATORS

Satisfactory actuation is one of the greatest challenges for feedback control of combustion oscillations. The ideal actuator is robust and durable; has low power requirements; has high control authority to affect limit cycle oscillations; has a linear response; and has a high bandwidth to excite the system at the frequencies of the unstable modes. In reality it is very difficult to meet all of these requirements with a given actuator.

Many of the early feedback control studies used loudspeakers for actuation (Dines, 1983; Lang *et al.*, 1987; Heckl, 1988; Poinso *et al.*, 1989). These provide a linear response and high bandwidth, but suffer from insufficient robustness and prohibitive power requirements for full-scale applications.

Exploiting the chemical energy released in combustion is an efficient means of meeting power requirements for feedback control, and so actuation of the fuel mass flow rate has been employed in more recent studies. The first fuel modulation actuators were based on on-off fuel injectors (Langhorne *et al.*, 1990) and were thus non-linear. Solenoid valves have a linear response and are thus preferable, and have been used in large- and full-scale applications (Seume *et al.*, 1998). Their main drawback is their limited bandwidth and control authority. Magneto-restrictive valves have increased bandwidth (Neumeier & Zinn, 1996; Niederberger *et al.*, 2009), and show promise for application at full-scale, provided that control authority can be maintained at high frequencies.

### 2.5.3 TIME DELAYS

To see the effect of time delays, we look at a simple second-order system, which corresponds to the dynamic model of low-frequency liquid-propellant rocket instabilities that was proposed in the earliest studies of combustion oscillations (Crocco & Cheng, 1956):

$$\ddot{x}(t) + 2\zeta\omega_0\dot{x}(t) + \omega_0^2x(t) = -Fx(t - \tau), \quad (2.4)$$

where  $\omega_0$  and  $\zeta$  characterize the resonance frequency and damping of the system and  $F$  is a constant. In the rocket instabilities model,  $x(t)$  corresponds to the perturbation of the injection rate, whose characteristic equation is forced by the injection rate at an earlier time  $x(t - \tau)$ . Taking a Taylor series of the right-hand side to first order, which is more easily justified when one considers that the frequencies of interest are low, and therefore that the time scales of the characteristic equation are long, (2.4) becomes

$$\ddot{x}(t) + (2\zeta\omega_0 - F\tau)\dot{x}(t) + (\omega_0^2 + F)x(t) = 0.$$

Thus for positive  $F$ , the time delay reduces the effective damping of the system, and for  $F\tau > 2\zeta\omega_0$  the system is unstable. This simple example helps to highlight the open-loop destabilizing effect that time delays can introduce.

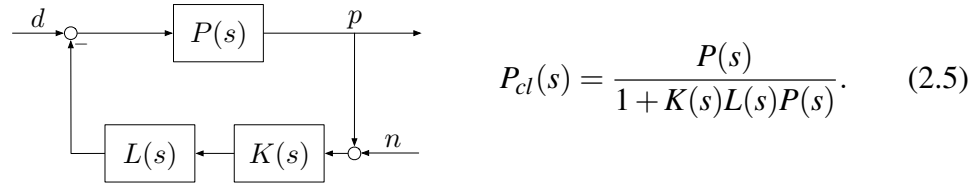
Time delays also present difficulties when feedback control is used, perhaps unsurprisingly when the actuation provided by the closed-loop controller is now based on old information. Banaszuk *et al.* (1999) use the presence of large time delays in combustion systems as an explanation of the peak splitting phenomenon seen in some closed-loop experiments. We now look at the origins of secondary peaks in more detail.

### 2.5.4 THE ORIGIN OF SECONDARY PEAKS

Secondary peaks have been observed in many closed-loop studies on combustion oscillations: two examples from Bloxside *et al.* (1988) and from Langhorne *et al.* (1990) are shown in figure 2.4. One observes that although the original oscillation is significantly reduced, new frequencies appear in the spectra when control is activated. For many of the early studies, this phenomenon can be attributed to the very simple con-

trollers used, and this was acknowledged by Langhorne *et al.* (1990), made clear via experiments by Gulati & Mani (1992), and studied in some detail for analytical models of combustors by Fleifil *et al.* (1998).

We now explain the phenomenon of secondary peaks – purely by way of a linear analysis – by considering the general feedback arrangement of a plant  $P(s)$ , a controller  $K(s)$  and an actuator  $L(s)$ , where we include a disturbance  $d$  at the input, and noise  $n$  at the output:



Here  $s = i\omega$  is the Laplace variable. We look at two possible reasons for secondary peaks. The first involves looking at the closed-loop transfer function (2.5): the closed-loop system can exhibit peaks in its frequency response if the denominator of (2.5) is close to zero at some frequency  $\omega_p$ . That is, setting  $s = i\omega_p$ , if

$$K(i\omega_p)L(i\omega_p)P(i\omega_p) \approx -1. \quad (2.6)$$

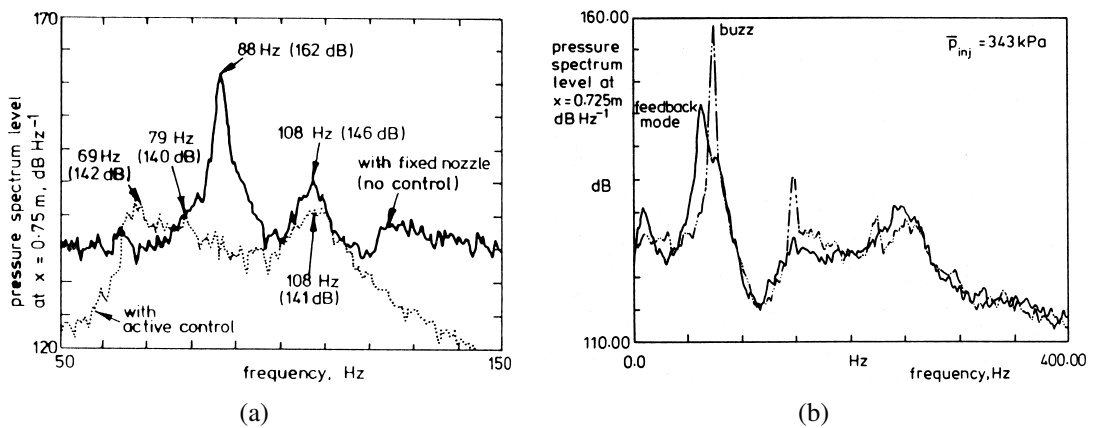


FIGURE 2.4: Examples of secondary peaks seen in experimental studies: (a) taken from Bloxside *et al.* (1988) (closed-loop case given by dashed line); and (b) taken from Langhorne *et al.* (1990) (closed-loop case given by solid line).

This secondary peak could correspond either to an unstable mode – which would then be limited in amplitude by non-linearities – or to a stable, lightly damped mode that is driven by external disturbances. This is essentially the explanation of secondary peaks given by Fleifil *et al.* (1998), and motivates the use of both a good model of the system and sophisticated controller design: if these are both available, then the ‘loop gain’  $K(s)L(s)P(s)$  can be shaped to make sure that the condition given by (2.6) is not approached. (Although when large time delays are present in the system, avoiding (2.6) at all frequencies is particularly challenging (Banaszuk *et al.*, 1999).)

There is a second, less obvious reason for secondary peaks that was first explained by Banaszuk *et al.* (1999) and by Cohen & Banaszuk (2003), who show that closed-loop amplification of disturbances will necessarily occur at some frequencies for narrow bandwidth controllers. To explain this second cause, first consider how feedback affects the amplification of disturbances  $d$ . Without control, the transfer function from a disturbance to the measured pressure is simply  $P(s)$ , whilst with feedback it becomes  $P(s)/(1 + K(s)L(s)P(s))$ . Therefore feedback modifies the open-loop transfer function by the amount

$$S(s) = \frac{1}{1 + K(s)L(s)P(s)}, \quad (2.7)$$

which is known as the sensitivity function. If  $|S(i\omega)| < 1$ , then disturbances are attenuated relative to open-loop, whereas if  $|S(i\omega)| > 1$ , then feedback amplifies disturbances. Ideally, one would like to design a compensator  $K(s)$  such that disturbances are attenuated at all frequencies,  $|S(i\omega)| < 1$ , and one may hope that with a good model of the system and a well-designed controller, this is possible. Unfortunately, Bode’s integral rule dictates that it is not. Under some quite general assumptions, Bode showed that a decrease in the sensitivity over one frequency range must be balanced by an increase in sensitivity over some other frequency range. More precisely, for a system with a relative degree of at least two,<sup>1</sup> Bode’s integral rule states that

$$\int_0^\infty \log |S(i\omega)| d\omega = \pi \sum_k \operatorname{Re}(p_k), \quad (2.8)$$

where  $p_k$  are the unstable poles of  $K(s)L(s)P(s)$ . Therefore for a stable plant, any

<sup>1</sup>The relative degree of a transfer function is defined in § 2.6 (equation (2.9)).

negative area ( $|S(i\omega)| < 1$ ) in the log-linear plot of  $S(i\omega)$  versus  $\omega$  must be balanced by a positive area ( $|S(i\omega)| > 1$ ) at some other frequency. For an unstable plant,  $\sum \text{Re}(p_k) > 0$ , and the situation is even worse.

Bode's area rule (2.8) is a fundamental limit of feedback control and, whilst not a problem in itself, is made a problem by actuators with limited bandwidth. For an actuator with unlimited bandwidth, (2.8) poses no problem, since the positive sensitivity can be spread over a large frequency range. If the actuator  $L(s)$  has limited bandwidth, however, then  $\log |S(i\omega)|$  necessarily approaches zero at high frequencies, and any positive  $\log |S(i\omega)|$  must occur within the bandwidth of the actuator. As a result any actuator, as well as providing excitation at the frequency of open-loop oscillations, ideally needs sufficient bandwidth so that the implications of (2.8) can be 'spread out' over a large frequency range.

If this is not possible, then secondary peaks can occur, even if an accurate model of the combustor is available, and even if a well-designed controller is used. This second source of secondary peaks, unlike the first, is not well-documented in the literature, but it is likely to be a problem when limited-bandwidth fuel flow actuators are used for control.

## 2.6 GENERAL PROPERTIES OF LONGITUDINAL COMBUSTION SYSTEMS

We now look at some general properties of longitudinal combustion systems which are useful for feedback control purposes. These properties were derived by Evesque *et al.* (2003b), and we will use them again in chapter 3 for the development of an adaptive controller for annular combustor geometries.

Figure 2.5 shows a general (longitudinal) combustion system fitted with a closed-loop controller. For feedback control, we assume that the feedback signal is a pressure measurement at some point in the combustor, and that modulation of the fuel mass flow rate is used for actuation.

Including the actuator in the open-loop transfer function of such a combustor, Evesque *et al.* (2003b) made four non-restrictive assumptions about the combustor's open-loop dynamics:

- (i) the pressure reflection coefficients at the upstream and downstream boundaries

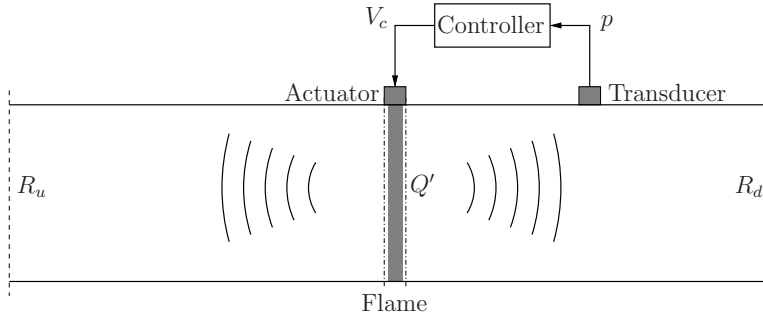


FIGURE 2.5: General combustion system with a feedback controller.

of the combustor satisfy

$$|R_u(s)| < 1, \quad |R_d(s)| < 1,$$

i.e. the amplitude of a reflected wave at a boundary is smaller than the amplitude of the incoming wave.

- (ii) the flame has stable dynamics, i.e. instability only occurs because of interactions between the flame and the combustor acoustics, and not because of any hydrodynamic instabilities of the flame itself.
- (iii) the flame response has a limited bandwidth.
- (iv) the actuator dynamics has a relative degree not exceeding two and has no right-half plane zeros.

By using a wave expansion of the acoustic field in the combustor, and by approximating the time delays in the system using Padé approximants, Evesque formed an open-loop transfer function for a longitudinal combustor of the form

$$P(s) = P_o(s)e^{-s\tau},$$

where  $P_o(s)$  is a rational approximation to the delay-free part of  $P(s)$  and can be written as the ratio of two monic polynomials:

$$P_o(s) = g_o \frac{N_P(s)}{D_P(s)}.$$

Here  $g_o$  is the high-frequency gain of  $P_o(s)$ . The *relative degree*  $n^*$  of  $P_o(s)$  is then defined as

$$n^*[P_o(s)] = \deg[D_P(s)] - \deg[N_P(s)], \quad (2.9)$$

which corresponds to the number of poles of  $P_o(s)$  minus the number of its zeros.

Three properties of any actuated combustion system meeting assumptions (i–iv) were then derived by Evesque:

PROPERTY 2.1. The zeros of  $P(s)$  are stable (i.e. in the left half-plane).

PROPERTY 2.2. The sign of the high-frequency gain of  $P(s)$  is given by the sign of the high-frequency gain of the actuator transfer function.

PROPERTY 2.3. The relative degree of  $P(s)$  is given by the relative degree of the actuator transfer function.

More details of the approach taken by Evesque *et al.* (2003b) – together with some development of the approach for annular combustor geometries which is important for chapter 3 – is given in appendix A.



## CHAPTER 3

### ADAPTIVE CONTROL OF ANNULAR COMBUSTION SYSTEMS

In this chapter, an adaptive feedback controller derived using Lyapunov's direct method is developed for axisymmetric annular combustion systems. For such systems, multiple sensors and multiple actuators are needed and thus straightforward single-input single-output approaches for longitudinal modes are no longer valid. The adaptive controller is well-suited to real engine environments for three reasons: it is able to identify and control both longitudinal and circumferential modes in annular combustors; it can adapt to large changes in the engine's operating conditions; and it does not require prior characterization of the system.

The adaptive feedback controller is implemented computationally in a low-order thermoacoustic network model (LOTAN) of an annular combustor and demonstrated in time domain simulations. The adaptive controller stabilizes two different combustion systems: one for which a circumferential instability only is present, and one with both a circumferential and a longitudinal instability. The controller retains control following a large change in the combustor operating conditions by re-tuning its adaptive parameters. Finally, a more easily implemented control arrangement with fewer transducers and actuators is investigated, and it is seen that closed-loop stability is still achieved.

#### 3.1 INTRODUCTORY REMARKS ON CIRCUMFERENTIAL MODES

For a longitudinal combustor geometry, only plane waves transport acoustic energy, and the pressure perturbation field (for example) can be written as a linear combination

of upstream- and downstream-traveling waves:

$$p'(x, t) = A_{\pm} e^{i\omega t + ik_{\pm} x},$$

where  $x$  is the axial coordinate.  $A_+$  represents a downstream-propagating wave and  $A_-$  represents an upstream-propagating wave, and  $k_+$  and  $k_-$  are the corresponding wave numbers. For such a geometry, one actuator and one sensor suffice for feedback control purposes. (The sensor must be axially well-placed to avoid nodes of the pressure mode shape.)

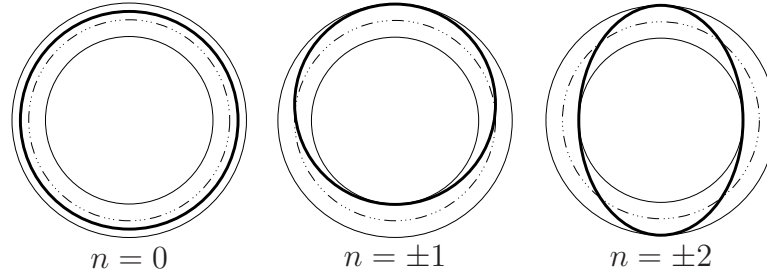
For an annular combustor geometry, we must also consider azimuthal and radial perturbations. For the annular geometries of interest in this chapter, the annular gap is small, and the radial dependence can be ignored (Stow *et al.*, 2002). Then the pressure perturbation field can be described by

$$p'(x, \theta, t) = A_{\pm} e^{i\omega t + ik_{\pm} x + in\theta},$$

where  $\theta$  is the azimuthal angle and  $n$  is the circumferential mode number. This introduces the possibility of circumferential modes: typical mode shapes are shown in figure 3.1. An  $n = 0$  mode corresponds to a longitudinal mode with no circumferential dependence, and increasing  $n$  corresponds to increasing circumferential wave number. For circumferential modes, the pressure mode shape may spin in time, or may be located at a fixed azimuthal angle, and therefore one cannot guarantee that a single sensor is not at a node. Similarly, one cannot guarantee that a single actuator will find itself in a useful position for control. From these observations it is clear that multiple sensors and multiple actuators are required for circumferential modes.

### 3.2 OPEN-LOOP TRANSFER FUNCTION FOR CONTROL PURPOSES

Figure 3.2 shows the open-loop linear transfer function for a combustion system including actuator (where again  $s = i\omega$  is the Laplace variable). Although this transfer function is not needed explicitly by the adaptive controller that we will develop, we introduce it here to make clear the Multi-Input Multi-Output (MIMO) nature of the

FIGURE 3.1: Circumferential mode shapes for increasing values of  $n$ .

problem for annular combustors, before introducing a modal equivalent of this transfer function in § 3.2.1.

Fuel valves will be used for actuation, since these are the most practical actuators for large- and full-scale applications, and pressure transducers will be used for sensing. For the annular combustor geometries that we will consider, several fuel valves and several pressure transducers are spaced azimuthally around the combustor's circumference. Then the overall open-loop transfer function is between the vector of actuator voltages  $\mathbf{V} = [V_1 \dots V_B]^T$  and the vector of transducer pressure measurements  $\mathbf{p} = [p_1 \dots p_T]^T$ , where  $B$  is the number of burner ducts and  $T$  is the number of pressure transducers. Referring to figure 3.2,  $f^\nabla$ ,  $\phi^\nabla$ ,  $Q^\nabla$  and  $a^\nabla$  represent the fractional change in the fuel mass flow rate, equivalence ratio, heat release rate and air mass flow rate respectively. Bold type is used (as it is for  $\mathbf{V}$  and  $\mathbf{p}$ ) to denote the vector-valued parameters  $\mathbf{f}^\nabla$ ,  $\phi^\nabla$ ,  $\mathbf{Q}^\nabla$  and  $\mathbf{a}^\nabla$  (all of dimension  $B$ ). Since all of the system inputs and outputs are vectors, the four constituent transfer functions are matrices:  $L(s)$ ,  $F(s)$ , and  $H(s)$  are of dimension  $B \times B$ , whilst  $G(s)$  is of dimension  $T \times B$ . The overall open-loop

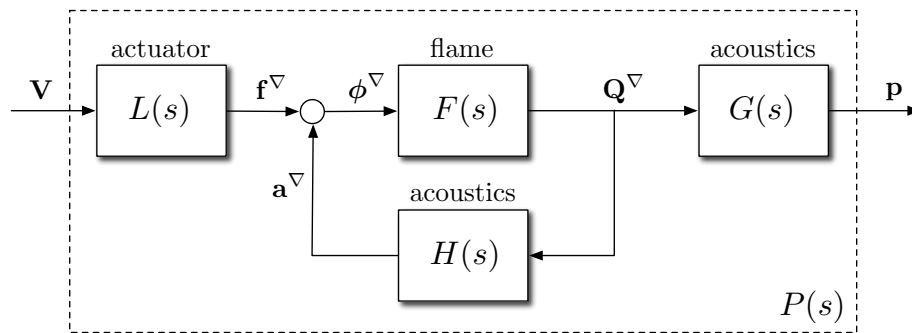


FIGURE 3.2: Open-loop transfer function for an annular combustion system.

transfer function is then

$$P(s) = G(s)(I + F(s)H(s))^{-1}F(s)L(s) \quad (3.1)$$

and has dimension  $T \times B$ . For small perturbations, the fractional change in equivalence ratio  $\phi^\nabla$  is related to the fractional change in fuel mass flow rate  $f^\nabla$  and the fractional change in air mass flow rate  $a^\nabla$  by  $\phi^\nabla = f^\nabla - a^\nabla$ .<sup>1</sup>

### 3.2.1 MODAL OPEN-LOOP TRANSFER FUNCTION

The adaptive controller that we will develop can be applied to Single-Input Single-Output (SISO) systems. The transfer function given by figure 3.2 and equation (3.1), however, has potentially many inputs and many outputs, and we remedy this by developing a *modal* transfer function and a corresponding modal adaptive controller. This simplifies the control problem from one for the MIMO system in figure 3.2 to one for a SISO system, and relies on the combustor's being axisymmetric and therefore having decoupled modes. Morgans & Stow (2007) show that this modal transfer function is given by

$$P^n(s) = \frac{p^n(s)}{V^n(s)} = \frac{L_b(s)F_b(s)G^n(s)}{B[1 + F_b(s)H^n(s)]}, \quad (3.2)$$

$F_b(s)$  is the flame transfer function for a given burner  $b$  (which are forcibly all identical for an axisymmetric combustor), whilst  $L_b(s)$  is the actuator transfer function for a given burner  $b$  (assumed to be all identical).

Equation (3.2) for the modal transfer function  $P^n(s)$  is very similar to that given by (3.1) for the single-input single-output case, which becomes

$$P(s) = \frac{p(s)}{V(s)} = \frac{L(s)F(s)G(s)}{1 + F(s)H(s)}. \quad (3.3)$$

It is for this single-input single-output case that Evesque *et al.* (2003b) derived the three properties of longitudinal combustion systems (summarized in § 2.6) that are useful for feedback control purposes, and upon which the proof of stability for the

<sup>1</sup>When normalized,  $\phi = (f/a)/(f/a)_{\text{stoich}}$  becomes  $1 + \phi^\nabla = (1 + f^\nabla)/(1 + a^\nabla)$ , which for small perturbations is simply  $\phi^\nabla = f^\nabla - a^\nabla$ .

adaptive controller to be introduced relies.

Therefore before developing an adaptive controller for circumferential modes, we must first ask if the modal transfer function (3.2) satisfies those same properties that are satisfied in the SISO case (3.3). This question is addressed in appendix A, where it is shown that the three properties derived by Evesque *et al.* (2003b) still hold for the modal transfer function, if the additional assumption is made that the frequencies of interest are well above the cut-off frequency.<sup>1</sup> This extra assumption is used to show that all of the zeros of  $P^n(s)$  are in the left half-plane. (Furthermore, for the two combustor geometries that we will consider, we will see that all zeros of the open-loop systems are in the left half-plane, and so Evesque's property 2.1 concerning the zeros is satisfied.)

### 3.3 LYAPUNOV ADAPTIVE CONTROL

The term adaptive control can be used to refer to many different control strategies (Åström, 1987), but they all share the common goal of controlling dynamical systems whose characteristics are not completely known.

Lyapunov-based adaptive control – so-called because of its foundations in Lyapunov stability theory – is one such scheme for the adaptive stabilization of unknown systems, and has found diverse applications including ship steering, flight control systems and flexible structures (Åström, 1983; Harris & Billings, 1981).

We now look at a Lyapunov-based adaptive controller for the adaptive stabilization of combustion oscillations. For completeness, we first look at the specific case of adaptive control of the class of combustion systems studied by Evesque *et al.* (2003b). This adaptive controller is valid for longitudinal combustors, where one pressure transducer and one actuator suffice for control. We then develop the controller further for application to annular combustion systems with axisymmetric geometries.

#### 3.3.1 AN ADAPTIVE CONTROLLER FOR A CLASS OF COMBUSTION SYSTEMS

Annaswamy *et al.* (1998) looked at self-tuning regulators (also known as model-based

---

<sup>1</sup>The cut-off frequency is the frequency below which the acoustic modes are attenuated with distance and carry no acoustic power – see appendix A for more details.

adaptive controllers) for a specific longitudinal combustion system: for such systems, one burner valve and one axially well-placed pressure transducer suffice for control. It was then shown (Evesque *et al.*, 2003b) that this control structure could be applied to a whole class of combustion systems. Evesque *et al.* (2003a) extended the algorithm to account for large time delays in the system by including a *Smith*-type controller (Smith, 1959): we will confine our attention to the algorithm without Smith controller here.

We consider an unstable open-loop transfer function (including actuator)  $P(s)$  which can be stabilized using feedback control, and we denote this closed-loop stabilized transfer function by  $P_{cl}^*(s)$ . It can be shown from root-locus arguments that, for the class of combustion systems studied by Evesque *et al.* (2003b), a first-order compensator of the form

$$K(s) = k_c \frac{s + z_c}{s + p_c} \quad (3.4)$$

is sufficient to provide closed-loop stability. The adaptive feedback controller that we now consider finds stabilizing parameters for this first-order compensator. The derivation of such an adaptive control algorithm relies on  $P_{cl}^*(s)$  being *Strictly Positive Real* (SPR).

If  $P_{cl}^*(s)$  is SPR, it is possible to form a positive-definite Lyapunov function which depends on the states (in a state-space sense) of  $P_{cl}^*(s)$  and a vector of control parameters. Because the Lyapunov function is positive-definite, it can be thought of as an energy function. The time derivative of the Lyapunov function is guaranteed to be negative if the time derivative of the control parameters obeys a certain rule: this provides the updating rule for the control parameters. When this updating rule is used, the Lyapunov function is guaranteed to decrease monotonically in time and the control parameters are guaranteed to converge to a stabilizing set. The existence of such a Lyapunov function – which depends on  $P_{cl}^*(s)$  being SPR – is crucial for obtaining an adaptation algorithm which guarantees stability.

$P_{cl}^*(s)$  being SPR requires that:

- (i)  $P_{cl}^*(s)$  has no right half-plane zeros (i.e. the closed-loop system is minimum phase).

- (ii) The high-frequency gain of  $P_{cl}^*(s)$  is positive.
- (iii)  $\text{Re}[P_{cl}^*(s)] > 0, \forall s$ , which is equivalent to the phase of  $P_{cl}^*(s)$  lying in the range  $-90^\circ < \angle[P_{cl}^*(s)] < +90^\circ$ .

For a more rigorous definition of an SPR transfer function, see Narendra & Annaswamy (1989).

These requirements on the closed-loop stabilized system  $P_{cl}^*(s)$  translate into requirements on the *open-loop* system  $P(s)$ . We now make these requirements on  $P(s)$  clear, and show how they relate to the general properties of combustion systems that were derived by Evesque *et al.* (2003b) and that were summarized in § 2.6.

- (i)  $P_{cl}^*(s)$  has no right half-plane zeros. Since feedback has no effect on the zeros of a transfer function, this means that  $P(s)$  must also have no right half-plane zeros. Evesque *et al.* (2003b) showed that this was met for longitudinal combustors (property 2.1), and in appendix A it is shown that this is also true of circumferential modes when the frequencies of interest are well above the cut-off frequency. We will also see that the transfer functions of the combustors studies in this chapter contain no right half-plane zeros. (For extension to combustion systems with right half-plane zeros, see Morgans & Annaswamy (2008).)
- (ii) *The high-frequency gain of  $P_{cl}^*(s)$  is positive.* For any feedback controller,  $P(s)$  and  $P_{cl}^*(s)$  have the same high-frequency gain. Therefore the high-frequency gain of  $P(s)$  must also be positive, and this corresponds to Evesque's property 2.2. For adaptive control, however, we will see that it is enough to know the sign of the high-frequency gain of  $P(s)$ . (The case where the sign of the high-frequency gain is unknown is the focus of chapter 4.)
- (iii)  $\text{Re}[P_{cl}^*(s)] > 0, \forall s$ . This places an upper bound on the relative degree of  $P_{cl}^*(s)$ . Since  $P(s)$  and  $P_{cl}^*(s)$  have the same relative degree, this upper bound also applies to  $P(s)$ . An SPR transfer function has a relative degree of at most one. By modifying the adaptive controller, however, it is possible to apply it to systems with a relative degree not exceeding two, and this corresponds to Evesque's property 2.3.

We now look at the adaptive control problem for two cases: first for systems with a relative degree of one; and then for systems with a relative degree not exceeding two, where the relative degree  $n^*$  of a transfer function  $P(s)$  is defined as the number of poles of  $P(s)$  minus the number of zeros (see equation (2.9)).

*Relative degree  $n^* = 1$*

When  $n^*[P(s)] = 1$  then  $n^*[P_{cl}^*(s)] = 1$  as well and  $P_{cl}^*(s)$  is SPR.<sup>1</sup> The adaptive controller for such a system is shown in figure 3.3(a). We now define the control vector  $\mathbf{k}(t) = [k_1(t) \ k_2(t)]^T$  and the data vector  $\mathbf{d}(t) = [p(t) \ V_z(t)]^T$ , where  $V_z(t) = \frac{V(t)}{s+z_c}$ , with  $z_c$  chosen and fixed. By defining  $\tilde{\mathbf{k}} = \mathbf{k} - \mathbf{k}^*$ , where  $\mathbf{k}^*$  denotes the  $\mathbf{k}$  for which the closed-loop system is stabilized, the total feedback signal can be written as  $\mathbf{k}^T \mathbf{d} = \mathbf{k}^{*T} \mathbf{d} + \tilde{\mathbf{k}}^T \mathbf{d}$ . Using this expression, the closed-loop system can be represented as shown in figure 3.3(b). Therefore the closed-loop system  $P_{cl}(s)$  at time  $t$  is identical to the closed-loop *stabilized* system  $P_{cl}^*(s)$  with input disturbance  $-\tilde{\mathbf{k}}^T \mathbf{d}$ , which means that  $p(t) = P_{cl}^*(s)[- \tilde{\mathbf{k}}^T \mathbf{d}(t)]$ . In state-space form, this can be written as

$$\begin{aligned} \dot{\mathbf{x}}(t) &= A\mathbf{x}(t) + B[-\tilde{\mathbf{k}}^T(t)\mathbf{d}(t)] \\ p(t) &= C\mathbf{x}(t). \end{aligned} \quad (3.5)$$

From lemma 2.4, Narendra & Annaswamy (1989), the strict positive realness of  $P_{cl}^*(s)$  assures the existence of a matrix  $Q = Q^T > 0$  which satisfies

$$\begin{aligned} A^T Q + QA &= -R \\ QB &= C^T, \end{aligned} \quad (3.6)$$

where  $R$  also satisfies  $R = R^T > 0$ .

We now want to find a *Lyapunov function*  $\Lambda(t)$  that is strictly positive and that decays in time when the control parameters  $\mathbf{k}(t)$  are updated correctly. The existence of such a function will be used to prove the asymptotic stability of the closed-loop

<sup>1</sup>For the third condition  $\text{Re}[P_{cl}^*(s)] > 0$ , the pole and zero pairs must also interlace in frequency.

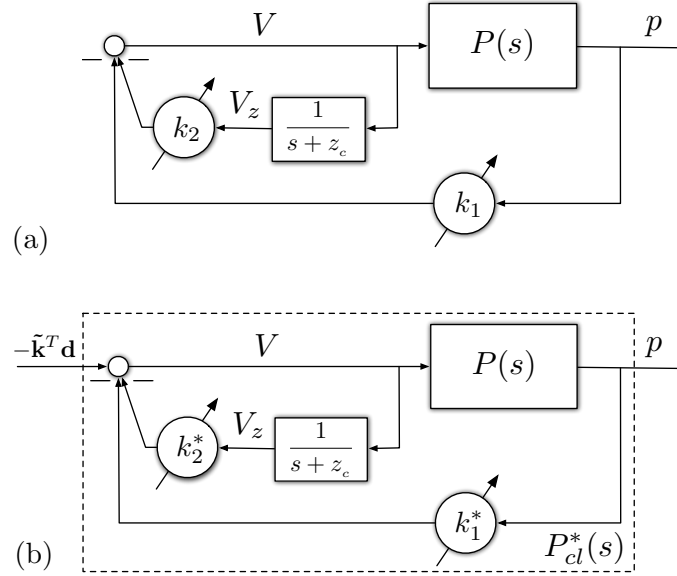


FIGURE 3.3: Block diagram of the adaptive controller: (a) the original block diagram, and (b) the equivalent closed-loop stabilized system  $P_{cl}^*(s)$  with input disturbance  $-\tilde{\mathbf{k}}^T \mathbf{d}$ .

system. We choose this function to be quadratic in both  $\mathbf{x}(t)$  and  $\tilde{\mathbf{k}}(t)$ :

$$\Lambda(t) = \mathbf{x}(t)^T Q \mathbf{x}(t) + \tilde{\mathbf{k}}^T(t) \tilde{\mathbf{k}}(t) \geq 0.$$

Evaluating the time derivative of  $\Lambda(t)$  using (3.5) and (3.6) gives

$$\dot{\Lambda}(t) = -\mathbf{x}^T(t) R \mathbf{x}(t) + 2\tilde{\mathbf{k}}^T(t) [\dot{\tilde{\mathbf{k}}}(t) - p(t)\mathbf{d}(t)],$$

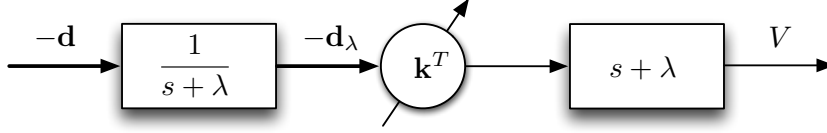
and  $-\mathbf{x}^T(t) R \mathbf{x}(t) \leq 0$ , so choosing the updating rule and control law

$$\dot{\tilde{\mathbf{k}}}(t) = p(t)\mathbf{d}(t) \tag{3.7a}$$

$$V(t) = -\mathbf{k}^T(t)\mathbf{d}(t) \tag{3.7b}$$

ensures that  $\dot{\Lambda}(t) \leq 0$ . It follows that  $\tilde{\mathbf{k}}(t)$  and  $\mathbf{x}(t)$  are bounded. Now (3.5) shows that  $\dot{\mathbf{x}}(t)$  is bounded. Finally lemma 2.12, Narendra & Annaswamy (1989) shows that  $\mathbf{x}(t)$  and therefore  $p(t)$  are guaranteed to converge asymptotically to zero.

In all of the above we have assumed that the high-frequency gain of the open-loop

FIGURE 3.4: Modification of the data vector  $\mathbf{d}$ .

system is positive. If the high-frequency gain of the open-loop system is negative, then the SPR arguments can be applied to  $-P_{cl}^*(s)$  instead. Then a more general updating rule for the adaptive parameters  $\mathbf{k}(t)$  is given by

$$\dot{\mathbf{k}}(t) = \text{sgn}(g_o)p(t)\mathbf{d}(t), \quad (3.8)$$

where  $g_o$  is the high-frequency gain of  $P(s)$ .

*Relative degree  $n^* = 2$*

The third SPR condition  $\text{Re}[P_{cl}^*(s)] > 0$  can only be met by  $n^* = 1$  systems. Therefore for  $n^* = 2$  systems,  $P_{cl}^*(s)$  is not SPR. For the right choice of  $\lambda$ , however, the transfer function  $(s + \lambda)P_{cl}^*(s)$  is SPR. Therefore Annaswamy *et al.* (1998) proposed modifying the data vector  $\mathbf{d}(t)$  as shown in figure 3.4. This modification makes the closed-loop system SPR (whilst avoiding explicit differentiation of the data vector  $\mathbf{d}(t)$ ), and results in a modified updating rule and control law

$$\dot{\mathbf{k}}(t) = \text{sgn}(g_o)p(t)\mathbf{d}_\lambda(t) \quad (3.9a)$$

$$V(t) = -\mathbf{k}^T(t)\mathbf{d}(t) - \dot{\mathbf{k}}^T(t)\mathbf{d}_\lambda(t), \quad (3.9b)$$

where  $\mathbf{d}_\lambda(t)$  is the modified data vector  $\mathbf{d}_\lambda(t) = \frac{1}{s+\lambda}\mathbf{d}(t)$ .

If  $\mathbf{k}$  were held fixed, then both controllers (3.7) and (3.9) would correspond to the first-order compensator

$$K(s) = k_1 \frac{s + z_c}{s + (k_2 + z_c)}.$$

Comparing this with (3.4), we see that  $k_1(t)$  acts to tune the gain of the adaptive controller, that  $k_2(t)$  acts to tune the position of the controller's pole, and that choosing  $z_c$

corresponds to specifying the controller's zero.

This adaptive controller has been applied previously to plane modes in a longitudinal combustor, where one fuel valve and one pressure transducer suffice for control (Evesque, 2000; Evesque *et al.*, 2003b; Riley *et al.*, 2004). We will develop this controller for circumferential instabilities in axisymmetric annular combustors, where multiple fuel valves and multiple pressure transducers are required for control. First, though, we derive expressions for the controller's *adaptation rates*.

### 3.3.2 ADAPTATION RATES

For the adaptive control of real systems, some command over the rate of adaptation of the controller is required: this can be achieved by introducing adaptation rates in (3.9a) to give

$$\dot{\mathbf{k}}(t) = \mathbf{\Gamma} \text{sgn}(g_o) p(t) \mathbf{d}_\lambda(t), \quad (3.10)$$

where  $\mathbf{\Gamma} = \text{diag}(\gamma_1 \ \gamma_2)$  is a diagonal matrix containing the *adaptation rates*. Adaptive control may at this point appear to be a Sisyphean task when the requirement to specify  $k_1$  and  $k_2$  has been replaced by the requirement to choose two new parameters  $\gamma_1$  and  $\gamma_2$ . However, the permissible range of values for  $\gamma_1$  and  $\gamma_2$  is several orders of magnitude greater than that for  $k_1$  and  $k_2$ . Furthermore, expressions for  $\gamma_1$  and  $\gamma_2$  which are functions of known parameters only will now be developed.

The adaptation rates can be set by specifying the desired speed of adaptation (Yildiz *et al.*, 2007). If the adaptive parameters start at zero, then this corresponds to  $3\tau_n$  for a 5% band around the set point (where  $\tau_n$  is the period of the unstable mode):

$$\begin{aligned} |\dot{k}_1(t)| &= \frac{|k_1^*|}{3\tau_n} = \left| \gamma_1 p(t) \frac{p(t)}{s + \lambda} \right| \\ |\dot{k}_2(t)| &= \frac{|k_2^*|}{3\tau_n} = \left| \gamma_2 p(t) \frac{V_z(t)}{s + \lambda} \right|. \end{aligned}$$

Therefore at the instability's frequency,  $s = i\omega_n$ ,

$$\gamma_1 = \frac{|k_1^*| |i\omega_n + \lambda|}{3\tau_n \hat{p}^2}$$

$$\gamma_2 = \frac{|k_2^*| |i\omega_n + \lambda|}{3\tau_n |\hat{p} \hat{V}_z|},$$

where  $\hat{p}$  and  $\hat{V}_z$  are characteristic values of  $p(t)$  and  $V_z(t)$  respectively. Using an order of magnitude analysis, one can arrive at expressions for the adaptation rates in terms of the known parameters  $k_1^*$ ,  $\omega_n$ ,  $z_c$  and  $\hat{p}$ . (It suffices to know only the order of magnitude of each of these parameters.)

$\lambda$  and  $\omega_n$  will be comparable in size, so we make the approximation  $|i\omega_n + \lambda| \simeq \omega_n$ , giving

$$\gamma_1 = \frac{|k_1^*| \omega_n^2}{6\pi \hat{p}^2}.$$

Determining  $\gamma_2$  is a little more involved, since expressions for  $k_2^*$  and  $\hat{V}_z$  are required. Using

$$V_z(t) = \frac{V(t)}{s + z_c} = \frac{V(t)}{i\omega_n + z_c}$$

at the instability frequency, and

$$V(t) = k_1 \frac{s + z_c}{s + (z_c + k_2)} p(t)$$

$$\hat{V} \sim k_1^* \hat{p},$$

together with

$$k_2 = p_c - z_c$$

$$k_2^* \sim \omega_n$$

(where  $-p_c$  is the pole of the final stabilizing controller) gives a final expression for  $\gamma_2$  of

$$\gamma_2 = \frac{\omega_n^3 \sqrt{\omega_n^2 + z_c^2}}{6\pi |k_1^*| \hat{p}^2}.$$

A final note on the choice of  $\hat{p}$ : this will depend on whether or not a limit cycle

is already present when control is activated. If the pressure perturbation is still growing when control is activated,  $\hat{p}$  is given by the (order of magnitude of the) pressure perturbation that one wants the controller to allow: previous pressure perturbations of smaller orders of magnitude than this will give rise to negligible rates of change of the adaptive parameters in (3.10). If the pressure perturbation has already established a limit cycle when control is activated, however, then the choice of  $\hat{p}$  is instead *imposed* by the limit cycle's amplitude.

These expressions provide a systematic way of choosing the adaptation rates, which were previously chosen by trial-and-error.

### 3.4 MODAL ADAPTIVE CONTROLLER

We now look at adaptive control of circumferential modes in annular combustors. This requires multiple pressure measurements and multiple fuel valves for feedback control, and therefore MIMO control (Morgans & Stow, 2007).

Instead of using MIMO control techniques, the adaptive controller that we now develop draws on the SISO adaptive controller already described, and relies on the combustor having an axisymmetric geometry. (For a large number of equally-spaced, identical burner valves, the combustor can still be considered axisymmetric with the burners in place – see Akamatsu & Dowling (2001) or Evesque & Polifke (2002).)

The combustor's axisymmetric geometry allows each unstable mode to be treated separately as a single-input single-output system, with open-loop modal transfer function  $P^n(s)$  given by (3.2). Since the modal adaptive controller works in terms of modal pressure  $p^n(t)$  and modal voltage  $V^n(t)$ , we must find expressions relating the individual actuator voltages  $V_b(t)$  and individual transducer pressures  $p_t(t)$  to their modal equivalents. For a combustor with  $B$  burners (with actuation at all burner locations), and if the pressure perturbation at some downstream location is measured using  $T$  pressure transducers equally-spaced around the combustor circumference, then the modal

voltage and pressure can be found using

$$p^n(t) = \frac{1}{T} \sum_{t=1}^T p_t(\theta, t) \Phi_1^n(\theta) \quad p_t(\theta, t) = \sum_{n=-N}^N p^n(t) \Phi_2^n(\theta) \quad (3.11)$$

$$V^n(t) = \sum_{b=1}^B V_b(\theta, t) \Phi_1^n(\theta) \quad V_b(\theta, t) = \frac{1}{B} \sum_{n=-N}^N V^n(t) \Phi_2^n(\theta), \quad (3.12)$$

where

$$\Phi_1^n(\theta) = \begin{cases} 1 & n = 0 \\ 2 \cos(n\theta) & n > 0 \\ 2 \sin(n\theta) & n < 0 \end{cases} \quad \Phi_2^n(\theta) = \begin{cases} 1 & n = 0 \\ \cos(n\theta) & n > 0 \\ \sin(n\theta) & n < 0. \end{cases} \quad (3.13)$$

The modal parameters  $p^n(t)$  and  $V^n(t)$  represent the discrete spatial Fourier transforms of the transducer pressures  $p_t(t)$  and actuator voltages  $V_b(t)$ . A standing wave representation is used because the controller parameters are updated in the time domain (Stow & Dowling, 2009).<sup>1</sup>

From (3.13), the  $+n$  and  $-n$  modes are 90 degrees out of phase with each other for a given  $n$ . Since  $P^n(s)$  is a SISO transfer function, the modal equivalent of the updating law (3.10) and feedback control law (3.9b) can now be used:

$$\dot{\mathbf{k}}^n(t) = \Gamma^n \text{sgn}(g_o^n) p^n(t) \mathbf{d}_\lambda^n(t) \quad (3.14a)$$

$$V^n(t) = -[\mathbf{k}^n]^T(t) \mathbf{d}^n(t) - [\dot{\mathbf{k}}^n]^T(t) \mathbf{d}_\lambda^n(t). \quad (3.14b)$$

Figure 3.5 shows the adaptive control procedure in pictorial form: at some time  $t$ , the adaptive controller is provided with a vector of pressure measurements  $\mathbf{p}(t)$ . From this, and using (3.11), a vector of modal pressures  $\mathbf{p}^n(t)$  is calculated. For each mode  $n$ , the modal pressure is used in the updating law for the adaptive parameters (3.14a), and the modal voltage resulting from this controller is calculated using (3.14b). Finally, the vector of modal voltages  $\mathbf{V}^n(t)$  is used to calculate the vector  $\mathbf{V}(t)$  using (3.12), which gives the voltage required at each burner.

<sup>1</sup>At a given moment in time, one cannot determine if a given mode shape is spinning in time or not. Therefore although one could use a spinning wave decomposition, we choose standing waves here, which make more sense conceptually.

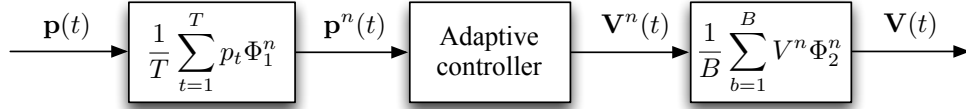


FIGURE 3.5: Modal adaptive control algorithm.

### 3.5 DESCRIPTION OF THE THERMOACOUSTIC NETWORK MODEL

LOTAN is a low order thermoacoustic network model developed by Dowling & Stow (2003) for the simulation of longitudinal and annular combustion systems. Low order modeling techniques are particularly attractive for annular combustors, owing to the high cost of computational fluid mechanics and of large-scale experiments for such geometries. The low order modeling approach is based on the fact that the main non-linearity is in the combustion response to flow perturbations (Dowling, 1997). LOTAN has been verified experimentally against both a sector rig (Stow & Dowling, 2001) and an atmospheric test rig (Stow & Dowling, 2004). The combustion system is modeled as a series of interconnected modules. Longitudinal ducts, annular ducts, combustion zones and area changes are amongst the module types that can be modeled.

The model decomposes the flow into a steady mean axial component and small perturbations. The perturbations throughout the combustor are related via wave propagation, in which acoustic waves, entropy waves and vorticity waves are all included. The flow conservation equations are used to track the evolution of these acoustic waves, vorticity waves and entropy waves. A thin annulus is assumed: therefore axial and azimuthal variations are considered, but radial variation of the flow parameters is ignored. The connecting modules are modeled as acoustically compact, meaning that their axial length is short in comparison to the acoustic wavelengths of interest. The acoustic boundary conditions at the inlet and outlet of the combustor are assumed to be known.

Combustion is assumed to take place at one axial location and to be acoustically compact. The flame dynamics are modeled using a flame transfer function relating the unsteady heat release  $Q$  to the fluctuation in equivalence ratio  $\phi$ . This is motivated by the fact that, for lean premixed prevaporized combustion, fluctuations in the inlet fuel-air ratio have been shown to be the dominant cause of unsteady combustion – see,

for example Richards & Janus (1998) or Lieuwen & Zinn (1998). Saturation bounds are applied to the unsteady heat release: this saturation leads to non-linear behaviour of the flame and the development of a limit cycle.

Calculations can be performed in both the frequency domain and the time domain (Stow & Dowling, 2009). Frequency domain calculations can be either linear or non-linear. For linear calculations, the values of complex frequency that satisfy both the inlet and outlet boundary conditions are found: this complex frequency gives the frequency of oscillation and growth rate of a given mode. Non-linear calculations can be performed to find the frequency and amplitude of the limit cycle. In this case, a non-linear flame transfer function (where the unsteady heat release rate saturates) is used whilst keeping the rest of the model linear. The resulting limit cycle's frequency and amplitude can then be calculated.

In time domain simulations, the transfer functions (excluding the flame) are converted to a Green's function and combined with the non-linear time domain model of the flame. Noise can be introduced into the system in the form of white noise superimposed on to the heat release at each burner, which acts to simulate turbulence and promotes the growth of unstable modes.

The two combustor geometries considered are simple representations of a Lean Premixed Prevaporized (LPP) aero-engine combustor, depicted in figure 3.6. Each combustor is made up of an annular plenum connected to an annular combustor by a number of equally-spaced premix ducts. Both combustor geometries are axisymmetric and therefore modal coupling is absent – see Akamatsu & Dowling (2001), where premix ducts leads to coupling of radial modes only, and Evesque & Polifke (2002), where circumferential modal coupling only occurs for non-identical premix ducts. Having uncoupled modes means that forcing the valve voltage in circumferential mode  $n$  gives rise to pressure fluctuations in circumferential mode  $n$  only.

For closed-loop control in LOTAN, actuation can be provided by fuel valves at each of the ducts, and sensing can be achieved using pressure transducers positioned downstream of the combustion zone.

### 3.6 ADAPTIVE CONTROL OF AN ANNULAR COMBUSTOR IN LOTAN

Using LOTAN, time domain simulations of an annular combustor with the modal adaptive controller (3.14) are now investigated. Control is first demonstrated for a combustor with a circumferential  $n = \pm 1$  unstable mode only. It is then shown that the adaptive controller maintains control following a large change in combustor operating conditions. Then by modifying the combustor geometry, an additional  $n = 0$  longitudinal instability is introduced. The adaptive controller stabilizes this modified system by simultaneously controlling the  $n = 0$  and  $n = \pm 1$  modes. Finally, a more practicable feedback control arrangement with fewer transducers and actuators is investigated. It is observed that the modal adaptive controller still provides stability with only three transducers and three actuators in place.

#### 3.6.1 COMBUSTOR GEOMETRIES

The combustor geometries used are the same as those used by Morgans & Stow (2007). Details of the geometry can be found in figure 3.6, whilst key parameters of the combustor are summarized in table 3.1. Twenty burners ( $B = 20$ ) and twenty pressure transducers ( $T = 20$ ) are positioned uniformly around the circumference of the annulus. A choked inlet and choked outlet are used for the upstream and downstream boundary conditions.

TABLE 3.1: Summary of unstable combustor's key parameters.

Air mass flow rate,	$\bar{a} = 100 \text{ kg/s}$
Combustion temperature,	$T_c = 2500 \text{ K}$
Number of fuel valves,	$B = 20$
Number of pressure transducers,	$T = 20$
Actuator transfer function, <sup>1</sup>	$L_b(s) = 0.1 e^{-2.0 \times 10^{-4}s}$
Flame transfer function,	$F_b(s) = 4.0 e^{-1.5 \times 10^{-3}s}$
Flame saturation properties:	$Q_{\text{sat}} = 0.4 \bar{Q}$

<sup>1</sup> The fuel valve can saturate at some points in the cycle if the fuel flow rate fluctuation exceeds the mean (at which point the overall fuel flow rate can reach zero).

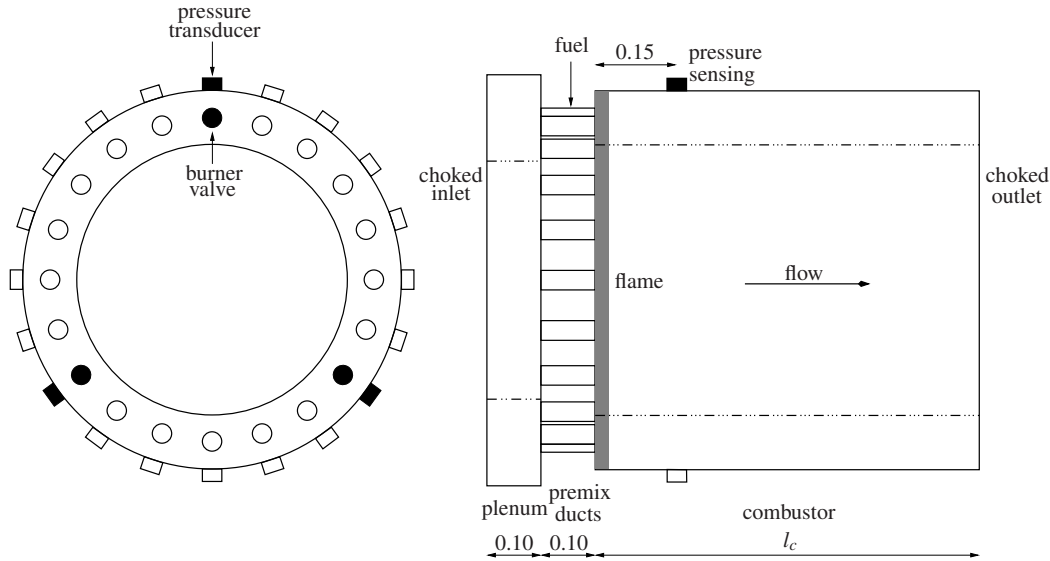


FIGURE 3.6: Annular combustor geometry. All dimensions in metres.  $l_c = 0.30$  m for the circumferential mode only case, and  $l_c = 0.71$  m for the multiple mode case. The plenum inner and outer radii are 0.22 m and 0.38 m respectively. The combustion chamber inner and outer radii are 0.25 m and 0.35 m respectively. The locations of the actuators and transducers used in § 3.7 are shown in black.

A simple gain/time delay flame transfer function of the form  $F_b(s) = k_f e^{-\tau_f s}$  is used with saturation bounds. The flame transfer function used is very similar in form to that used by Bellucci *et al.* (2005). The gain  $k_f$  represents the flame's linear gain, the time delay  $\tau_f$  represents the convection time from fuel input to combustion, and the saturation bound  $Q_{\text{sat}}$  represents the maximum fractional change in heat release that can occur. According to this model, the heat release responds linearly to flow perturbations for small oscillations. For unstable modes, though, the growing amplitude causes the heat release to saturate. This saturation results in non-linear behaviour of the flame and a limit cycle. Armitage *et al.* (2004) discuss flame models in more detail.

### 3.6.2 SINGLE CIRCUMFERENTIAL MODE

The Bode diagram of the open-loop  $n = \pm 1$  transfer function  $P^{\pm 1}(s)$  is shown in figure 3.7 for frequencies up to 2000 Hz (note the linear frequency scale). This transfer function is found using LOTAN: referring to equation (3.2),  $L_b(s)$  and  $F_b(s)$  are prescribed, whilst the modal transfer functions  $G^n(s)$  and  $H^n(s)$  are found in LOTAN by forcing

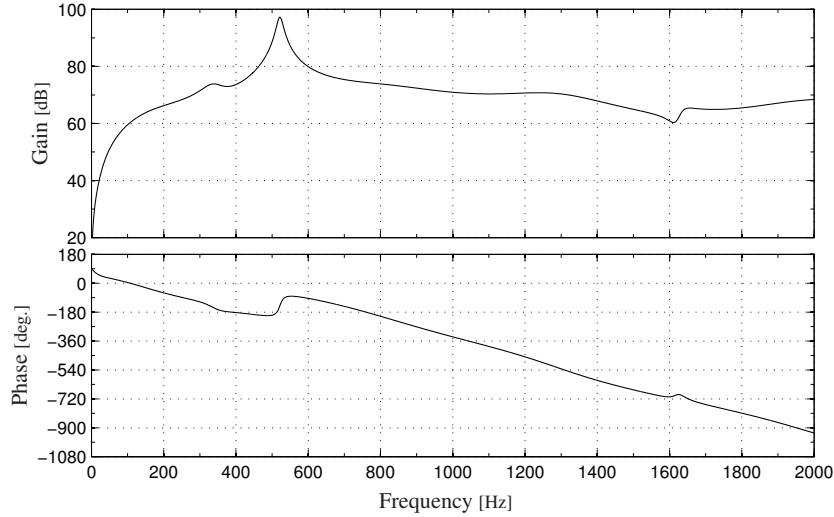


FIGURE 3.7: Open-loop Bode diagram of the modal transfer function  $P^{\pm 1}(s)$ .

their respective inputs over a discrete set of frequencies for the mode  $n$  of interest.

The poles of the system (3.2) correspond to the peaks of the Bode diagram: a phase increase of  $180^\circ$  across a peak indicates an unstable conjugate pair of poles, whilst a phase decrease of  $180^\circ$  indicates a stable conjugate pair (Dorf & Bishop, 2005). The frequency and growth rate of the unstable mode are 521 Hz and  $56.1 \text{ rad s}^{-1}$ . Figure 3.8 shows the limit cycle mode shape of the instability. The mode spins in time during the limit cycle – an effect caused by the modal coupling introduced by the non-linearity which is discussed in more detail by Schuermans (2003).<sup>1</sup> From figure 3.7 it can be seen that all of the zeros of the open-loop system are in the left half-plane. (Left half-plane zeros induce an increase in phase, whilst right half-plane zeros induce a reduction in phase.) Therefore assumption (i) concerning the position of the system’s zeros is satisfied.

The parameter values used for the  $n = \pm 1$  adaptive controller (in this and all other test cases) are  $z_c^{\pm 1} = 11000 \text{ rad s}^{-1}$ ,  $\gamma_1^{\pm 1} = 5.0 \times 10^{-14}$ ,  $\gamma_2^{\pm 1} = 1.0 \times 10^3$ , and  $\text{sgn}(g_0^{\pm 1}) = +1$ . The time domain simulation of the closed-loop system with adaptive controller is shown in figure 3.9. White noise is superimposed on to the mean heat release at each burner – the amplitude of the noise is 20% of the mean heat release at each burner. Control is activated at 0.5 seconds, by which time a limit cycle has

<sup>1</sup>This modal coupling is only present during the non-linear limit cycle.

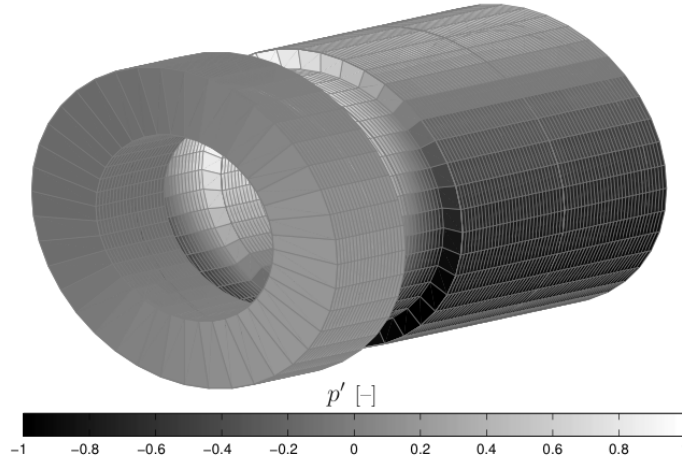


FIGURE 3.8: Pressure mode shape of the  $n = \pm 1$  spinning mode (arbitrary scale).

established itself. The adaptive controller finds stabilizing modal control parameters  $\mathbf{k}^{\pm 1}$  within approximately 0.2 seconds, and the pressure measurements are reduced to the background noise level. The adaptive controller arrives at identical modal controllers for the  $n = -1$  ( $\mathbf{k}^{-1}$ ) and  $n = +1$  ( $\mathbf{k}^{+1}$ ) modes: this corresponds to there being equal amounts of each mode present in the spinning limit cycle. Figure 3.10 shows a zoomed-in section of the time domain simulation for  $0.70 \leq t \leq 0.72$ . Only three of the twenty pressure measurements and actuated fuel mass flow rates are shown for clarity. From the phase difference observed between these three pressure measurements, it is clear that the mode shape is spinning in time when control is activated.

### 3.6.3 CHANGING OPERATING CONDITIONS

One of the distinct advantages of adaptive control is its ability to deal with large changes in the plant transfer function. This is now demonstrated by varying the combustor's flame transfer function  $F(s)$  with time once control of the nominal plant has been achieved. Specifically, the flame transfer function gain  $k_f$  (refer to table 3.1) is varied linearly from 4.0 to 5.2 over a 0.2 second period. Figure 3.11 shows the modal adaptive controller's response to this change in operating conditions. The adaptive parameters  $\mathbf{k}^{\pm 1}(t)$  re-adapt and find a new stabilizing controller, and closed-loop stability is maintained despite the change. Note that a *fixed* controller with the same parameters

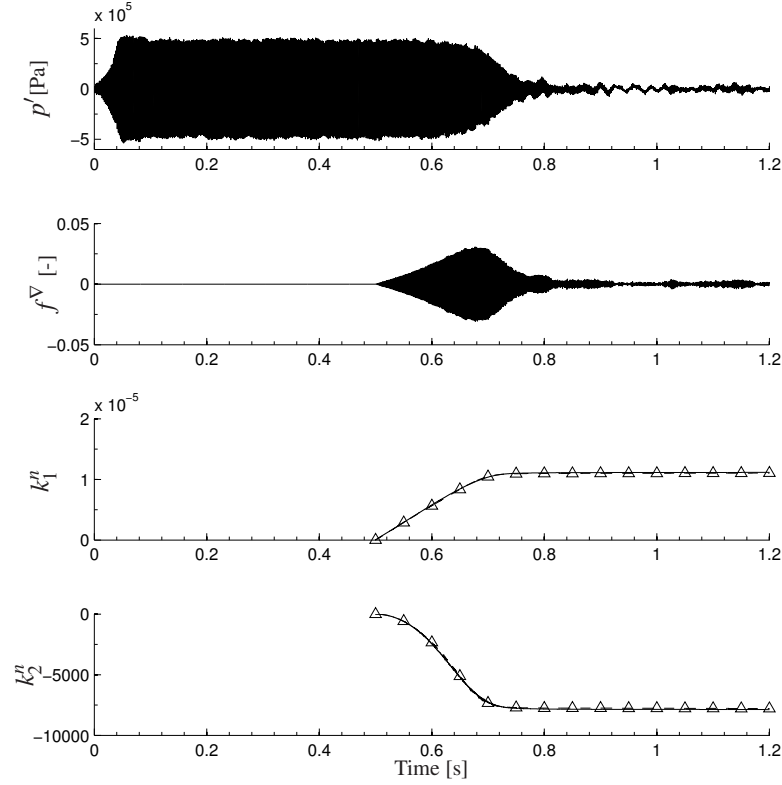


FIGURE 3.9: Adaptive control of the  $n = \pm 1$  unstable mode. The upper two plots show the measured pressure perturbation  $p'$  and the actuated fractional fuel mass flow rate  $f^V$ . The lower two plots show the adaptation of the modal control vector  $\mathbf{k}^n(t)$  for  $n = +1$  (—) and  $n = -1$  (-△-).

as the original adaptive controller would have lost control following this change.

#### 3.6.4 MULTIPLE UNSTABLE MODES

By increasing the combustion chamber's length from 0.30 m to 0.71 m (see figure 3.6), an  $n = 0$  longitudinal instability is introduced, with the frequency and growth rate of the  $n = \pm 1$  mode changing slightly. Table 3.2 shows the frequencies and growth rates of the two modes, and figure 3.12 shows the two modes' open-loop Bode diagrams. Again, and for both transfer functions, all of the zeros are in the left half-plane, and so assumption (i) concerning the position of the system's zeros is satisfied.

The parameter values used for the  $n = 0$  adaptive controller are  $z_c^0 = 11000 \text{ rad s}^{-1}$ ,  $\gamma_1^0 = 1.5 \times 10^{-15}$ ,  $\gamma_2^0 = 3.0 \times 10^2$  and  $\text{sgn}(g_0^0) = +1$ . The time domain simulation for

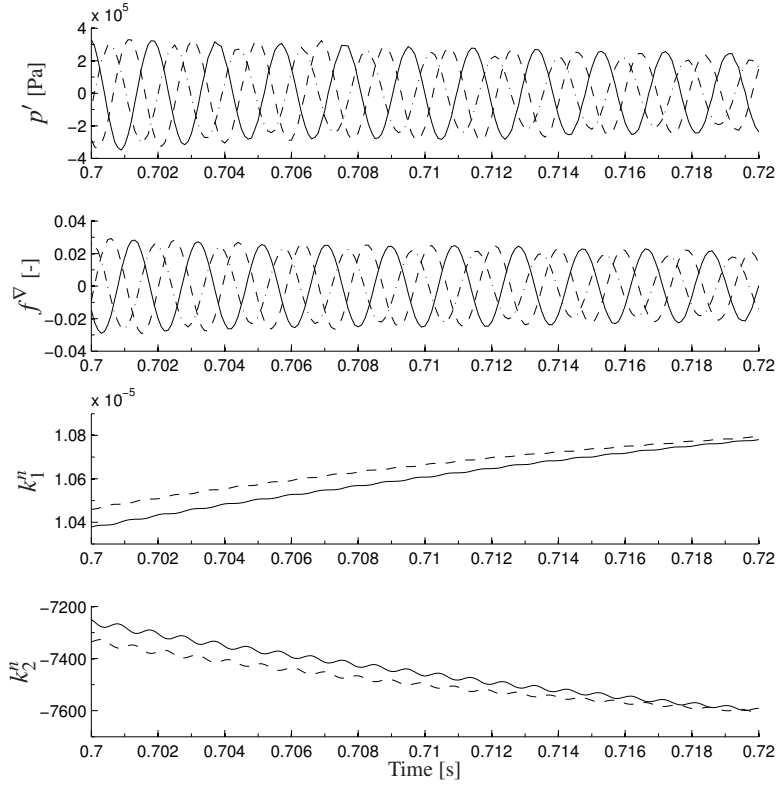


FIGURE 3.10: Adaptive control of the  $n = \pm 1$  unstable mode: zoomed-in section for  $0.70 \leq t \leq 0.72$ . The upper two plots show the measured pressure perturbation  $p'$  and the actuated fractional fuel mass flow rate  $f^V$ . Data for only three pressure transducers and three actuators at azimuthal angles of  $\theta = 0^\circ$  (—),  $\theta = 126^\circ$  (- - -) and  $\theta = 234^\circ$  (- · -) are shown for clarity. The lower two plots show the adaptation of the modal control vector  $\mathbf{k}^n(t)$  for  $n = +1$  (—) and  $n = -1$  (- - -).

the multiple unstable mode case is shown in figure 3.13. For no control whatever, the longitudinal mode with the higher growth rate grows first and dominates the response in the limit cycle. Thus only the longitudinal mode is present when control is activated at 0.5 seconds. The modal adaptive controller arrives at stabilizing adaptive parameters  $\mathbf{k}^0(t)$  after approximately 0.2 seconds. Following this the circumferential mode grows: the adaptive parameters  $\mathbf{k}^{\pm 1}(t)$  adapt accordingly and find a stabilizing controller. The combustion system is completely stabilized.

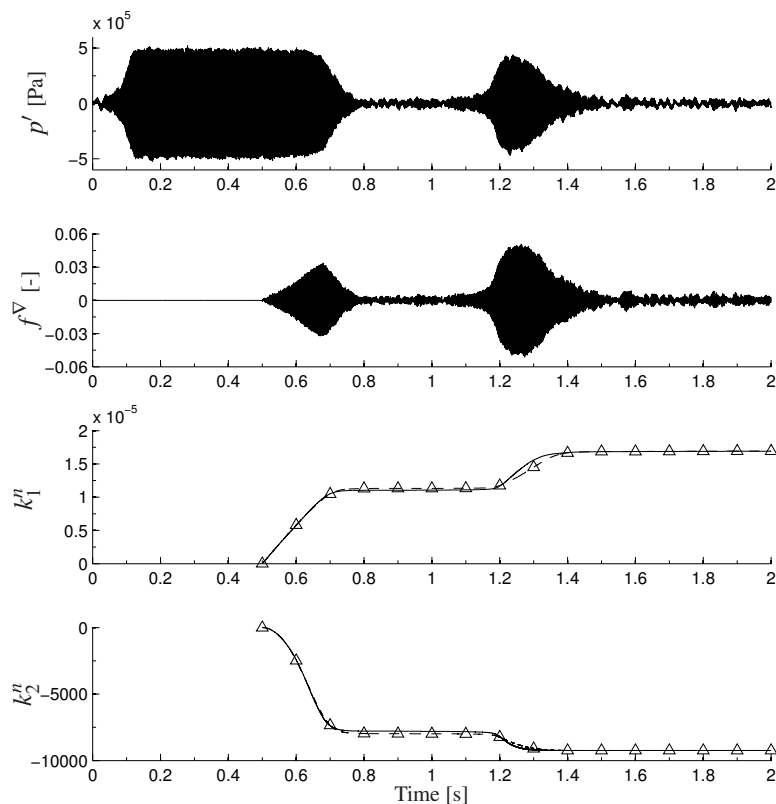


FIGURE 3.11: Time domain simulation of adaptive control of the  $n = \pm 1$  unstable mode. Flame transfer function gain  $k_f$  increased linearly from 4.0 at  $t = 1.0$  s to 5.2 at  $t = 1.2$  s. Legend same as figure 3.9.

### 3.7 CONTROL USING FEWER TRANSDUCERS AND ACTUATORS

To ensure that the axisymmetry assumption still holds with the adaptive feedback controller in place, twenty transducers and twenty actuators were used. From practical considerations, though, this is a large number. Therefore it is interesting to investigate

TABLE 3.2: Frequencies and growth rates of the two unstable modes.

$n$	Frequency [Hz]	Growth rate [ $\text{rad s}^{-1}$ ]
0	616	16.0
$\pm 1$	511	11.3

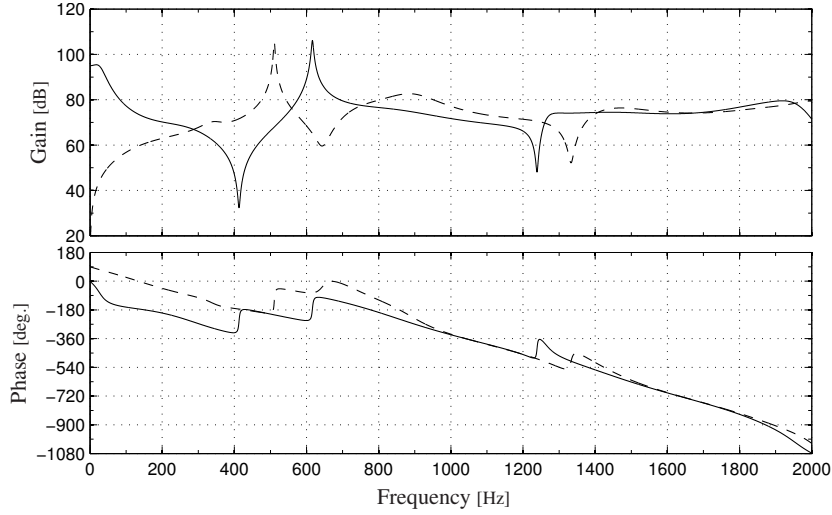


FIGURE 3.12: Open-loop Bode diagram of the two modal transfer functions:  $P^0(s)$  (—) and  $P^{\pm 1}(s)$  (---).

the behaviour of the closed-loop system with fewer transducers and actuators in place.<sup>1</sup>

To construct the modal pressure vector  $\mathbf{p}^n = [p^{-N} \dots p^{+N}]^T$  from the vector of measured pressures  $\mathbf{p} = [p_1 \dots p_T]^T$ , the minimum number of transducers needed is given by the maximum circumferential mode of interest  $N$ . Since one must ensure that the transducers do not find themselves all simultaneously at pressure nodes of the combustor, the minimum number of transducers required  $T_{\min}$  is given by  $T_{\min} = 2N + 1$ . A similar argument can be applied to the number of actuators to give  $A_{\min} = 2N + 1$ . (It is worth noting that reducing the number of measurement points will not affect the combustor's axisymmetry, whilst reducing the number of actuation points will.)

Since it was assumed previously that actuation occurred at all burner locations (i.e.  $A = B$ ), the control voltage vector is now of reduced dimension  $\mathbf{V} = [V_1 \dots V_A]^T$ . In this simpler case, (3.11) still holds: the modal pressure amplitudes  $\mathbf{p}^n$  are real quantities and can still be deduced from a reduced number of pressure measurements. For the control voltage, though, the modal voltage  $\mathbf{V}^n$  is not being deduced from the actuator voltages  $\mathbf{V}$ . Rather, for a given  $\mathbf{V}^n$ , which is provided by the modal adaptive controller (figure 3.5), we want to find the combination of actuator voltages  $\mathbf{V}$  which

<sup>1</sup>Although the number of actuators is reduced, the combustor still has twenty burners: the reduction means that closed-loop actuation is only taking place at some rather than all burner locations.

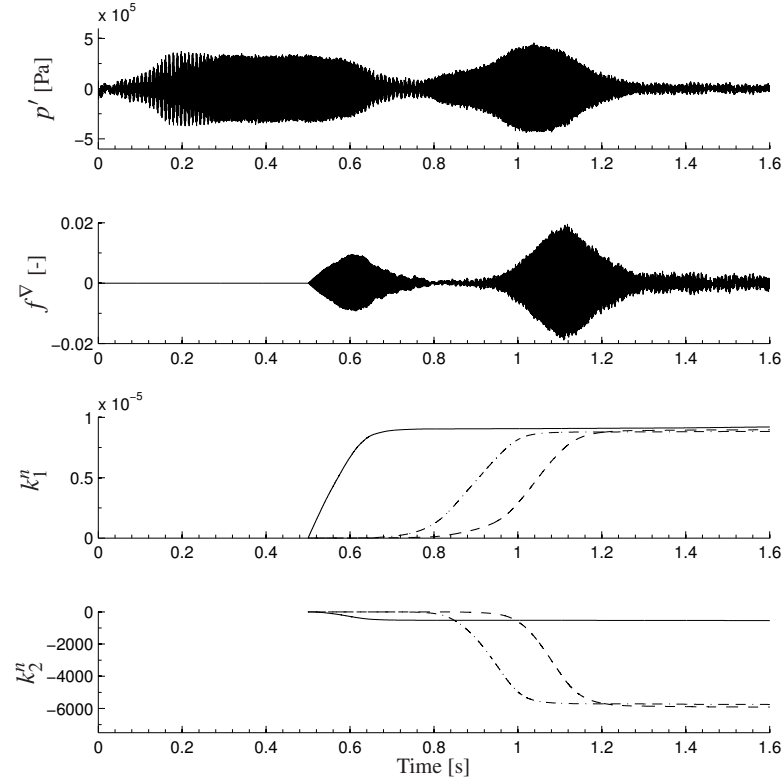


FIGURE 3.13: Time domain simulation of adaptive control of the  $n = 0$  and  $n = \pm 1$  unstable modes. The upper two plots show the measured pressure perturbation  $p'$  and the actuated fractional fuel mass flow rate  $f^V$ . The lower two plots show the adaptation of the modal control vector  $\mathbf{k}^n(t)$  for  $n = 0$  (—),  $n = +1$  (---) and  $n = -1$  (-·-·).

best approximates this modal voltage. Therefore instead of the discrete Fourier transform pair in (3.12), we simply write

$$V_a(\boldsymbol{\theta}, t) = \frac{1}{A} \sum_{n=-N}^N V^n(t) \Phi_2^n(\boldsymbol{\theta}).$$

For the combustor considered  $N = 1$ , so  $T_{\min} = B_{\min} = 3$  and therefore we use three actuators and three transducers. Figure 3.6 shows the location of the three actuators and three transducers, which are at azimuthal angles of  $0^\circ$ ,  $126^\circ$  and  $234^\circ$ .

Figure 3.14 shows time domain results for this simpler control arrangement, applied to the combustion geometry with the  $n = \pm 1$  unstable mode only (as in § 3.6.2). All other control parameters are the same as those used in § 3.6.2. Comparison with

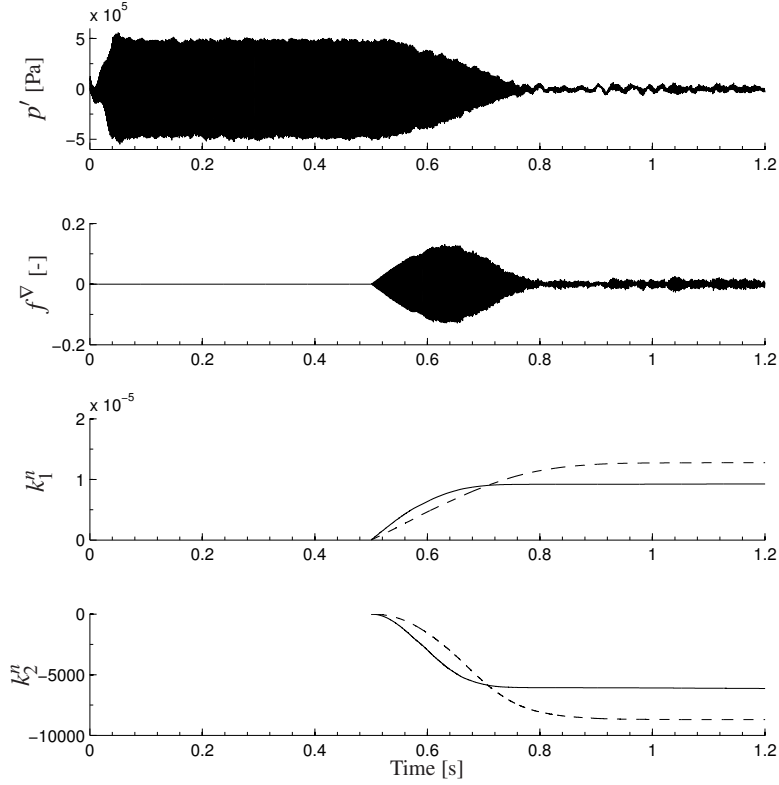


FIGURE 3.14: Time domain simulation of adaptive control using fewer transducers and actuators. The upper two plots show the measured pressure perturbation  $p'$  and the actuated fractional fuel mass flow rate  $f^V$ . The lower two plots show the adaptation of the modal control vector  $\mathbf{k}^n(t)$  for  $n = +1$  (—) and  $n = -1$  (---).

figure 3.9 reveals the behaviour of this simpler arrangement and the fully-instrumented arrangement to be very similar. The most obvious difference is the increased magnitude of the fuel mass flow rate actuation required for control, which in this simpler case is 15 % of the mean, compared with 3 % of the mean in figure 3.9. This is explained by the greater control authority required at each actuation point when the total number of actuators is reduced. One also observes that the time required for the adaptive parameters  $\mathbf{k}^n$  to settle to stabilizing values is greater, in particular for the  $n = -1$  circumferential mode. Finally, the discrepancy between the final control vectors  $\mathbf{k}^{-1}$  and  $\mathbf{k}^{+1}$  is greater than that seen in figure 3.9. Nevertheless, both modal controllers arrive at stabilizing control parameters and the combustion system is stabilized.

### 3.8 CONCLUDING REMARKS

In this chapter, two properties of unstable aero-engine combustion systems that complicate their stabilization have been addressed: their annular geometry and therefore their propensity for circumferential modes; and their potential for large changes in operating conditions. For these reasons the adaptive controller presented is well-suited to real engine environments.

We finish by remarking that the adaptive feedback controller considered operates outside of the restrictions placed upon it in its theoretical development. The Lyapunov-based stability analysis of § 3.3 is valid only for linear plants, and yet control is activated from within a non-linear limit cycle. The SISO analysis used in § 3.2.1 also relies on an axisymmetry assumption, and yet the adaptive controller of § 3.7 clearly neglects this assumption. (Although the controller of § 3.6 respects it.)



## CHAPTER 4

### ADAPTIVE CONTROL FOR UNKNOWN CONTROL DIRECTION

One of the fundamental (and troublesome) requirements of classical, Lyapunov-based adaptive control is that the sign of the high-frequency gain of the system must be known (Narendra & Annaswamy, 1989). Since time delays are always present in combustion systems, they are of infinite dimension. Therefore the sign of the high-frequency gain is never known a priori and must somehow be determined. For this reason a controller that does not require this information presents advantages for the adaptive control of combustion oscillations.

In this chapter, an adaptive feedback controller is applied to a simple unstable combustion system: the Rijke tube. The controller does not require knowledge of the sign of the high-frequency gain of the system, and this represents the first experimental demonstration of such a controller. Control is maintained following a large change in operating conditions, brought about by increasing the length of the Rijke tube after control of the nominal system has been achieved.

#### 4.1 IMPORTANCE OF THE HIGH-FREQUENCY GAIN

At the heart of Lyapunov-based adaptive control are three assumptions. If the open-loop system has transfer function  $P(s)$ , and if we write  $P(s)$  as the ratio of two coprime, monic polynomials

$$P(s) = g_o \frac{N_P(s)}{D_P(s)},$$

then the three conditions placed on  $P(s)$  are (Narendra & Annaswamy, 1989)

- (i) The sign of the high-frequency gain  $g_o$  is known.

(ii) The relative degree  $n^*$  of  $P(s)$  is known.<sup>1</sup> (I)

(iii) The zeros of  $P(s)$  are all stable (i.e. the system is minimum phase).

It is the first condition that we concern ourselves with here. For many systems, the sign of the high-frequency gain (whose physical significance is given in the following) is obvious from the physics of the problem, and so providing it poses no problem. For combustion systems, however, which are infinite-dimensional, the sign of the high-frequency gain of the system is unknown and must be determined. (The phase of such a system evolves indefinitely with frequency, and so the sign of its high-frequency gain is not well-defined.)

#### 4.1.1 PHYSICAL SIGNIFICANCE OF THE HIGH-FREQUENCY GAIN

To demonstrate the physical significance of the high-frequency gain, we now look at a simple first-order unstable system whose transfer function is

$$P(s) = \frac{y(s)}{u(s)} = \frac{g_0}{s - a}, \quad (4.1)$$

where  $u$  is the system input,  $y$  is the system output,  $s = i\omega$  is the Laplace variable,  $g_0$  is the high-frequency gain of the system and  $a$  (which is positive for an unstable system) corresponds to the location of the system's (only) pole.

In the time domain, this corresponds to the first-order differential equation

$$\dot{y}(t) = ay(t) + g_0u(t).$$

Looking at  $\dot{y}(t)$  for small time using the initial value theorem, and for a unit step input  $u(s) = 1/s$ :

$$\begin{aligned} \lim_{t \rightarrow 0^+} \dot{y}(t) &= \lim_{s \rightarrow \infty} s^2 y(s) \\ &= \lim_{s \rightarrow \infty} s^2 \frac{1}{s} \frac{g_0}{s - a} \\ &= g_0. \end{aligned}$$

---

<sup>1</sup>The relative degree is defined as  $n^* = \deg[D_P(s)] - \deg[N_P(s)]$ .

Therefore knowing the *sign* of the high-frequency gain corresponds to knowing, in the time domain, the sign of the system's 'instantaneous gain': that is, knowing whether the system's response to a positive unit step input is positive or negative for  $t$  sufficiently small. More generally, for an  $n^{\text{th}}$  order system with a relative degree of  $n^*$ , the same analysis can be applied to the  $(n^*)^{\text{th}}$  derivative of the output,  $y^{(n^*)}$ .

#### 4.1.2 IMPORTANCE FOR FEEDBACK CONTROL

We can see the significance of  $g_o$  for feedback control by again considering the simple first-order unstable system (4.1), this time remaining in the frequency domain throughout. If we introduce a feedback gain as shown in figure 4.1, the overall closed-loop transfer function  $P_{\text{cl}}(s)$  is (negative feedback convention)

$$\begin{aligned} P_{\text{cl}}(s) &= \frac{P(s)}{1 + kP(s)} \\ &= \frac{g_o}{s + (kg_o - a)}. \end{aligned}$$

Since the controller gain  $k$  acts to stabilize the system by moving the closed-loop system's pole into the left half plane (i.e. by making the term  $(kg_o - a)$  positive), we see that the gain  $k$  must be both of the correct sign (so that the product  $kg_o$  is positive) and sufficiently large  $kg_o > a$ . Therefore the sign of  $g_o$  dictates the sign of  $k$  required for closed-loop stability. Again, this result still holds true for an  $n^{\text{th}}$  order system, as long as it has a *relative* degree  $n^*$  of one. (It can be shown, using root locus arguments, that any minimum phase system with a relative degree of one can be stabilized using a feedback gain alone.)

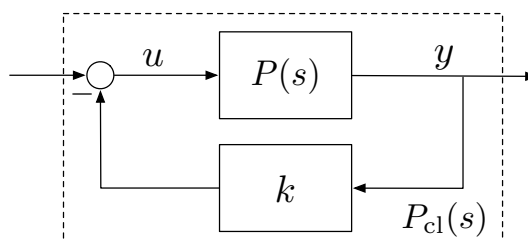


FIGURE 4.1: Feedback arrangement using a feedback gain  $k$ .

### 4.1.3 IMPORTANCE FOR LYAPUNOV-BASED ADAPTIVE CONTROL

We now look at how these arguments apply to Lyapunov-based adaptive control. A system of relative degree one that satisfies the three conditions (I) can be stabilized using just a feedback gain  $k$  (Dorf & Bishop, 2005). We have seen that this feedback gain needs to be (i) of sufficient magnitude and (ii) of the right sign. For a Lyapunov-based adaptive controller, the second condition must be provided (see the updating law in (3.9a), for example). Then the adaptive controller is guaranteed to meet the first condition and provide closed-loop stability.

Although we have already seen in chapter 3 how  $\text{sgn}(g_o)$  is used in the updating law for Lyapunov-based adaptive control (see equation (3.8), for example), we look specifically at the feedback gain only case here for ease of exposition. In this case, the sign of the high-frequency gain of the system is used to form an adaptive controller with updating rule and control law

$$\dot{k}(t) = \text{sgn}(g_o)y^2(t) \quad (4.2)$$

$$u(t) = -k(t)y(t), \quad (4.3)$$

which guarantees stability of the closed-loop system. It is clear how the  $\text{sgn}(g_o)$  is used in (4.2) to decide in which direction to update the control gain  $k$ .

## 4.2 ADAPTIVE CONTROL USING A NUSSBAUM GAIN

Morse (1983) suggested that knowledge of the sign of the high-frequency gain was intrinsic: in particular, that a linear plant *cannot* be stabilized without knowledge of the sign of  $g_o$ . Nussbaum (1983) proved this conjecture for first order *rational* controllers. More importantly, however, by using a non-rational term he constructed a globally adaptively stabilizing controller for a first order system which did not rely on knowledge of the sign of  $g_o$ . The work of Willems & Byrnes (1984) extends Nussbaum's result to any minimum-phase system with a relative degree of one.

The controllers used by Nussbaum (1983) and by Willems & Byrnes (1984) both incorporate a *Nussbaum gain*  $N(k)$ . Willems & Byrnes (1984) show that for the control

of a minimum phase system with a relative degree of one, any function  $N(k)$  which satisfies the conditions

$$\begin{aligned} \sup_{k>0} \frac{1}{k} \int_0^k N(\sigma) d\sigma &= \infty \\ \inf_{k>0} \frac{1}{k} \int_0^k N(\sigma) d\sigma &= -\infty \end{aligned} \quad (4.4)$$

is a Nussbaum gain and guarantees closed-loop stability when the sign of the high-frequency gain is unknown. Such a Nussbaum gain can be used with the updating rule and control law

$$\begin{aligned} \dot{k}(t) &= y^2(t) \\ u(t) &= -N(k)y(t) \end{aligned}$$

to adaptively stabilize the system. These are very similar to the updating rule (4.2) and control law (4.3) for the Lyapunov controller. The key difference is that the Nussbaum gain – and the conditions placed upon it – remove the need for knowledge of  $\text{sgn}(g_o)$ .

Functions satisfying (4.4) are a type of switching function. The review paper of Ilchmann (1999) gives some examples of such functions, including:

$$\begin{aligned} N_1(k) &= k^2 \cos k \\ N_2(k) &= \begin{cases} k & \text{if } n^2 \leq |k| < (n+1)^2, \quad n \text{ even} \\ -k & \text{if } n^2 \leq |k| < (n+1)^2, \quad n \text{ odd.} \end{cases} \end{aligned}$$

It is now clear how the Nussbaum gain achieves control without knowledge of the sign of the high-frequency gain. The conditions imposed upon a Nussbaum gain (4.4) mean that it sweeps across both positive and negative gains, whilst also increasing in magnitude with increasing  $k$ . Provided that this occurs, the system can be stabilized without knowledge of  $\text{sgn}(g_o)$ : in contrast to the Lyapunov-based adaptive controller, a Nussbaum gain automatically meets *both* requirements for closed-loop stability.

In closed-loop control, unnecessarily high feedback gains are to be avoided, not least because they can place high demands on the actuator, and because they can lead

to excitation of other modes of the system. Using a Nussbaum gain which is a smooth function helps to alleviate any high gain behaviour of the Nussbaum gain. Furthermore, one can help to ensure that the final stabilizing Nussbaum gain,  $N^*$ , is in the vicinity of the minimum required, and not significantly larger, by observing that the Nussbaum gain only need switch sign once, if at all. This is explained more fully in appendix D, where choosing the adaptation rate  $\mu$  (introduced later in equation (4.7)) is discussed.

### 4.3 NUSSBAUM GAIN ADAPTIVE CONTROL APPLIED TO A RIJKE TUBE

We now look at applying a Nussbaum-gain adaptive controller to a simple laboratory-scale experiment: the Rijke tube. We will see that the controller is able to stabilize the system without knowledge of  $\text{sgn}(g_0)$ , and that the controller is robust to changing operating conditions. To the author's knowledge, it represents the first experimental results for a Nussbaum-type adaptive controller.

#### 4.3.1 EXPERIMENTAL ARRANGEMENT

The Rijke tube provides a simple means of generating combustion oscillations on a laboratory scale. It consists of a vertical cylindrical tube open at both ends, with a heat source inside the tube some distance from the lower end. Large-amplitude acoustic oscillations are excited when the heat source is in the lower half of the tube (Howe, 1998).

Active control has previously been demonstrated on a Rijke tube (Dines, 1983; Lang *et al.*, 1987; Heckl, 1988). It has been observed that the system can be stabilized using a feedback gain alone (i.e. phase compensation is not required), and so the Rijke tube provides a suitable test-bed for a Nussbaum-gain adaptive controller.

The Rijke tube used consists of a cylindrical quartz tube of length 750 mm and diameter 44 mm inclined vertically as shown in figure 4.2(a). A propane-fuelled Bunsen burner provides a laminar flame which is stabilized on a grid 210 mm above the bottom of the tube. In the absence of control, the Rijke tube exhibits oscillations at a frequency of 244 Hz.

Measurement of the pressure perturbation (denoted  $p$ ) is provided by a microphone

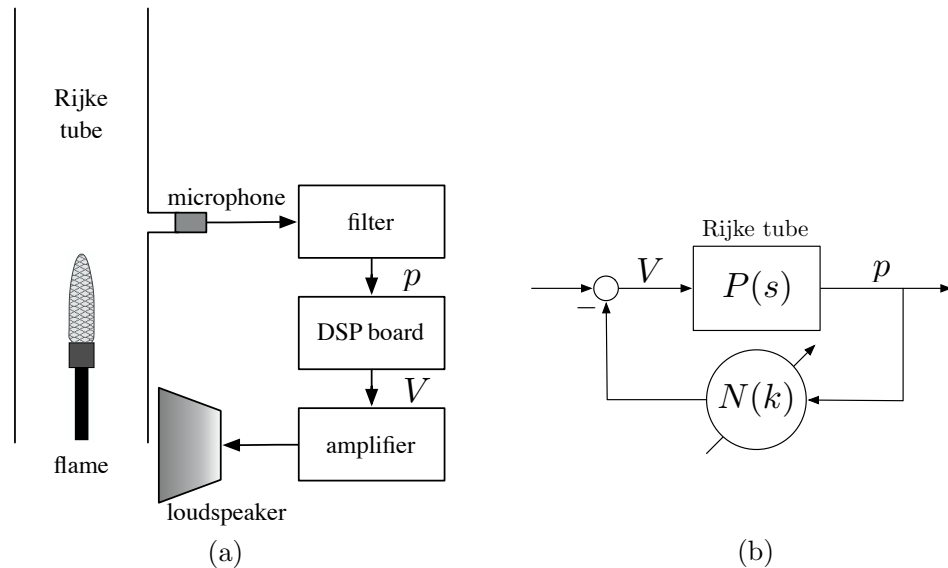


FIGURE 4.2: Experimental set-up of the Rijke tube: (a) schematic; and (b) corresponding block diagram.

fitted to a tube tapping situated 410 mm from the bottom of the tube. The semi-infinite line technique is used to obtain thermal insulation without distortion from acoustic reflections. Actuation is achieved using a 50 W low-frequency loudspeaker (with the control voltage to the loudspeaker before amplification denoted  $V$  – see figure 4.2(a)) situated close to the lower end of the tube. The loudspeaker exhibits a flat frequency response over the frequency range of interest (50–2000 Hz). Outside of this range, its dynamics becomes more complicated. To eliminate this dynamics, a bandpass filter is applied to the microphone signal with a pass-band from 50 Hz to 2000 Hz.

#### 4.3.2 NUSSBAUM ADAPTIVE CONTROLLER

The Rijke tube can now be treated like the general plant described in § 4.2, where the microphone voltage  $V$  corresponds to the system input  $u$ , and the pressure perturbation  $p$  corresponds to the system output  $y$ . This is seen more clearly in figure 4.2(b), where an arrow crossing a circle indicates an adaptive parameter. The updating rule and

control law for the adaptive controller are

$$\dot{k}(t) = \gamma p^2(t) \quad (4.5)$$

$$V(t) = -N(k)p(t), \quad (4.6)$$

and the Nussbaum gain used is

$$N(k) = k \cos(\mu |k|^{\frac{1}{4}}), \quad (4.7)$$

with  $\gamma = 100$  and  $\mu = 0.53$ . Here  $\gamma$  and  $\mu$  are the adaptation rates of the controller, explained in more detail in appendix D.

The theoretical development of the Nussbaum gain in § 4.2 ignores the influence of noise in the system. Since noise will always be present in the pressure measurement  $p$  (even when the system has been stabilized), we see from (4.5) that  $k(t)$  will never be stationary. This problem can be solved by introducing a *dead-zone* into the updating rule (Ioannou & Sun, 1996). With this modification,  $k(t)$  is only updated if the pressure  $p$  exceeds some pre-defined limit (which is chosen based on the magnitude of the noise in the system). The updating rule for  $k(t)$  then becomes

$$\dot{k}(t) = \begin{cases} \gamma p^2(t) & |p(t)| \geq P_{\text{deadzone}} \\ 0 & |p(t)| < P_{\text{deadzone}}. \end{cases} \quad (4.8)$$

We choose  $P_{\text{deadzone}} = 0.04$  in this particular case, which is about 5% of the limit-cycle amplitude.

This adaptive control algorithm is implemented on a TI C6713DSK DSP board with ADC and DAC evaluation modules (an ADS8361EVM and a DAC7731EVM). The pressure measurement  $p$  and control voltage  $V$  are recorded using a PC-based data acquisition system. The sampling frequency for both the DSP board and the data acquisition system is 5000 Hz.

#### 4.4 EXPERIMENTAL RESULTS

Two sets of experimental results are now presented. First, for fixed operating conditions, the Nussbaum controller achieves control even when it is first updated in the wrong direction. Second, we study the robustness of the controller by changing the length of the Rijke tube after control of the nominal system has been achieved. The controller maintains control following this change.

##### 4.4.1 FIXED OPERATING CONDITIONS

Figure 4.3(a) shows adaptive control results when the Nussbaum gain is initially updated in the right direction. The pressure perturbation has already established a limit cycle when control is activated at  $t = 0.2$  s. Since the Nussbaum gain is initially updated in the right direction, the cosine term in the Nussbaum gain (4.7) does not switch sign. Hence in this case the controller behaves in a similar way to a Lyapunov-based adaptive controller, and the growth of the Nussbaum gain  $N(k)$  is very similar to that of the adaptive parameter  $k$ .<sup>1</sup> Within approximately 0.5 s of control being activated, the controller finds a stabilizing gain  $N^*$ , and the system is stabilized.

Figure 4.3(b) shows adaptive control results when the Nussbaum gain is initially updated in the wrong direction. The impact of this is clear: when control is first activated at  $t = 0.2$  s, the Nussbaum gain  $N(k)$  causes the Rijke tube's limit cycle to actually increase in amplitude. Soon after, however, the Nussbaum gain changes sign and finds a stabilizing gain  $N^*$  which is both of sufficient magnitude and of the right sign. The system is stabilized within approximately 0.4 s of control being activated. The value of the Nussbaum gain used in this case is 2.10, compared with 1.78 in figure 4.3(a).

##### 4.4.2 VARYING OPERATING CONDITIONS

We now look at the robustness of the adaptive controller by increasing the length of the Rijke tube after control of the nominal plant has been achieved. The length of the tube is increased from 770 mm to 870 mm using a variable length attachment, which causes

<sup>1</sup> $k$  starts from zero here (i.e.  $k(0) = 0$ ), which is true for all three experiments.

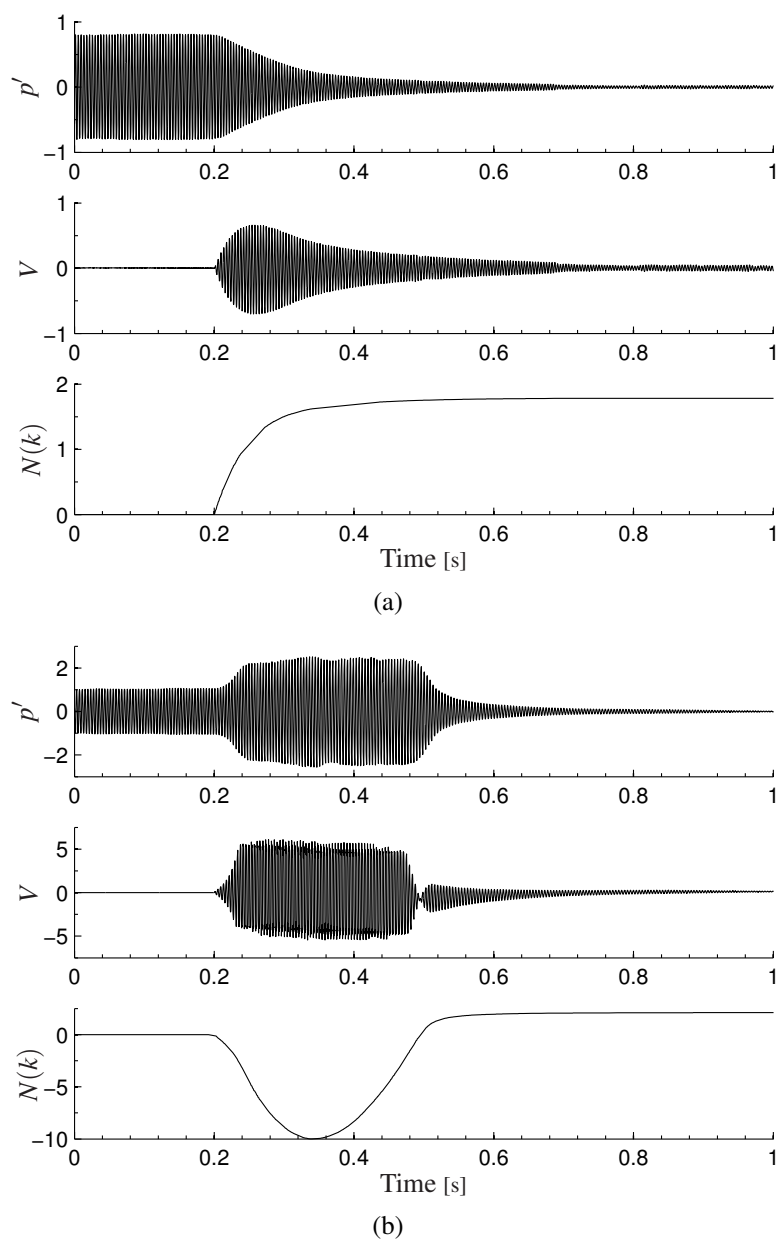


FIGURE 4.3: Experimental results for fixed operating conditions: with (a)  $N(k)$  initially updated in the right direction; and (b)  $N(k)$  initially updated in the wrong direction. In both cases the measured pressure perturbation, control voltage and Nussbaum gain are shown.

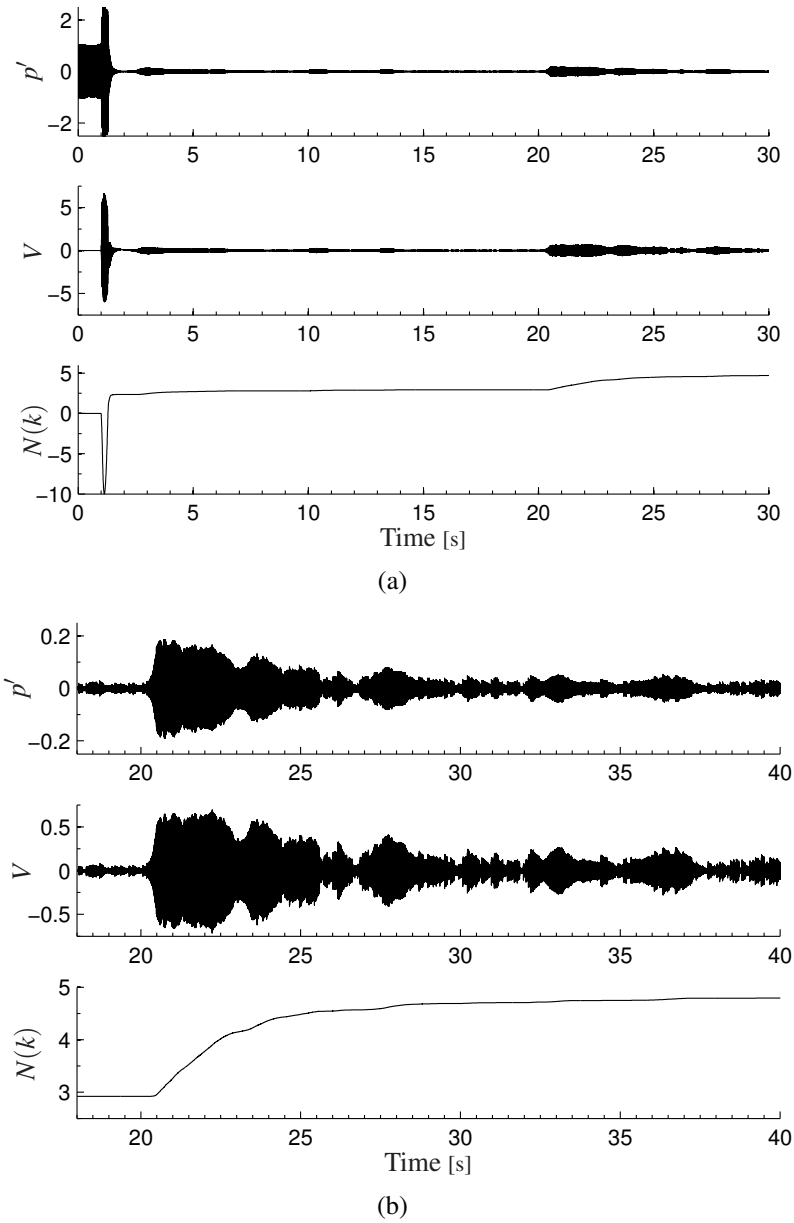


FIGURE 4.4: Experimental results for varying tube length ( $N(k)$  initially updated in the wrong direction): (a) tube length increased at approximately 18 s; and (b) zoomed-in plot of the controller's re-adaptation following the change in length. In both cases the measured pressure perturbation, control voltage and Nussbaum gain are shown.

a shift in frequency of the unstable mode from 238 Hz to 214 Hz.<sup>1</sup> Results are shown in figure 4.4(a), where control is activated at  $t = 0.2$  s, again from within the limit cycle. The Nussbaum controller finds a stabilizing gain within approximately 0.4 s.

After approximately 18 s, the length of the Rijke tube is suddenly increased. The Nussbaum gain is no longer stabilizing for this new length, but the controller re-adapts and finds a new stabilizing gain. This is seen more clearly in figure 4.4(b) which shows a zoomed-in section of figure 4.4(a). Here the time axis starts just before the length of the Rijke tube is increased.

#### 4.5 CONCLUDING REMARKS

This chapter has focused on adaptive control of combustion oscillations in a simple experiment, and considers the adaptive control problem when the sign of the high-frequency gain (or ‘control direction’) is unknown.

The proof of stability of the Nussbaum gain is for systems with a relative degree of one. In the experiments, however, it adaptively stabilizes a *gain-stabilizable* system: these two conditions are not equivalent (indeed, based on the observations made in chapter 2, we expect the actuated Rijke tube to have a relative degree not exceeding two).<sup>2</sup> Furthermore, the proof is valid only for linear systems, while in the experiments, the controller establishes control from within the Rijke tube’s pressure limit cycle. It is clear, then, that the Nussbaum controller is capable of adaptive stabilization outside of the restrictions placed upon it in its theoretical development.

---

<sup>1</sup>This first tube length is slightly longer than that for the fixed operating conditions case in § 4.4.1, owing to the geometry of the variable length attachment.

<sup>2</sup>For minimum-phase systems, the class of  $n^* = 1$  systems is a subset of the class of gain-stabilizable systems, and so a  $n^* = 1$  condition is more restrictive than a gain-stabilizable condition.

## CHAPTER 5

### DYNAMICS OF CAVITY OSCILLATIONS

In this chapter the compressible flow past a two-dimensional rectangular cavity is considered. We focus on the dynamics that are important for feedback control purposes. An historical perspective to the problem is first given. Direct numerical simulations are then used to find the open-loop transfer function of the cavity flow between a body force near the cavity's leading edge and a pressure measurement at some point inside the cavity. The results are compared to those given by a simple linear model of the cavity flow, which is intended to be useful for feedback control design. The choice of parameters for this linear model is based on flow data from the direct numerical simulations. We finish by deriving some general properties of the cavity flow that are useful for feedback control, and that will be used for adaptive control in chapter 6.

#### 5.1 INTRODUCTION AND HISTORICAL PERSPECTIVE

Cavity flows are another example of a self-sustained oscillation, and can occur in a wide variety of guises, including the flow past a sunroof in an automobile, and the flow past aircraft landing gear wells and weapons bays.

The basic configuration of a cavity flow is shown in figure 5.1. We consider the compressible flow past shallow cavities. The mechanism leading to self-sustained oscillations in such cavities is as follows: the shear layer formed at the cavity's upstream corner amplifies disturbances as they convect downstream, which are then scattered into pressure fluctuations at the cavity's downstream corner. These pressure fluctuations propagate back upstream, and excite further disturbances in the shear layer via a

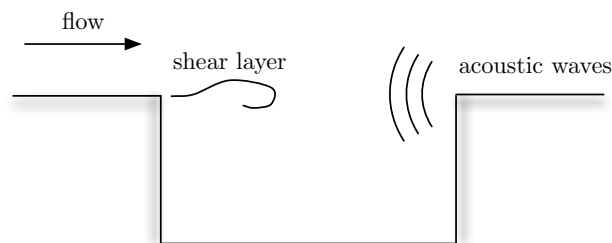


FIGURE 5.1: Basic configuration of a cavity flow.

receptivity process, creating a feedback loop. For suitable phase change of the disturbance, resonance occurs.

Cavity flows were studied as early as the 1950s by Roshko (1955) and Krishnamurthy (1956), but the flow-acoustic resonance phenomenon was first described by Rossiter (1964). (A similar model had previously been proposed by Powell (1953) for edge tones.) Rossiter provided a semi-empirical formula for the prediction of the resonant frequencies, which are often referred to as the *Rossiter tones*. More details about the physics of cavity flows can be found in the review articles of Rockwell & Naudascher (1978), Blake & Powell (1986) and Colonius (2001).

Strategies to eliminate cavity oscillations can be split into two broad categories: passive control and active control. We define these two broad classes of control as we did in chapter 2 (figure 2.2). Passive control studies have typically involved geometry modifications such as spoilers, fences and ramps (Heller & Bliss, 1975). Active, open-loop control studies date back to Sarohia & Massier (1977), who used steady mass injection at the base of the cavity, but later studies have typically involved forcing the shear layer near the cavity's upstream corner (Sarno & Franke, 1994; Stanek *et al.*, 2000).

A renewed interest in cavity flows in recent years is in part due to the possibility of using feedback (or 'dynamic') control to suppress oscillations. The idea of using feedback to suppress cavity oscillations is not new (Gharib, 1987), but many of the earlier studies used simple (trial-and-error) phase-locked controllers (Shaw & Northcraft, 1999; Williams *et al.*, 2000), which do not use models of the cavity flow dynamics. More recently, model-based feedback control has been promoted (Rowley

*et al.*, 2006): dynamical models of the cavity flow have typically been found using either system identification methods (Kook *et al.*, 2002; Kegerise *et al.*, 2007a,b) or the Proper Orthogonal Decomposition (Samimy *et al.*, 2007), and standard techniques such as Linear Quadratic control (Cabell *et al.*, 2006) and  $\mathcal{H}_\infty$  loop shaping (Yan *et al.*, 2006) have been used for controller design. For an excellent recent review of the control of cavity oscillations, see Cattafesta *et al.* (2008).

Although many studies on feedback control of cavity oscillations already exist, many of the system identification procedures have been performed for the open-loop unstable system, which means that the *linear* dynamics are masked by non-linearities which will inevitably appear. Furthermore, the linear modeling approach proposed by Rowley *et al.* (2006) has not been fully explored. Since the validity of a linear model is crucial for the design of an effective model-based feedback controller, we make finding an accurate linear model our priority in this chapter. We then compare this dynamical model – found directly from direct numerical simulations using system identification techniques – to that given by the simple linear model proposed by Rowley *et al.* (2006).

## 5.2 CAVITY GEOMETRY AND NUMERICAL METHOD

The two-dimensional, compressible flow past a rectangular cavity is considered. The flow conditions are for a Mach number  $M = 0.6$ , length to depth ratio  $L/D = 2.0$ , a Reynolds number based on momentum thickness  $\theta$  at the cavity leading edge of  $Re_\theta = 56.8$ , and  $L/\theta = 52.8$ .

The flow is solved using direct numerical simulation. The Navier-Stokes equations are non-dimensionalized according to the usual compressible non-dimensionalization – see Rowley (2001) for details. The simulations have been carefully validated using grid resolution and boundary placement studies, together with comparison with experimental data (Rowley *et al.*, 2002). The simulation uses  $240 \times 96$  grid points inside the cavity and  $1008 \times 384$  grid points above the cavity, which is sufficient to resolve all scales at this Reynolds number.

At these conditions, the flow develops into a limit-cycle, with the two most energetic peaks in the spectra occurring at Strouhal numbers of 0.40 and 0.70. These peaks are in reasonable agreement with the first two modes predicted by the semi-empirical

formula of Rossiter (1964):

$$\text{St}_n = \frac{f_n L}{U} = \frac{n - \gamma}{M + 1/\kappa}, \quad n = 1, 2, \dots, \quad (5.1)$$

which predicts the first two modes at Strouhal numbers of 0.32 and 0.74. Here  $n$  is the mode number, and  $\kappa$  and  $\gamma$  are empirical constants corresponding to the average convection speed of disturbances in the shear layer and a phase delay.  $\gamma = 0.25$  and  $1/\kappa = 1.75$  are typical values, and the values used here.

### 5.3 SYSTEM IDENTIFICATION OF THE CAVITY FLOW

We now look at finding the open-loop transfer function of the cavity flow. Since the open-loop system is unstable, the cavity must first be stabilized so that the *linear* open-loop transfer function can be found. Stability is achieved by using a dynamic phasor model, developed for the cavity flow by Rowley & Juttijudata (2005). This dynamic phasor postulates a low-order model that captures the relevant dynamical features of the non-linear, limit-cycling flow using

$$\begin{aligned} \dot{r}(t) &= \sigma r(t) - \alpha r^3(t) \\ \dot{\theta} &= \omega, \end{aligned}$$

which describes oscillations at a frequency  $\omega$ , with constants  $\alpha > 0$  and  $\sigma > 0$ . Then the origin ( $r = 0$ ) is unstable, and there is a stable periodic orbit given by  $r = \sqrt{\sigma/\alpha}$ . For this model, Rowley & Juttijudata (2005) consider a controller whose control signal is a sinusoid at the same frequency as the natural flow, with suitably chosen phase, and slowly varying amplitude. This control signal makes the origin ( $r = 0$ ) globally attracting, at least for the model. It was found that this controller eliminated oscillations in direct numerical simulations, and so we use it for the current system identification.

Figure 5.2(a) shows the cavity geometry. Actuation is provided by a body force  $\rho v$  – where  $\rho$  is the fluid density and  $v$  is a velocity component which is perpendicular to the free-stream – positioned in the shear layer a distance  $L/20$  from the cavity upstream corner. Three pressure sensors are used in total and measure the pressure half-way up

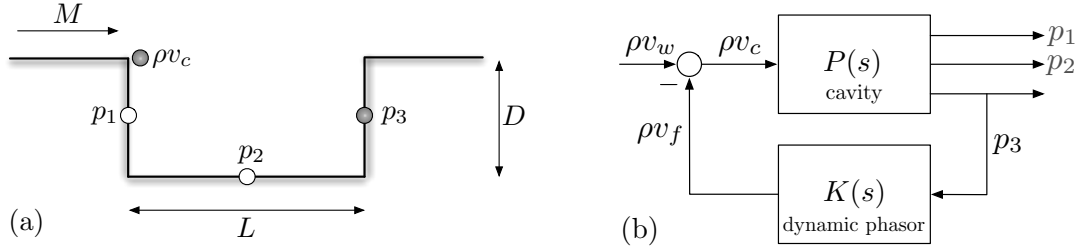


FIGURE 5.2: System identification: (a) the cavity geometry showing the location of the body force and the pressure sensors, and (b) the corresponding closed-loop block diagram.

the upstream wall (denoted  $p_1$ ), half-way along the cavity floor (denoted  $p_2$ ) and half-way up the downstream wall (denoted  $p_3$ ).

Figure 5.2(b) shows the feedback arrangement used for system identification. The pressure measured on the downstream wall ( $p_3$ ) is used as the feedback signal for the dynamic phasor. The total body force at the input is given by  $\rho v_c = \rho v_w - \rho v_f$  (negative feedback convention), where  $\rho v_w$  is a broadband forcing signal and  $\rho v_f$  is the feedback control signal from the dynamic phasor.<sup>1</sup> Taking the total body force  $\rho v_c$  and the pressure vector  $\mathbf{p} = [p_1 \ p_2 \ p_3]^T$  as the system input and output, the cavity's open-loop transfer function  $P(s) = [P_1(s) \ P_2(s) \ P_3(s)]^T$  can be found, where

$$[p_1 \ p_2 \ p_3]^T = [P_1(s) \ P_2(s) \ P_3(s)]^T \rho v_c.$$

(If instead the broadband signal  $\rho v_w$  was used as the system input, the closed-loop, stabilized transfer function would be recovered.)

Using  $\rho v_c$  and  $\mathbf{p}$  as the input-output pair as described, spectral analysis can be used to find the cavity's open-loop transfer function. Tests were performed to ensure that the forced cavity was behaving linearly for the forcing amplitudes used. This was achieved using a sum of two sinusoids at the input, the frequencies of which were chosen to match the frequencies of the two unstable modes, since it was reasoned that non-linearities were most likely to first appear when forcing at these frequencies.

The open-loop transfer functions found for the three sensor locations are shown in figure 5.3. At all three pressure probe locations, the first three Rossiter modes are

<sup>1</sup> $\rho v_w$  is band-limited to avoid aliasing – where high frequency components can masquerade as lower frequencies. Despite this, its bandwidth still extends well above the frequencies of interest.

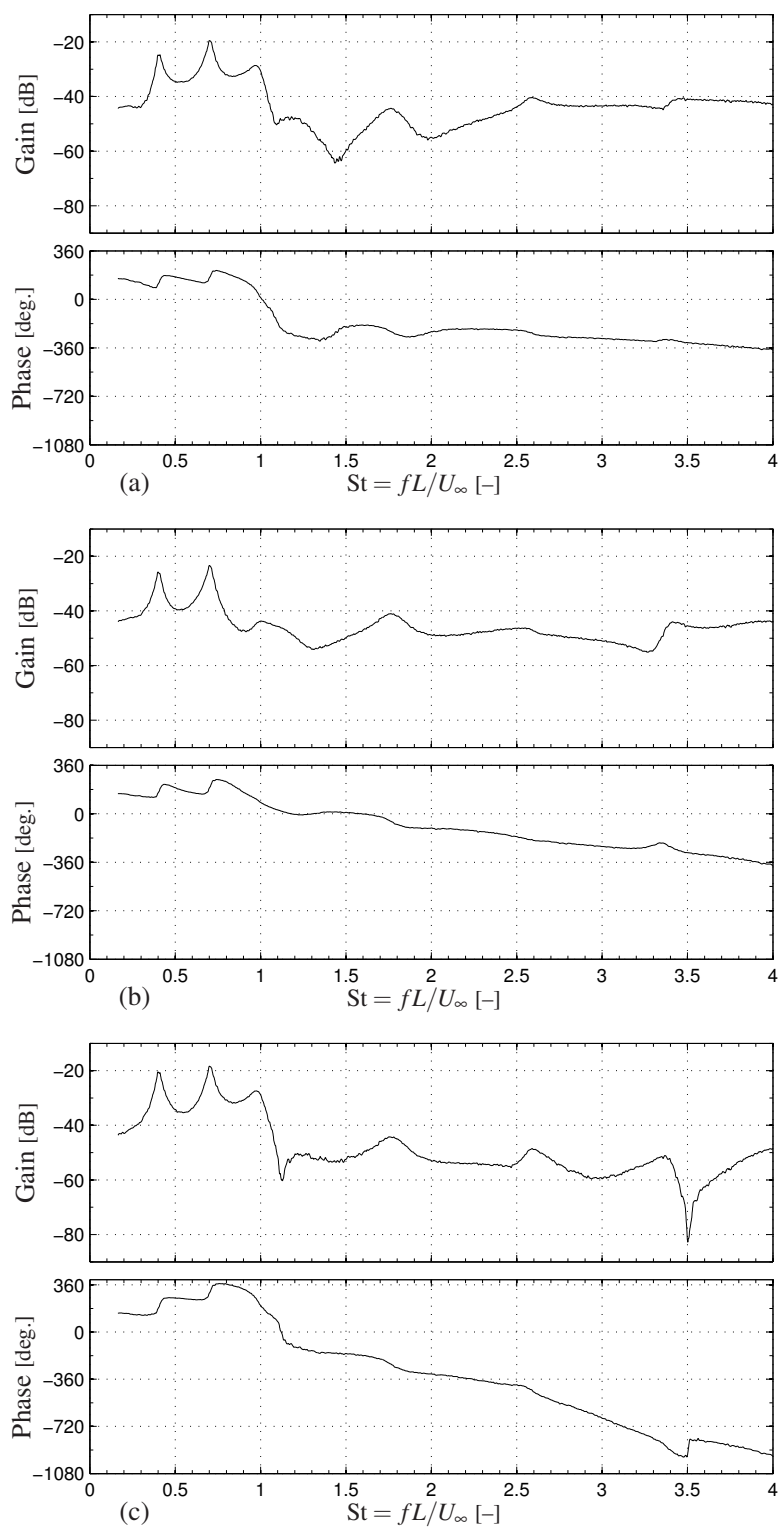


FIGURE 5.3: Transfer functions measured from direct numerical simulations: (a) for pressure probe 1,  $P_1(s)$ ; (b) for pressure probe 2,  $P_2(s)$ ; and (c) for pressure probe 3,  $P_3(s)$ .

seen at Strouhal numbers of 0.40, 0.70 and 0.98. These values agree with those found by Rowley *et al.* (2002) for a Mach number of 0.6, and show reasonable agreement with Rossiter's formula (5.1), which predicts Strouhal numbers of 0.32, 0.74 and 1.17. The phase increase seen across the first and the second Rossiter modes indicates that these two modes are unstable (Dorf & Bishop, 2005), which explains their dominance in the open-loop spectra. The third Rossiter mode is stable, since one observes a phase decrease across it.

We note briefly here the identified system's time delay. Since the transfer function of a pure time delay of duration  $\tau$  is  $e^{-s\tau}$ , a time delay introduces a negative gradient to a transfer function's phase: from this gradient, a system's time delay can be deduced. The time delay seen at high frequencies in figure 5.3 will be explained in more detail in § 5.4.3.

#### 5.4 LINEAR MODELS FOR CONTROL OF CAVITY OSCILLATIONS

Rowley *et al.* (2006) propose a linear model for cavity oscillations. The model, composed of four constituent transfer functions, is of low-order and is intended for feedback control design purposes. Each of the constituent transfer functions corresponds to one of the four elements in the mechanism first described by Rossiter (1964): the amplification of disturbances by the free shear layer; the scattering of the disturbances into pressure fluctuations at the downstream corner; the propagation of these pressure fluctuations inside the cavity; and the receptivity to pressure perturbations at the upstream corner. A block diagram of the linear model is shown in figure 5.4. The 'o' and 'L' subscripts correspond to the upstream and downstream corners respectively.

The open-loop transfer function given by the linear model – which is between the body force and the pressure at the upstream corner – is given by

$$\hat{P}_1(s) = \frac{p_o(s)}{\rho v_o(s)} = \frac{G(s)S(s)A(s)}{1 - G(s)S(s)A(s)R(s)}. \quad (5.2a)$$

If we are interested in a pressure measurement at the downstream corner ( $p_L$  in figure

5.4), then we instead have

$$\hat{P}_3(s) = \frac{p_L(s)}{\rho v_o(s)} = \frac{G(s)S(s)}{1 - G(s)S(s)A(s)R(s)}. \quad (5.2b)$$

(We use the subscripts 1 & 3, together with a hat, to indicate that these are approximations of the transfer functions at probe locations 1 & 3.)

Since open-loop transfer functions have been measured from direct numerical simulations of the cavity, it is possible to compare these measured transfer functions with those given by the linear model (5.2). (The measured transfer functions  $P_1(s)$  and  $P_3(s)$  involve pressure measurements half-way along the upstream and downstream walls, whilst the linear models (5.2a) and (5.2b) give the transfer functions at the upstream and downstream corners, but this should make little difference, especially when the linear model only considers the longitudinal behaviour of the cavity.)

Furthermore, since flow data are available at regular intervals throughout the computational domain, it is possible to use the same system identification methods to find approximations to the four constituent transfer functions, and these can be used to inform the choice of the linear model's constituent transfer functions in figure 5.4.

#### 5.4.1 CONSTITUENT TRANSFER FUNCTIONS

We now look at each of the four constituent transfer functions in turn. The method for approximating each transfer function from direct numerical simulations is explained,

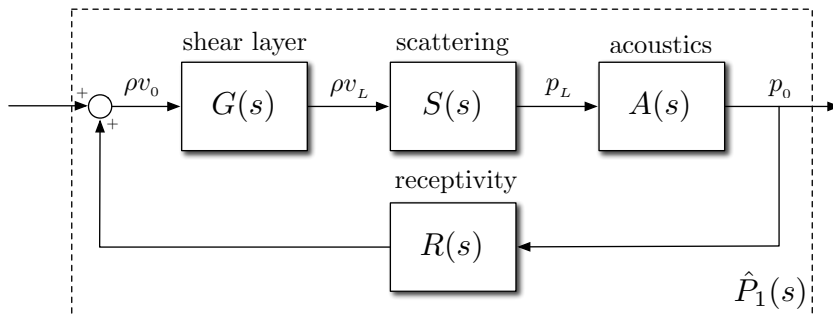


FIGURE 5.4: Linear model of the cavity flow proposed by Rowley *et al.* (2006). The ‘o’ and ‘L’ subscripts used correspond to the upstream and downstream corners respectively.

and the measured constituent transfer function is used to choose the parameters of the linear model of Rowley *et al.* (2006). Finally, the overall open-loop system is treated: the measured open-loop transfer functions (figures 5.3(a) & 5.3(c)) are compared with those given by the feedback interconnection of the four constituent transfer functions  $G(s)$ ,  $S(s)$ ,  $A(s)$  and  $R(s)$  given by equations (5.2a) & (5.2b).

Each constituent transfer function is measured in direct numerical simulations using the same spectral method that was used to find the overall open-loop transfer function  $P(s)$  in § 5.3. For the linear model, the parameters stated are all non-dimensionalized by Strouhal number. For a time delay, for example, the non-dimensional value that is stated,  $\tau$ , is related to the dimensional value,  $\tau^d$  by  $\tau = \tau^d U/L$ , where  $U$  is the free-stream velocity.

#### *Shear layer*

The shear layer transfer function  $G(s)$  describes the amplification of velocity perturbations at the upstream corner as they travel downstream. Therefore the input and output are taken at the upstream corner and downstream corner respectively. Since the input used for control is a body force  $\rho v$  rather than a velocity (figure 5.2(b)), we include the density in the input and output.

The shear layer transfer function can be found using linear stability theory. As a simpler alternative for a linear model, Rowley *et al.* (2006) propose using a second-order system with a time delay:

$$G(s) = \frac{\rho v_L(s)}{\rho v_o(s)} = k_g \frac{\omega_o^2}{s^2 + 2\zeta \omega_o s + \omega_o^2} e^{-s\tau_g}. \quad (5.3)$$

Figure 5.5 compares the measured shear layer transfer function to that given by the linear model (5.3) for  $k_g = 3.35$ ,  $\omega_o = 3.44$ ,  $\zeta = 0.07$  and  $\tau_g = 1.43$  (which corresponds to  $\kappa = 0.70$  in Rossiter's formula (5.1)). The model transfer function captures the important dynamical features of the shear layer: near-unity gain at low frequencies; amplification of disturbances at mid-frequencies; attenuation of disturbances at high frequencies; and an appropriate phase. (The phase is given by the time delay  $\tau_g$ , the time taken for a disturbance generated at the upstream corner to propagate to the

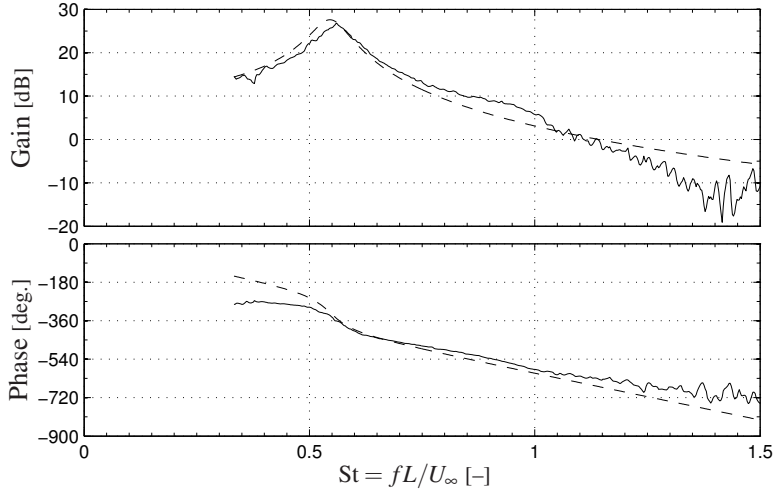


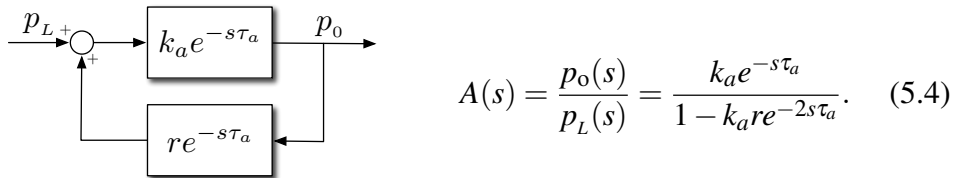
FIGURE 5.5: Shear layer transfer function  $G(s)$ : measured from direct numerical simulation (—); and approximated as a second-order transfer function with time delay (---).

downstream corner.) One observes that the maximum gain, cross-over frequency and phase characteristics are all well-captured by the model.<sup>1</sup>

### Acoustics

The acoustic transfer function  $A(s)$  relates pressure perturbations at the downstream corner,  $p_L$ , to pressure perturbations at the upstream corner,  $p_o$ , and so the pressures at these two locations are used as input and output for the measured transfer function.

The linear model accounts for longitudinal acoustic cavity resonances by modeling acoustic propagation and reflection in the cavity:



An acoustic wave generated at the downstream corner propagates upstream. Some of it reflects off the upstream wall, propagates downstream, and arrives back at the downstream wall, where it is again reflected. The coefficients  $k_a$  and  $r$  measure the total efficiency of the reflection process, including losses to the far-field. The time

<sup>1</sup>The cross-over frequency is the frequency at which the gain passes through 0 dB.

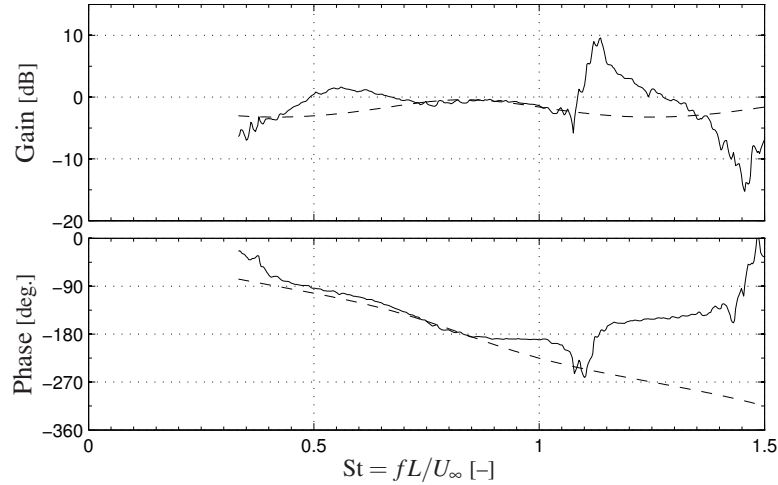


FIGURE 5.6: Acoustic transfer function  $A(s)$ : measured from direct numerical simulation (—); and approximated as a time delay with reflection (---).

delay  $\tau_a$  represents the time taken for an acoustic wave to propagate the length of the cavity.

Figure 5.6 compares the measured acoustic transfer function with that given by the linear model (5.4) for  $k_a = 0.8$ ,  $r = 0.16$  and  $\tau_a = 0.60$ . (This acoustic time delay is the value expected and, in its non-dimensional form, is given simply by the Mach number  $M$ .) One observes reasonable agreement, with the phase characteristics more well-captured than the gain. It is likely that the discrepancy in the gain at lower frequencies is caused by the acoustic field generated by the shear layer's evolving vorticity. The frequency at which the greatest discrepancy is seen coincides with the frequency at which the shear layer's gain is largest, which seems to support this observation.

We briefly note the behaviour of  $A(s)$  at high frequencies here. Above Strouhal numbers of approximately 1.0, the gain of  $A(s)$  is poorly captured by the linear model, and the phase of the measured  $A(s)$  has a *positive* gradient, which suggests a *negative* time delay. We will see similar behaviour for the scattering and receptivity transfer functions: that the agreement between what is measured and the linear model is poor above Strouhal numbers of approximately 1.0. An explanation for all of these observations is given in § 5.4.3.

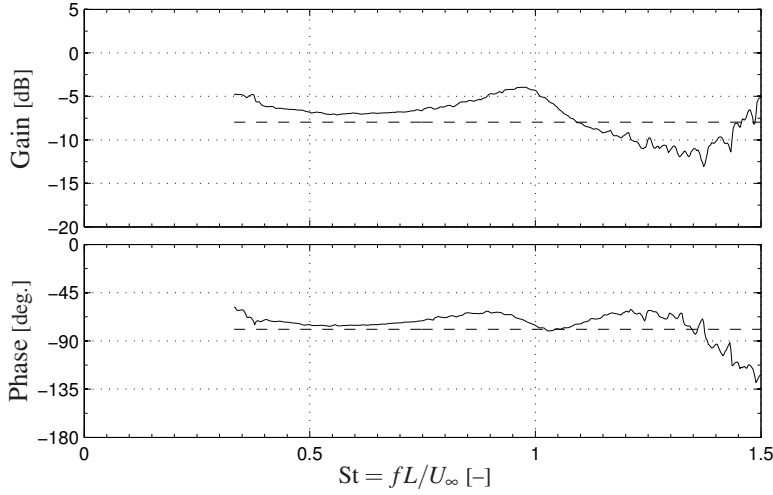


FIGURE 5.7: Scattering transfer function  $S(s)$ : as extracted from direct numerical simulation (—); and approximated as a complex-valued constant (---).

### Scattering

The scattering transfer function  $S(s)$  describes the generation of acoustic waves when velocity perturbations impinge on the downstream corner. Therefore we use the quantity  $\rho v_L$  and the pressure  $p_L$  at the downstream corner as the input and output for the measured transfer function.

The scattering transfer function is modeled as a constant gain and constant phase lag:

$$S(s) = \frac{p_L(s)}{\rho v_L(s)} = k_s e^{-i2\pi\theta_s}. \quad (5.5)$$

Figure 5.7 compares the measured scattering transfer function with that given by the linear model (5.5) for  $k_s = 0.40$  and  $\theta_s = 0.22$ . Whilst the model is crude, its constant gain and phase lag give reasonable agreement up to Strouhal numbers of about 1.0.

### Receptivity

The receptivity transfer function  $R(s)$  describes the perturbations in  $\rho v$  generated by incident pressure perturbations at the upstream corner. Therefore we use the quantities  $p_o$  and  $\rho v_o$  as the input and output for the measured transfer function.

The receptivity transfer function is modeled as a constant gain and constant phase

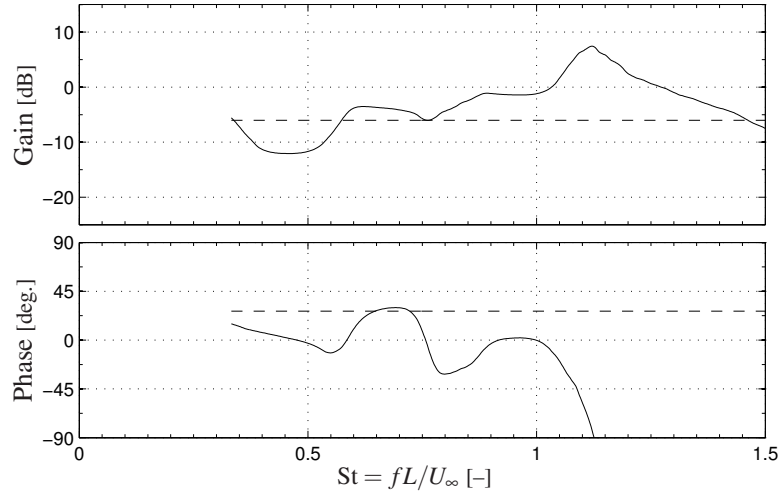


FIGURE 5.8: Receptivity transfer function  $R(s)$ : as extracted from direct numerical simulation (—); and approximated as a complex-valued constant (---).

lag:

$$R(s) = \frac{\rho v_o(s)}{p_o(s)} = k_r e^{-i2\pi\theta_r}. \quad (5.6)$$

Figure 5.8 compares the measured receptivity transfer function with that given by the linear model (5.6) for  $k_r = 0.50$  and  $\theta_r = -0.074$ . Again, whilst crude, the model's constant gain and phase lag give reasonable agreement up to Strouhal numbers of about 1.0.

#### 5.4.2 OVERALL LINEAR MODEL

By using the linear model's four constituent transfer functions in the feedback arrangement shown in figure 5.4, a low-order model for the overall cavity flow can be formed. Using (5.2), we can do this for a pressure measurement on the upstream wall,  $\hat{P}_1(s)$  and on the downstream wall,  $\hat{P}_3(s)$ .

We now compare the transfer functions given by the linear model at these two measurement locations,  $\hat{P}_1(s)$  and  $\hat{P}_3(s)$ , to those measured directly,  $P_1(s)$  and  $P_3(s)$ . The comparison for both transfer functions is shown in a Bode diagram in figure 5.9, and in a Nyquist diagram in figure 5.10. It is clear from both figures that, over the frequency range of the first two Rossiter modes, the agreement is very good for both transfer functions. This is encouraging, since it is the dynamics over this frequency

range, where the open-loop gain is the largest, that drives the design of a model-based controller. The third Rossiter mode, however, is not well-captured by the linear model. We now look at understanding these findings in terms of the *loop gain*.

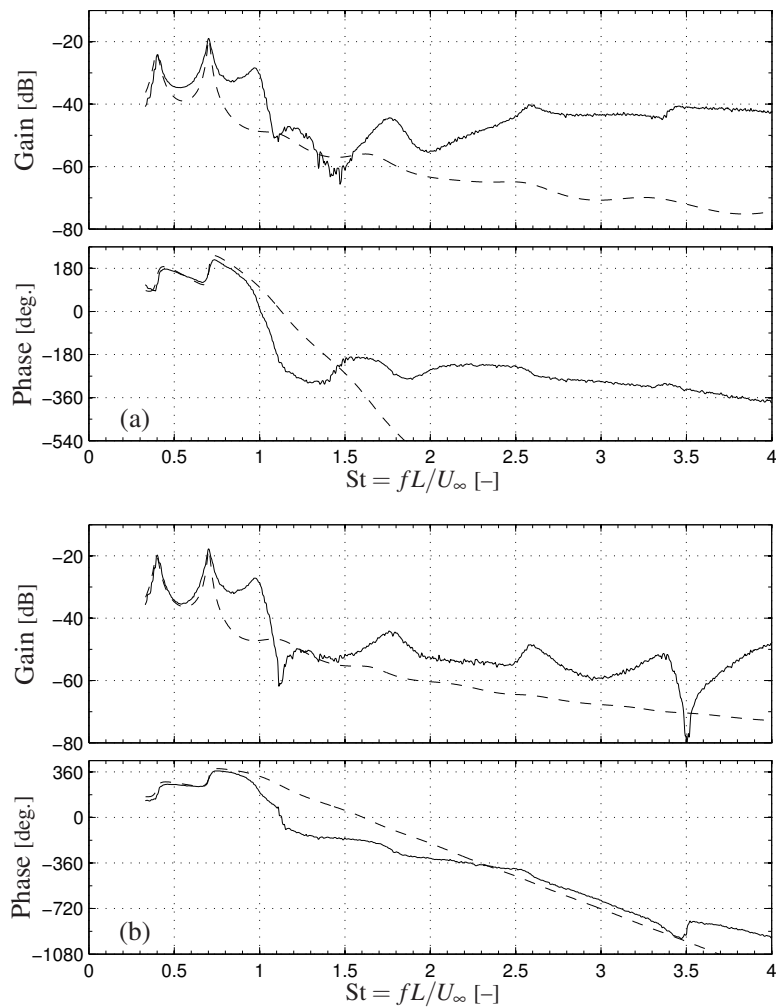


FIGURE 5.9: Bode diagram comparison of the open-loop transfer function: (a) for probe 1,  $P_1(s)$ ; and (b) for probe 3,  $P_3(s)$ . In both plots, the transfer function measured from direct numerical simulation (—) is compared with that given by the linear model (---).

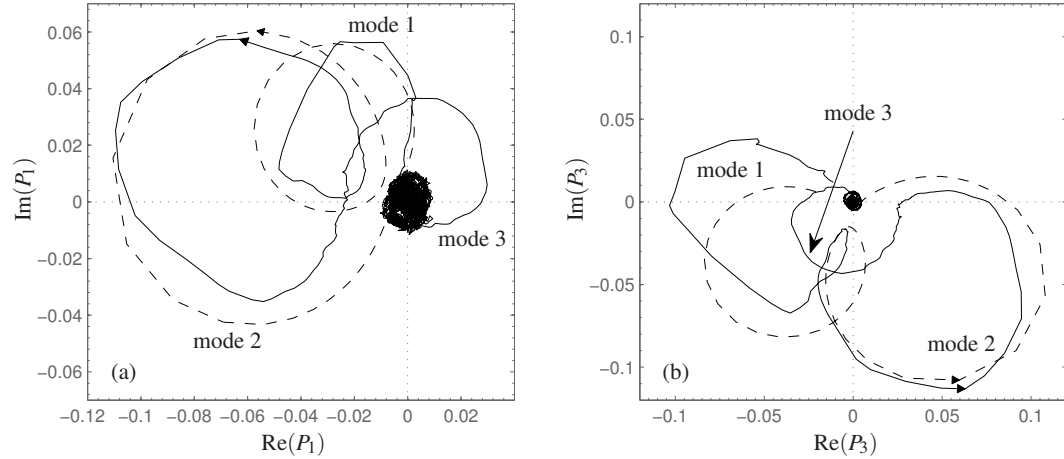


FIGURE 5.10: Nyquist diagram comparison of the open-loop transfer function (positive frequencies only): (a) for probe 1,  $P_1(s)$ ; and (b) for probe 3,  $P_3(s)$ . In both plots, the transfer function measured from direct numerical simulation (—) is compared with that given by the linear model (---). The three Rossiter modes are also indicated.

#### *Importance of the loop gain*

The behaviour of the linear model can be explained in terms of its *loop gain*  $L(s)$ , where

$$L(s) = G(s)S(s)A(s)R(s).$$

This appears in the denominator of both transfer functions in (5.2), from which it is clear that the linear model's poles occur at those frequencies satisfying  $L(s) = 1$ . This can only be satisfied when the phase of the loop gain satisfies  $\angle L(s) = 0^\circ, -360^\circ, \dots$ , and this condition gives the frequencies of the linear model's modes. Then the *stability* of a mode is determined by the magnitude of the loop gain at that frequency: if the loop gain is less than one, the mode is stable, whilst if the loop gain is greater than one, the mode is unstable.

Therefore the success in predicting the first and second Rossiter modes can be explained – in terms of the linear model at least – by the correct prediction of the loop gain  $L(s)$  at those frequencies.

Similarly, the loop gain can be used to explain the poor prediction of the third Rossiter mode. The linear model predicts a third Rossiter mode at a Strouhal number

of 1.15, which is higher than that seen in simulations. The loop gain at this Strouhal number is very low, so that the third Rossiter mode is highly damped, and is therefore hardly visible in the linear model's transfer function. Since the loop gain decreases with increasing frequency, the over-prediction of the third Rossiter mode's frequency has a negative impact on the prediction of the loop gain for the third Rossiter mode, and so the prediction of both its frequency and its loop gain is poor.

#### *Link to Rossiter's formula*

Setting  $G(s) = e^{-s\tau_g}$ , assuming  $S(s) = e^{-i2\pi\gamma}$  and  $R(s) = 1$ , and letting  $k_a = 1$  and  $r = 0$  (no reflection) in (5.4) to give  $A(s) = e^{-s\tau_a}$ , the predicted open-loop transfer function for pressure probe 1 becomes

$$\hat{P}_1(s) = \frac{e^{-i2\pi\gamma} e^{-s(\tau_g + \tau_a)}}{1 - e^{-i2\pi\gamma} e^{-s(\tau_g + \tau_a)}}$$

which has poles at  $s = i\omega_n$ , with

$$\text{St}_n = \frac{f_n L}{U} = \frac{n - \gamma}{M + 1/\kappa}, \quad n = 1, 2, \dots,$$

and so we recover Rossiter's formula (5.1).<sup>1</sup>

It is now clear why Rossiter's formula can only predict the cavity's resonant frequencies and not their growth rates: the loop gain in this case is given by  $L(s) = e^{-i2\pi\gamma} e^{-s(\tau_g + \tau_a)}$ , the magnitude of which is always one.

#### 5.4.3 HIGH-FREQUENCY DYNAMICS

The linear model used shows reasonable success in predicting the gain and phase characteristics of the open-loop cavity flow over the frequency range of the Rossiter tones. Clearly this linear model is useful for feedback control design purposes. However, the linear model over-predicts the time delay for pressure probe 1 at higher frequencies (figure 5.9(a)), and we seek an explanation for this.

<sup>1</sup>In fact, the constant phase change given by  $\gamma$  can be arbitrarily apportioned between  $S(s)$  and  $R(s)$  with no change in the predicted resonant frequencies.

The linear model neglects the acoustic field generated by the body force  $\rho v_c$  directly. At low frequencies, this is perfectly valid: the acoustics generated by the Rossiter mechanism dominate, and the effect of the body force's direct acoustic field is negligible. At higher frequencies, though, the shear layer attenuates disturbances rather than amplifying them, i.e.  $|G(s)| < 1$ . This means that the velocity fluctuations arriving at the downstream corner are very small, and the Rossiter mechanism is cut-off. Indeed, these considerations lead to a convenient definition of 'low frequencies' and 'high frequencies': low frequencies are those for which the shear layer amplifies disturbances, whilst high frequencies are those for which disturbances are attenuated. (From figure 5.5, the cross-over frequency of the shear layer – where the magnitude of  $G(s)$  passes through 0 dB – is at a Strouhal number of about 1.1.)

This explains the positive gradient of the acoustic transfer function's phase seen in figure 5.6. At frequencies above the shear layer's cross-over frequency, the body force dominates the acoustic field. Since the body force is much closer to the upstream corner than to the downstream corner, the effect of the body force is seen at  $p_o$  before it is seen at  $p_L$ , and this corresponds to  $A(s) = p_o(s)/p_L(s)$  having a *negative* time delay. The acoustic transfer function makes clear what is true for all four constituent transfer functions: it is only valid to seek them over the frequency range at which the Rossiter modes can occur, i.e. at frequencies where  $|G(s)| > 1$ . To do so at higher frequencies is to seek a mechanism that no longer exists, the open-loop dynamics being instead dominated by the acoustics directly generated by the body force  $\rho v_c$ . This helps to explain the poor agreement seen at higher frequencies between measurements and the linear model for the transfer functions representing the acoustics  $A(s)$ , scattering  $S(s)$  and the receptivity process  $R(s)$ .

We now look at a simple modification to the linear model to better capture this high-frequency behaviour for probe 1. (For brevity's sake we omit probe 3, although the same analysis can be performed.) In particular, the modification correctly predicts the system time delay at high frequencies. The modified linear model is shown in figure 5.11. A transfer function to model the acoustics generated by the body force

directly,  $B(s)$ , is introduced. The transfer function that we choose is

$$B(s) = k_b e^{-s\tau_b}, \quad (5.7)$$

where  $k_b$  is a gain and  $\tau_b$  is the time taken for an acoustic wave, generated by the body force, to propagate to the pressure sensor location of interest – in this case probe 1.

The linear model's open-loop transfer function for pressure probe 1 is now given by

$$\hat{P}_1(s) = \frac{G(s)S(s)A(s) + B(s)}{1 - G(s)S(s)A(s)R(s)}.$$

At low frequencies,  $B(s)$  is negligible and we recover (5.2a). At high frequencies,  $|G(s)| \ll 1$  and we have simply  $P(s) = B(s)$ .

The Bode diagram of the modified linear model's transfer function, together with that found in direct numerical simulations, is shown in figure 5.12. The parameter values chosen are  $\tau_b = 0.15$ , which is the anticipated acoustic time delay between the body force and probe location 1, and  $k_b = 0.33$ . One observes that the model's prediction of the Rossiter modes remains intact, and that the high-frequency dynamics at probe 1 are more well-captured, in particular the time delay (given by the gradient of the phase plot). Furthermore, this model is able to capture *zeros* of the transfer function as well as the poles - this is explored in more detail in § 5.5.1.

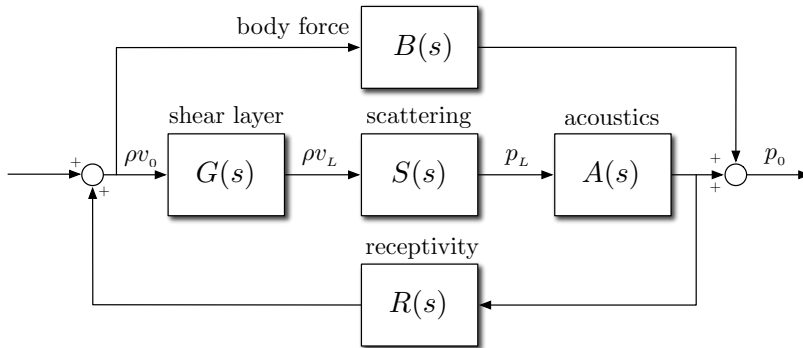


FIGURE 5.11: Modified linear model to account for the acoustic field generated by the body force directly.

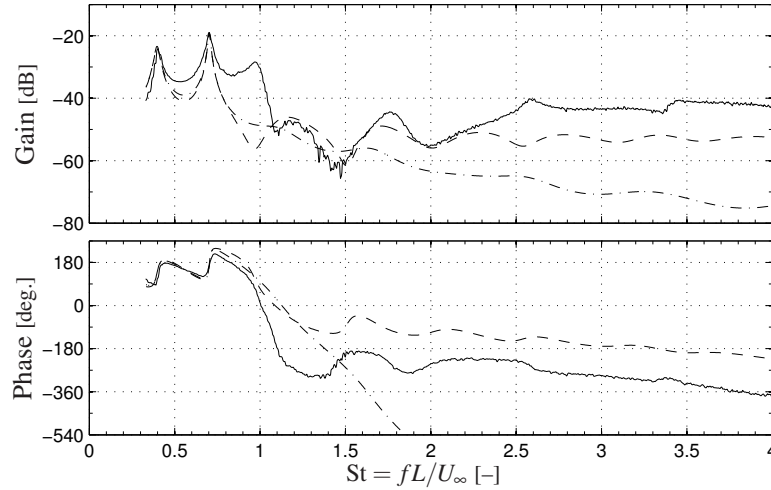


FIGURE 5.12: Bode diagram comparison of the modified open-loop transfer function for probe 1: as extracted from direct numerical simulation (—); and approximated by the modified linear model (---). The original linear model is also shown (-·-) for comparison.

## 5.5 PROPERTIES OF THE CAVITY TRANSFER FUNCTION

The results of § 5.4.1 suggest that, for suitable choice of constituent transfer functions, a linear model of the form

$$\hat{P}_1(s) = \frac{G(s)S(s)A(s) + B(s)}{1 - G(s)S(s)A(s)R(s)} \quad (5.8)$$

is useful for feedback control purposes.

We now develop an explicit expression for this transfer function based on the constituent transfer functions used in § 5.4.1. We focus on the transfer function for probe location 1,  $\hat{P}_1(s)$ , because this corresponds most closely to the pressure signal that we will use for adaptive feedback control in chapter 6. The same results regarding the locations of the zeros and the transfer function's relative degree still hold for probe location 3, however (which is the probe location that we will use for linear quadratic control, also in chapter 6).

Since the scattering and receptivity transfer functions are modeled simply as complex constants, we set  $S(s) = \Lambda_s$  and  $R(s) = \Lambda_r$ . We write the shear layer transfer function (5.3) as the product of a rational transfer function  $G_o(s)$  and a pure time de-

lay:

$$G(s) = G_o(s)e^{-s\tau_g}.$$

Substituting these expressions, together with the transfer functions for the acoustics (5.4) and for the body force (5.7), into (5.8) gives

$$\hat{P}_1(s) = \frac{k_a\Lambda_s G_o(s)e^{-s(\bar{\tau}-\tau_b)} + k_b(1 - k_a r e^{-2s\tau_a})}{-k_a\Lambda_s\Lambda_r G_o(s)e^{-s\bar{\tau}} + (1 - k_a r e^{-2s\tau_a})} e^{-s\tau_b} \quad (5.9)$$

$$= P_o(s)e^{-s\tau_b}, \quad (5.10)$$

where in (5.9) we have introduced  $\bar{\tau} = \tau_g + \tau_a$ . The body force's acoustic delay  $\tau_b$  has been removed from the numerator of  $\hat{P}_1(s)$  in (5.9) and appears as a pure time delay. (This can be done because the shear layer time delay  $\tau_g$  will always be larger than the body force's acoustic delay  $\tau_b$ .) Thus  $\hat{P}_1(s)$  is written as the product of some transfer function  $P_o(s)$  and a pure time delay in (5.10).

We now use this model to look at two important properties of the cavity flow's transfer function: the location of its zeros; and its relative degree. These two properties will be important for the adaptive controller used in chapter 6.

### 5.5.1 TRANSFER FUNCTION ZEROS

We have already seen in chapters 2 & 3 that the location of the zeros of the open-loop system are important for adaptive control. Specifically, any zeros must lie in the left half-plane. We first note that without the body force  $B(s)$ , the zeros of (5.2a) are given by

$$G(s)S(s)A(s) = 0. \quad (5.11)$$

Since none of the transfer functions  $G(s)$ ,  $S(s)$  or  $A(s)$  possess any zeros, (5.11) is never satisfied, and the original linear model does not model any zero dynamics of the system. With the body force modification made, the zeros of (5.8) are given by

$$G(s)S(s)A(s) + B(s) = 0,$$

and zeros occur whenever  $G(s)S(s)A(s) = -B(s)$ . Then from equation (5.9), the zeros of  $\hat{P}_1(s)$  are given by the roots of

$$k_a \Lambda_s G_o(s) e^{-s(\bar{\tau} - \tau_b)} + k_b (1 - k_a r e^{-2s\tau_a}) = 0. \quad (5.12)$$

First consider the case where  $r \rightarrow 0$ , which physically corresponds to neglecting the reflection of acoustic waves inside the cavity. Then (5.12) simplifies to

$$k_a \Lambda_s G_o(s) e^{-s(\bar{\tau} - \tau_b)} + k_b = 0. \quad (5.13)$$

We are interested in whether the (complex-valued) roots  $\lambda = \sigma + i\omega$  of (5.13) lie in the left half-plane ( $\sigma < 0$ ) or in the right half-plane ( $\sigma > 0$ ). This amounts to looking at the magnitude of (5.13), since  $|e^{-i\omega(\bar{\tau} - \tau_b)}| = 1$ :

$$|e^{-s(\bar{\tau} - \tau_b)}| = e^{-\sigma(\bar{\tau} - \tau_b)} = \frac{|k_b|}{k_a |\Lambda_s| |G_o(s)|}, \quad (5.14)$$

and we see that, in this simplified case, the position of the zeros depends on the shear layer's gain, and is therefore frequency-dependent. We expect  $|k_b/k_a \Lambda_s| \approx 1$ . Therefore at low frequencies where  $|G_o(s)| > 1$ , we expect  $e^{-\sigma(\bar{\tau} - \tau_b)} < 1$  at the zeros, and any zeros are likely to be in the right half-plane ( $\sigma > 0$ ). At high frequencies where  $|G_o(s)| < 1$ , we expect  $e^{-\sigma(\bar{\tau} - \tau_b)} > 1$ , and any zeros are likely to be in the left half-plane ( $\sigma < 0$ ).

If we now include the effect of the downstream reflection coefficient  $r$ , the zeros of (5.9) are given by

$$|e^{-s(\bar{\tau} - \tau_b)}| = \frac{|k_b| |1 - k_a r e^{-2s\tau_a}|}{k_a |\Lambda_s| |G_o(s)|}, \quad (5.15)$$

and the same argument applies: right half-plane zeros are more likely at low frequencies; and left half-plane zeros are more likely at high frequencies.<sup>1</sup>

These observations are supported by the transfer functions found at probe locations 1 & 3 in figures 5.3(a) & 5.3(c). Both transfer functions have zeros at a Strouhal number

<sup>1</sup>It is instructive to consider that when  $|G_o(s)| > 1$ , equation (5.12) is dominated by the first term  $k_a \Lambda_s G_o(s) e^{-s(\bar{\tau} - \tau_b)}$ . Whilst this has no zeros, the pure time delay  $e^{-s(\bar{\tau} - \tau_b)}$  acts in a similar way to right half-plane zeros (by making the term  $k_a \Lambda_s G_o(s) e^{-s(\bar{\tau} - \tau_b)}$  non-minimum phase).

of around 1.1, at which point the shear layer has approximately unity gain. The phase decrease across these zeros indicates that they are in the right half-plane. On the other hand, probe 3 also has a pair of zeros at a Strouhal number of around  $St = 3.5$ , by which point the shear layer transfer function satisfies  $|G(s)| \ll 1$ . The phase increase across these zeros indicates that they are in the left half-plane.

From (5.15), the shear layer transfer function  $G(s)$  is important in determining the zeros of  $\hat{P}_1(s)$ . It is worth pointing out that the result concerning their locations holds for any shear layer transfer function  $G(s)$  – provided that its gain is greater than one at low frequencies and decreases at high frequencies – and is not exclusive to the second-order model (5.3) chosen.

### 5.5.2 RELATIVE DEGREE

Recall that for a rational transfer function  $P_o(s)$ , written as the ratio of two coprime, monic polynomials

$$P_o(s) = k_o \frac{N_o(s)}{D_o(s)},$$

its relative degree  $n^*$  is defined as the degree of its denominator polynomial  $D_o(s)$  minus the degree of its numerator polynomial  $N_o(s)$ :

$$n^*[P_o(s)] = \deg[D_o(s)] - \deg[N_o(s)]. \quad (5.16)$$

We now see that the relative degree of  $\hat{P}_1(s)$  – when approximated by the product of a rational transfer function  $P_o(s)$  and a pure time delay – is zero, and we see it in two ways. The first involves using the specific linear model of § 5.4, and the second is based on some more general assumptions about the constituent transfer functions.

#### *Based on the derived linear model*

From (5.9),  $P_o(s)$  for the cavity flow is not a rational transfer function. Therefore we first form a rational approximation  $P_o^r(s)$ . Following Evesque *et al.* (2003b), we do this using Padé approximants. For some function  $f(s)$ , an  $[L, M]$ th-order Padé approximant of  $f(s)$  is a rational function whose numerator has order  $L$  and denominator has order

$M$ . The rational function matches the first  $(L + M + 1)$  terms of the power series of  $f(s)$ , and therefore its range of validity increases as  $L$  and  $M$  increase. We use the notation  $[L/M]_{f(s)}$  for this Padé approximant. For a pure time delay, which has unity gain at all frequencies, we choose  $L = M$ . Then the poles of the resulting Padé approximant are complex conjugates of its zeros, and  $[M/M]_{f(s)}$  has unity gain at all frequencies as required. The phase of the approximation will be well-matched over some frequency range, and this range increases with the order of the Padé approximant, but will deviate asymptotically.

Replacing each of the delay terms in  $P_o(s)$  with an  $[M, M]$ th-order Padé approximant  $[M/M]_{f(s)}$ , and writing  $G_o(s)$  as  $G_o(s) = k_g \omega_0^2 / D_G(s)$  (with  $D_G(s) = s^2 + 2\zeta \omega_0 s + \omega_0^2$ ) gives the rational approximation  $P_o^r(s)$ :

$$P_o^r(s) = \frac{k_a k_g \omega_0^2 \Lambda_s [M/M]_{e^{-s(\bar{\tau}-\tau_b)} + k_b D_G(s) (1 - k_a r [M/M]_{e^{-2s\tau_a}})}{-k_a k_g \omega_0^2 \Lambda_s \Lambda_r [M/M]_{e^{-s\bar{\tau}}} + D_G(s) (1 - k_a r [M/M]_{e^{-2s\tau_a}})}. \quad (5.17)$$

The relative degree of this expression is zero. This can be seen by observing that in the limit  $\omega \rightarrow \infty$ ,

$$\lim_{\omega \rightarrow \infty} P_o^r(i\omega) = \frac{k_b D_G(i\omega) (1 - k_a r [M/M]_{e^{-2i\omega\tau_a}})}{+D_G(i\omega) (1 - k_a r [M/M]_{e^{-2i\omega\tau_a}})} = k_b,$$

and a finite gain at infinite frequency implies a relative degree of zero. Here we have assumed that  $G_o(s) = k_g \omega_0^2 / (s^2 + 2\zeta \omega_0 s + \omega_0^2)$ , but the result holds for any shear layer transfer function with a relative degree of one or greater.

*Based on some more general assumptions*

The result above was derived for the specific model of the cavity flow given by the constituent transfer functions (5.3–5.6), and by using Padé approximants. The question now arises: is it possible to arrive at the same result using some more general assumptions about the constituent transfer functions? We will now see that it is. Consider again equation (5.8). Let  $G(s)S(s)R(s) = \Psi(s)$ , giving

$$\hat{P}_1(s) = \frac{\Psi(s) + B(s)}{1 - \Psi(s)R(s)}.$$

Now represent each constituent transfer function as the ratio of two polynomials. Then  $\Psi(s) = N_\Psi(s)/D_\Psi(s)$ , for example, and  $\hat{P}_1(s)$  can be written as<sup>1</sup>

$$\hat{P}_1 = \frac{N_\Psi D_R D_B + N_B D_\Psi D_R}{D_\Psi D_R D_B - N_\Psi N_R D_B} \quad (5.18)$$

$$= \frac{D_R}{D_B} \left( \frac{N_\Psi D_B + N_B D_\Psi}{D_\Psi D_R - N_\Psi N_R} \right). \quad (5.19)$$

We want to find the relative degree of this expression. By (5.16), this is

$$\begin{aligned} n^*(\hat{P}_1) = & \deg(D_\Psi D_R - N_\Psi N_R) + \deg(D_B) \\ & - \deg(D_\Psi N_B + N_\Psi D_B) - \deg(D_R). \end{aligned} \quad (5.20)$$

We now make two assumptions on the relative degree of the constituent transfer functions:

- (i) the transfer functions  $\Psi(s) = G(s)S(s)A(s)$  and  $R(s)$  are *strictly proper* transfer functions – that is, they have a relative degree of one or greater.
- (ii) the body force transfer function  $B(s)$  has a relative degree of zero.

These two assumptions are physically motivated. The gain of a strictly proper transfer function satisfies  $|P(i\omega)| \rightarrow 0$  as  $\omega \rightarrow \infty$ . Because of viscosity, we expect the pressure perturbations generated (indirectly) by velocity perturbations in the shear layer – which is what the transfer function  $\Psi(s) = G(s)S(s)A(s)$  represents – to be small at high frequencies. Similarly, we expect the response of the shear layer to incoming acoustic waves to decrease with increasing frequency, and this response is characterized by the transfer function  $R(s)$ .

A transfer function with a relative degree of zero, on the other hand, has finite response at high frequencies. Since viscosity is unimportant in sound waves (Dowling & Ffowcs Williams, 1983), assumption (ii) is reasonable and, like assumption (i), is

---

<sup>1</sup>For clarity's sake we now drop the  $(s)$  notation, and the frequency-dependence is implied.

physically motivated.<sup>1</sup> Using these two assumptions gives

$$\begin{aligned}\deg(D_\Psi D_R - N_\Psi N_R) &= \deg(D_\Psi D_R), \text{ and} \\ \deg(D_\Psi N_B + N_\Psi D_B) &= \deg(D_\Psi N_B),\end{aligned}$$

and equation (5.20) becomes

$$n^*(\hat{P}_1) = \deg(D_\Psi D_R) + \deg(D_B) - \deg(D_\Psi N_B) - \deg(D_R) \quad (5.21)$$

$$= \deg(D_\Psi D_R D_B) - \deg(D_\Psi D_R N_B) \quad (5.22)$$

$$= \deg\left(\frac{D_B}{N_B}\right) = \deg\left(\frac{1}{B(s)}\right), \quad (5.23)$$

which by assumption is zero.

## 5.6 SUITABILITY OF THE ADAPTIVE CONTROLLER FOR CAVITY OSCILLATIONS

We now consider applying the adaptive controller of chapter 3 to the cavity flow. We first summarize the conditions placed on the open-loop plant by the adaptive controller of chapter 3, and look at to what extent each is met by the model of the cavity that was developed in § 5.5. The concept of collocated control is then introduced as a way of dealing with the right-half plane zeros that can occur for the cavity flow, and it is shown that using this collocated control arrangement, the cavity flow meets all of the requirements of the adaptive controller.

The open-loop transfer function of interest includes the actuator,  $P_L(s) = L(s)P(s)$ . The requirements placed on  $P_L(s)$  by the adaptive controller, and the extent to which  $P_L(s)$  meets them, are summarized below.

- (i)  $P_L(s)$  has no right half-plane zeros. Based on the linear model derived in 5.5.1,  $P(s)$  – and therefore  $P_L(s)$  – may have zeros in the right half-plane, particularly at low frequencies.
- (ii) the sign of the high-frequency gain of  $P_L(s)$  is known. At high frequencies  $P(s)$

<sup>1</sup>Indeed, the form chosen for  $B(s)$  in (5.7) is ‘all-pass’ and has a relative degree of zero after a Padé approximant is used for the time delay.

becomes simply  $P(s) = B(s) = k_b e^{-s\tau_b}$ , and so the high-frequency gain of  $P_L(s)$  is  $k_l k_b$ , where  $k_l$  is the high-frequency gain of the actuator transfer function. (This assumes that the body force completely characterizes the high-frequency behaviour of the system, which it may not, and so in general we must assume that the high-frequency gain must be determined.)

- (iii) *the relative degree of  $P_L(s)$  does not exceed two.* In § 5.5.2 it was shown that the relative degree of  $P(s)$  is zero. Therefore the relative degree of  $P_L(s)$  is given by the relative degree of the actuator transfer function  $L(s)$ . We expect a typical actuator to have a relative degree of one or two – see Kegerise *et al.* (2007a), for example, where the actuator used is typical of a second-order, under-damped system. Therefore we assume that the relative degree of  $P_L(s)$  satisfies  $n^* \leq 2$ .

Clearly, all of the requirements on  $P_L(s)$  are met, with the exception of the locations of its zeros. There is also another, slightly more subtle way in which the cavity flow does not presently meet the above requirements. For a transfer function to be *Strictly Positive Real*, a relative degree of one is necessary but not sufficient. In addition the pole and zero pairs must ‘interlace’ in frequency: that is, a pair of poles must be followed by a pair of zeros, who must be followed by another pair of poles, and so on. Referring to figure 5.3, this condition is not met at any of the three pressure probes, where in each case the three Rossiter tones neighbour each other with no zeros in between.

We remedy both of these problems by introducing *collocated control*. This arrangement is depicted in figure 5.13, where now the pressure sensor and body force region are collocated. The location of the body force does not change, the pressure sensor used for control instead moving to join it near the cavity’s upstream corner. Although this arrangement is not possible in practice, it could be approximated in experiments by placing a pressure sensor close to the actuator at the upstream corner. It seems reasonable to assume that such an experimental arrangement, although no longer strictly collocated, could give rise to the same desired properties of only left half-plane zeros and interlacing poles and zeros.

We introduce this collocation to take advantage of the fact that, for a collocated transfer function from volume velocity to pressure, the product of the input and out-

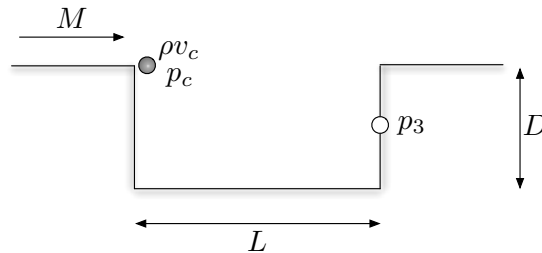


FIGURE 5.13: Collocated control arrangement for adaptive control. (Pressure probe 3 is also shown.)

put has the dimension of power, and is therefore positive real (see Hong & Bernstein (1998)). Only stable transfer functions can be positive real, and so this positive realness applies to the closed-loop stabilized system (as it did in the development of the adaptive controller in § 3.3.1).

For a transfer function to be positive real, all of its zeros must lie in the left half-plane, and its poles and zeros must interlace in frequency (this ensures that its phase lies between  $-90^\circ$  and  $+90^\circ$ ). Therefore using collocated control, the closed-loop stabilized system must have only left half-plane zeros, and the pole and zero pairs must interlace in frequency. These collocation-based arguments do not include the actuator transfer function  $L(s)$ , but we have already established in requirement (iii) on page 86 that the overall system  $P_L(s)$  can be modeled as having a relative degree not exceeding two, and now all of the requirements on  $P_L(s)$  are satisfied.

## 5.7 CONCLUDING REMARKS

This chapter has focused on linear models of cavity oscillations that are useful for feedback control purposes. By applying system identification techniques to direct numerical simulations of the cavity flow, its linear dynamics have been very accurately determined. The transfer function found has been compared to that given by a simple linear model, which shows reasonable agreement and which is useful for feedback control design.

By including a simple model of the acoustic field generated *directly* by the body force region, two properties of the system are more accurately modeled: its behaviour

at high-frequencies (in particular its time delay); and the locations of its zeros.<sup>1</sup>

Some general properties of cavity oscillations have been derived. These properties are of general interest for any feedback control scheme, but are particularly useful for adaptive control. Although the derivation of these properties relies to some extent on the specific linear model used, many of the underlying assumptions would hold for any physically-motivated model – for example, that the shear layer amplifies disturbances only over some limited frequency range, and that the actuator is of low relative degree. Finally, by comparing these derived properties to the properties required by the adaptive controller of chapter 3, it has been shown that such an adaptive controller can be applied to the cavity flow, provided that collocated control is used.

#### ACKNOWLEDGEMENT

The work presented in this chapter and to be presented in chapter 6 was done in collaboration with Professor Clarence Rowley at Princeton University. As part of the collaborative work I spent two months on a research visit to Professor Rowley's research group, where we had many discussions on the DNS code and on applying feedback control to it.

---

<sup>1</sup>In fact, the linear model which does not account for the body force's acoustic field predicts only the poles of the system and not its zeros, as demonstrated in equation (5.11).

## CHAPTER 6

### FEEDBACK CONTROL OF CAVITY OSCILLATIONS

Previous attempts at controlling cavity oscillations have met with limited success. One of the major challenges for the control of cavity flows is dealing with the sensitivity of the flow's dynamics to changes in Mach number. See, for example, Rowley & Juttijudata (2005), where an 8 % change in Mach number from  $M = 0.60$  to  $M = 0.55$  resulted in the closed-loop controller actually increasing the amplitude of oscillations, or Kegerise *et al.* (2007b), where closed-loop control maintained suppression of cavity tones only over a modest range of Mach numbers ( $0.275 \leq M \leq 0.29$ ).

Feedback control is most effective when a reliable model of the system-to-be-controlled is available. In this chapter, system identification and model reduction techniques are used to form a low order model of the cavity flow. Specifically, the Eigen-system Realization Algorithm (ERA) is used to find a low order state-space model of the cavity flow. An optimal ( $\mathcal{H}_2$ ) controller is then designed, and this controller maintains stability over a wider Mach number range than seen in previous studies. We then attempt to improve the robustness of the controller by introducing a very simple type of gain scheduling.

Finally, we look at using a Lyapunov-based adaptive control scheme like that used in § 3, and see that it maintains stability over an even wider Mach number range.

#### 6.1 REDUCED ORDER MODELING FOR FLUIDS

One of the greatest challenges for feedback control of fluids is their dynamical complexity, the Navier-Stokes equations being both high-dimensional and non-linear. Model

reduction involves finding low-dimensional models that approximate the high-dimensional dynamics of a system. Since model reduction is so pertinent to the problem of feedback control of fluids, a brief review of some of the methods available is given here, before we use one of these methods – the Eigensystem Realization Algorithm (ERA) – to form a reduced-order model of the cavity flow which is useful for feedback control purposes.

Proper Orthogonal Decomposition (POD), also known as principal component analysis, or the Karhunen-Loève expansion, has been used for some time in developing low-order models of fluids (Lumley, 1970; Sirovich, 1987). Given a set of data that lie in a vector space  $\mathcal{V}$ , proper orthogonal decomposition finds a subspace  $\mathcal{V}_r$  of dimension  $r$  such that the error in the projection onto the subspace is minimized. The resulting POD modes are optimal in that they maximize the average energy in the projection of the data onto the subspace spanned by the modes. However, these POD modes may not be the best modes for describing the *dynamics* that generate the data set, since low-energy features may be critically important to the dynamics. For cavity oscillations, for example, acoustic disturbances are crucial to the Rossiter mechanism, even though they have much smaller energy than hydrodynamic pressure fluctuations.

To address this problem, Rowley (2005) introduced a method called *balanced* POD which approximates *balanced truncation* (Moore, 1981) for large systems, and which has deep connections with POD. The balancing refers to the observability and controllability Gramians of the resulting low order model being equal and diagonal (or ‘balanced’), and physically this means that the dynamics that generate the data set are properly accounted for. The concepts of observability and controllability of a low order model will be explained in more detail in the next section.

Because of this balancing procedure, a reduced order model computed by balanced POD is vastly superior to that given by POD for a given order  $r$ , at least when we are concerned with finding a low order model for feedback control purposes. The main disadvantage with balanced POD, however, is that solutions of an adjoint system are required, and so the method can only be used in computational studies and not for experimental data.

Ma *et al.* (2009) have shown that the reduced order models generated by the eigen-

system realization algorithm (Juang & Pappa, 1985) – a method developed for modal parameter identification and model reduction in the structural dynamics community – are theoretically identical to those generated by balanced POD. A distinct advantage of the ERA is that solutions of an adjoint system are not required, and so a balanced low order model can be found from experimental data as well as from simulations.

## 6.2 BALANCED REDUCED ORDER MODELING

We now look at some of the important concepts for balanced reduced order modeling, before looking specifically at the eigensystem realization algorithm.

Consider the linear, time-invariant, discrete-time dynamical system

$$\begin{aligned}x(k+1) &= Ax(k) + Bu(k) \\ y(k) &= Cx(k)\end{aligned}\tag{6.1}$$

where  $u \in \mathbb{R}^p$  is a vector of inputs,  $y \in \mathbb{R}^q$  is a vector of outputs and  $x \in \mathbb{R}^n$  is called the system state:  $n$  is the order of the system, and will be important later.  $k$  is the time step index. We consider the discrete-time case, since we are interested in discrete-time data from simulations or experiments.

We now look at the definitions of two important concepts for balanced reduced order models: controllability and observability.

### 6.2.1 CONTROLLABILITY

For zero initial condition  $x(0) = 0$ , the state of the system (6.1) evolves according to

$$\begin{aligned}x(1) &= Bu(0) \\ x(2) &= ABu(0) + Bu(1) \\ x(3) &= A^2Bu(0) + ABu(1) + Bu(2) \\ &\vdots \\ x(s) &= \sum_{k=1}^s A^{s-k} Bu(k)\end{aligned}$$

or, in matrix form

$$x(s) = \begin{bmatrix} B & AB & A^2B & \cdots & A^{s-1}B \end{bmatrix} \begin{bmatrix} u(s-1) \\ u(s-2) \\ u(s-3) \\ \vdots \\ u(0) \end{bmatrix}, \quad (6.2)$$

which relates the state at time step  $s$ ,  $x(s)$  to previous inputs  $u(k)$ ,  $0 \leq k \leq s-1$ . A system is called *controllable* if, for every state  $\bar{x}$ , there exists an input series  $u(k)$  that takes the state from  $x(0) = 0$  to  $x(s) = \bar{x}$  in a finite time. It can be shown that the system (6.1) is controllable if and only if the controllability matrix

$$\mathcal{Q} \triangleq \begin{bmatrix} B & AB & A^2B & \cdots & A^{s-1}B \end{bmatrix}, \quad (6.3)$$

$\mathcal{Q} \in \mathbb{R}^{n \times ps}$ , which appears in (6.2), has rank  $n$ . Of course, if the (linear) system can go from zero state to any  $\bar{x}$ , then it can go from any  $x(0)$  to any  $\bar{x}$ .

### 6.2.2 OBSERVABILITY

A state-space realization (6.1) is observable if the initial state  $x(0)$  can be deduced from knowledge of  $u(k)$  and  $y(k)$  for  $0 \leq k \leq s$  for any  $s > 0$ .

Without loss of generality, we may take  $u(k) = 0$ ,  $\forall k$ , since the  $u$ -dependent part of the solution can always be subtracted from the full solution. Therefore looking at the evolution of the output  $y(k)$ , for some initial state  $x(0) \neq 0$ , the system (6.1) with  $u(k) = 0$  gives

$$\begin{aligned} y(0) &= Cx(0) \\ y(1) &= CAx(0) \\ y(2) &= CA^2x(0) \\ &\vdots \\ y(s-1) &= CA^{s-1}x(0) \end{aligned}$$

or, in matrix form

$$\begin{bmatrix} y(0) \\ y(1) \\ y(2) \\ \vdots \\ y(s-1) \end{bmatrix} = \begin{bmatrix} C \\ CA \\ CA^2 \\ \vdots \\ CA^{s-1} \end{bmatrix} x(0)$$

which relates the output at all times to the initial state  $x(0)$ . A unique solution exists – and therefore the initial state  $x(0)$  can be deduced – if and only if the observability matrix

$$\mathcal{P} = \begin{bmatrix} C & CA & CA^2 & \cdots & CA^{s-1} \end{bmatrix}^T, \quad (6.4)$$

$\mathcal{P} \in \mathbb{R}^{qs \times n}$ , has rank  $n$ . Having justified our setting  $u(k) = 0$  without loss of generality, this result holds for any  $u(k) \neq 0$ .

### 6.2.3 EIGENSYSTEM REALIZATION ALGORITHM

In the previous section it was stated that the eigensystem realization algorithm can be used to find *balanced* reduced order models. We now look at using the ERA to find a low order state-space model of the cavity flow. The ERA is valid only for stable systems, and therefore we use the dynamic phasor – as we did in § 5 – to first stabilize the flow. Then we use an extension to the ERA called observer/controller identification (OCID), which allows the open-loop dynamics of a system operating in closed-loop to be found.

An overview of the ERA is now given, and the ERA for stable systems is described. Then we look briefly at the problems faced in applying it to an unstable system, and see how these problems can be addressed using OCID.

The eigensystem realization algorithm involves forming the generalized  $\alpha q \times \beta p$

Hankel matrix composed of the system Markov parameters:

$$H(k-1) = \begin{bmatrix} Y_k & Y_{k+1} & \cdots & Y_{k+\beta-1} \\ Y_{k+1} & Y_{k+2} & \cdots & Y_{k+\beta} \\ \vdots & \vdots & \ddots & \vdots \\ Y_{k+\alpha-1} & Y_{k+\alpha} & \cdots & Y_{k+\alpha+\beta-2} \end{bmatrix} \quad (6.5)$$

where  $\alpha$  and  $\beta$  are arbitrary integers. The Markov parameter  $Y_k \in \mathbb{R}^{q \times p}$  for time index  $k$  is defined as

$$Y_k \triangleq CA^{k-1}B. \quad (6.6)$$

Setting  $k = 1$  for the Hankel matrix, substituting in (6.6) for the Markov parameters, and decomposing into two matrices, we find that

$$H(0) = \mathcal{P}_\alpha \mathcal{Q}_\beta \quad (6.7)$$

where  $\mathcal{P}_\alpha \in \mathbb{R}^{\alpha q \times n}$  is the observability matrix (6.4) and  $\mathcal{Q}_\beta \in \mathbb{R}^{n \times \beta p}$  is the controllability matrix (6.3) as defined earlier. Since the Hankel matrix  $H(0)$  is composed of the Markov parameters in (6.5), we see from (6.7) that the Markov parameters are closely related to the observability and controllability matrices.

Now, factorizing the Hankel matrix  $H(0)$ , which has rank  $n$ , using the singular value decomposition, and truncating to order  $r < n$ , we have

$$H(0) = R\Sigma S^T \cong R_r \Sigma_r S_r^T. \quad (6.8)$$

$R_r$  and  $S_r$  are made up of the first  $r$  (orthonormal) columns of  $R$  and  $S$  respectively.  $\Sigma_r$  is a rectangular matrix,  $\Sigma_r = \text{diag} = [\sigma_1 \ \sigma_2 \ \cdots \ \sigma_r]$ , with  $\sigma_1 \geq \sigma_2 \geq \cdots \geq \sigma_r \geq 0$ , the first  $r$  singular values of  $H(0)$ . Examining (6.7) and (6.8) as a whole, we can write

$$H(0) = \mathcal{P}_\alpha \mathcal{Q}_\beta \cong (R_r \Sigma_r^{1/2})(\Sigma_r^{1/2} S_r^T). \quad (6.9)$$

One possible choice for the decomposition of  $H(0)$  is then  $\mathcal{P}_\alpha = R_r \Sigma_r^{1/2}$  and  $\mathcal{Q}_\beta =$

$\Sigma_r^{1/2} S_r^T$ , and this choice makes both  $\mathcal{P}_\alpha$  and  $\mathcal{Q}_\beta$  balanced in the sense that

$$\begin{aligned}\mathcal{P}_\alpha^T \mathcal{P}_\alpha &= \Sigma_r^{1/2} R_r^T R_r \Sigma_r^{1/2} = \Sigma_r \\ \mathcal{Q}_\beta \mathcal{Q}_\beta^T &= \Sigma_r^{1/2} S_r^T S_r \Sigma_r^{1/2} = \Sigma_r,\end{aligned}\tag{6.10}$$

where  $\mathcal{P}_\alpha^T \mathcal{P}_\alpha$  and  $\mathcal{Q}_\beta \mathcal{Q}_\beta^T$  are the observability and controllability Gramians.

The system matrices  $B$  and  $C$  can then be found from (6.3) and (6.4) respectively. To find the  $A$  matrix, let  $k = 2$  in (6.5) and use (6.9) to give

$$H(1) = \mathcal{P}_\alpha A \mathcal{Q}_\beta \cong (R_r \Sigma_r^{1/2}) A (\Sigma_r^{1/2} S_r^T),$$

from which  $A$  can be found. For a more rigorous treatment of the ERA, see Juang & Pappa (1985) or Juang (1994).

The state-space model (6.1) given by the ERA is *balanced*: the controllability and observability Gramians are diagonal and equal by (6.10), and this means that the *dynamics* of the system are properly taken into account. Furthermore, an upper bound for the error in the reduced order model can be derived. Let  $G_r$  denote the transfer function of the reduced order model of order  $r$ , and let  $G$  denote the transfer function of the full system. Then the  $\mathcal{H}_\infty$ -norm of the error satisfies

$$\|G - G_r\|_\infty \leq 2 \sum_{j=r+1}^n \sigma_j$$

(‘twice the sum of the tails’).

Finally, we briefly note a connection to POD here: the modes found by POD are the most controllable modes, and the observability of the modes is not taken into consideration. This helps to explain some of the inadequacies of POD for feedback control, since the most controllable modes may be only weakly observable.

### *Observer/controller identification (OCID)*

The ERA is only applicable to stable systems. We can see the problem with applying the ERA to an unstable system by again considering equation (6.6):<sup>1</sup>

$$Y_k \triangleq CA^{k-1}B.$$

For a stable system subjected to an impulse, the term  $A^{k-1}$  becomes progressively smaller, and the Markov parameter (or ‘impulse response’)  $Y_k \simeq 0$  for sufficiently large  $k$ . For an unstable system, however,  $A^{k-1}$  becomes progressively larger, and no such approximation can be made.<sup>2</sup>

For an unstable system made stable by feedback, OCID remedies this problem by first computing the Markov parameters of the closed-loop, stable system. Using these Markov parameters, and the fact that both the forcing signal and the feedback signal can be measured ( $\rho_{v_w}$  and  $\rho_{v_f}$  in figure 5.2(b)), OCID then finds the Markov parameters of the open-loop, unstable system and of the controller. These Markov parameters can be used to find a state-space realization of the open-loop system (and, if desired the closed-loop controller).

For more details of OCID, see Juang (1994), chap. 8.

### 6.3 APPLICATION OF THE ERA TO THE CAVITY FLOW

We now look at applying the ERA to the cavity flow. To validate the reduced order models obtained, we compare the frequency response of the reduced order model to that found using spectral analysis in § 5.<sup>3</sup>

We find that by using a model with 140 states, the frequency responses of the reduced order model and the spectral estimate are almost indistinguishable: the comparison is shown in figure 6.1. We seek a low order model of the cavity flow, and so the question now arises: How many states are required for feedback control purposes?

<sup>1</sup>This is without considering the non-linearities that the growing response will give rise to.

<sup>2</sup>A similar problem can occur for lightly damped systems, where the  $k$  required to satisfy  $Y_k \simeq 0$  can become prohibitively large.

<sup>3</sup>The reduced order model is in state-space form (6.1) and is therefore in the (discrete) time domain. Its frequency response can be found by using  $z$ -transforms.

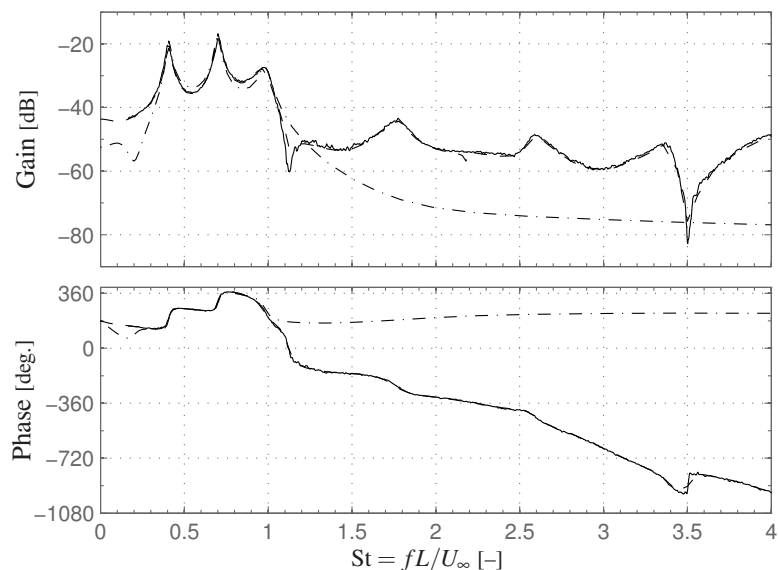


FIGURE 6.1: Open-loop Bode diagram comparison: transfer function found using spectral analysis (—), and using the ERA with 140 states (---) and with 8 states (-.-). All for probe 3.

By using just 8 states in the ERA-derived reduced order model, one observes (figure 6.1) that the first three Rossiter modes are very well-captured. (Mathematically, this means that the  $\mathcal{H}_\infty$ -norm of the error  $\|G - G_r\|_\infty$  is sufficiently small using 8 states.)

This 8-state reduced order model is used in the next section for the design of a linear quadratic Gaussian regulator.

## 6.4 LQG CONTROL

The measured open-loop transfer function, as well as giving valuable insight into some of the physical features of the cavity flow, can be used for feedback control design purposes. Using the state-space model found using the ERA, it is possible to use standard robust control techniques such as Linear Quadratic Gaussian (LQG) control and  $\mathcal{H}_\infty$  control (Zhou & Doyle, 1998). Here we focus on LQG control, and use it to find a stabilizing regulator for the cavity flow at a Mach number of 0.6.

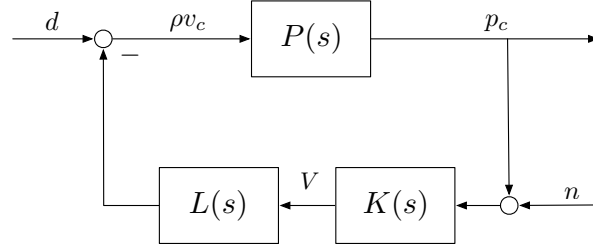


FIGURE 6.2: Closed-loop cavity arrangement. The effect of noise ( $n$ ) and disturbances ( $d$ ) has been included. The subscript  $c$  is used to denote the control parameters  $\rho v_c$  and  $p_c$ , which could be situated anywhere in the cavity's domain, and  $V$  is the control voltage.

#### 6.4.1 CONTROLLER DESIGN

The cavity flow's transfer function  $P(s)$  found in § 5 and § 6.3 is from the control body force  $\rho v_c$  to the pressure measurement  $p_c$ . In an experiment, an actuator would be used to provide the body force, and so we include an actuator transfer function here, which we denote  $L(s)$ . Then the regulator is designed for the overall plant  $P_L(s) = L(s)P(s)$ , which is the transfer function between a control voltage  $V$  and the pressure measurement  $p_c$ . The overall arrangement is shown in figure 6.2.

For the discrete-time state space model defined by (6.1), a Linear Quadratic (LQ) regulator uses the state feedback law

$$u = -Kx \quad (6.11)$$

to minimize the quadratic cost function

$$J = \sum_{i=0}^{\infty} (x^T Q_x x + u^T Q_u u). \quad (6.12)$$

$Q_x \in \mathbb{R}^{n \times n}$  and  $Q_u \in \mathbb{R}^{p \times p}$  are weighting matrices used to penalize large system states and large control inputs respectively.<sup>1</sup>

<sup>1</sup>Note the difference between the scalar transfer function  $K(s)$  in figure 6.2 and the matrix of (constant) control gains  $K$  in the state feedback law (6.11).

Substituting (6.11) into (6.1), we obtain the closed-loop system

$$\begin{aligned}x(k+1) &= (A - BK)x(k) \\ y(k) &= Cx(k)\end{aligned}\tag{6.13}$$

and we see that, by suitable choice of the feedback gain matrix  $K$ , the eigenvalues of  $(A - BK)$  – and therefore the dynamics of the closed-loop system – can be made stable.

*Linear Quadratic* (LQ) control assumes that the full state  $x$  is available to the regulator – this state is used in the feedback law (6.11). In many cases, though, the full state is not available for measurement, the regulator having *direct* access only to the inputs  $u$  and the outputs  $y$ . *Linear Quadratic Gaussian* (LQG) control can be employed to remedy this by using an observer to form an estimate  $\hat{x}$  of the real state  $x$ . This estimate of the state is used in the LQG control feedback law

$$u = -K\hat{x}.\tag{6.14}$$

It remains to see how the estimate of the state is formed: the observer determines the estimate of the state by

$$\begin{aligned}\hat{x}(k+1) &= A\hat{x}(k) + Bu(k) + L[y(k) - \hat{y}(k)] \\ \hat{y}(k) &= C\hat{x}(k),\end{aligned}\tag{6.15}$$

a system that mimics (6.1), but is forced by the output error  $y - \hat{y}$ . It is straightforward to show that, if the eigenvalues of  $(A - LC)$  are stable, the estimation error  $\hat{x} - x$  tends to zero. The *Gaussian* term in Linear Quadratic Gaussian control refers to the specific type of observer used, a Kalman filter. A Kalman filter amounts to a specific choice of the observer gain matrix  $L$  which is optimal, in the sense that the error converges in the presence of stochastic disturbances  $d$  and noise  $n$  (see figure 6.2), assumed to be zero-mean, *Gaussian*, white-noise processes.

The LQG and optimal estimation problems can be solved using standard routines in Matlab. The resulting LQG controller and observer can then be combined to give an overall regulator  $K(s)$ , which is of the same order as the plant model used  $P_L(s)$  (including actuator).

The actuator transfer function used  $L(s)$  is a second-order, under-damped system:

$$L(s) = k_L \frac{\omega_L^2}{s^2 + 2\zeta_L \omega_L s + \omega_L^2},$$

with  $k_L = 1.0$ ,  $\omega_L = 1.9$  (which corresponds to a non-dimensional frequency of  $f_L = 0.3$ ) and  $\zeta_L = 0.3$ . See Kegerise *et al.* (2007a) for example, where the frequency response of the piezoelectric actuator used was typical of this type.

Since we have a single input system,  $Q_u$  in (6.12) is simply a scalar. We choose the output measurement  $y = Cx$  as our output cost (giving  $Q_x = C^T C$ ), and the quadratic cost function has a simple form

$$J = \sum_{i=0}^{\infty} (y^2 + q_u u^2),$$

where the scalar  $q_u$  is used to specify the relative importance of maintaining a small input signal and maintaining a small output measurement. Very little noise is encountered in the direct numerical simulations, but we expect more in a real experiment, so Gaussian white noise is artificially added to the pressure measurement. The covariance of this noise is used in the design of the observer.

The Bode diagram of the overall regulator  $K(s)$ , given by the combination of the state estimator (6.15) and the feedback law (6.14), is shown in figure 6.3. The Nyquist diagram of the overall open-loop plant  $P_L(s)$  is plotted in figure 6.4(a): this shows the (complex-valued) frequency response of the system in the complex plain for both positive and negative frequencies. In figure 6.4(b), the Nyquist diagram of the loop-gain  $K(s)P_L(s)$  is plotted. Since the open-loop system has two pairs of unstable poles, we require 4 counter-clockwise encirclements of the -1 point. The regulator  $K(s)$  provides those 4 encirclements, and it does so with a gain margin of 4.5 dB and a phase margin of  $36^\circ$ .

#### 6.4.2 RESULTS

We now look at how the LQG regulator performs in direct numerical simulations of the cavity flow. The LQG regulator is first applied at the design point: a free stream

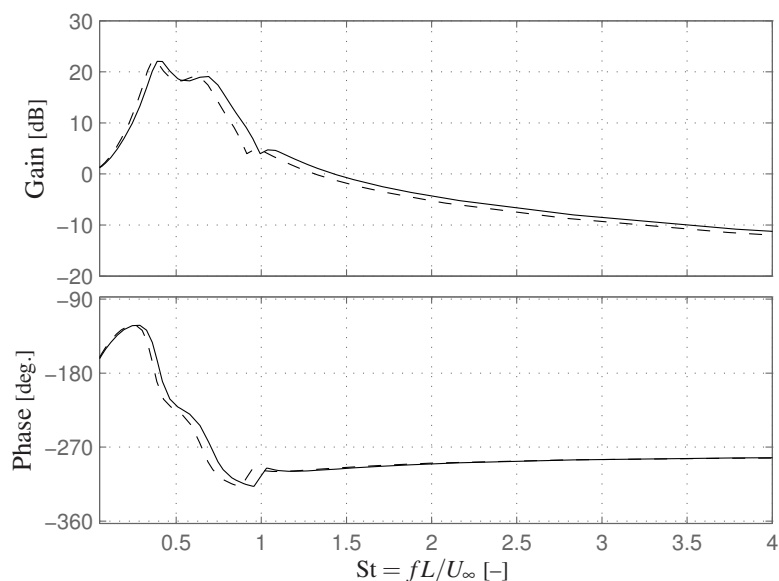


FIGURE 6.3: Bode diagram of the LQG regulator (—); and of the gain-scheduled regulator for a Mach number of  $M = 0.8$  (---).

Mach number of  $M = 0.6$ . Since we are confident that the state-space model of the system is accurate, and since the optimal control techniques used should provide reasonable robustness to changes in the plant, the regulator should exhibit good robustness to changes in Mach number. We test this by applying the controller at off-design conditions, for Mach numbers in the range  $0.4 \leq M \leq 0.8$ .

Closed-loop control results for the design case of  $M = 0.6$  are shown in figure 6.5: control is activated at approximately 76 non-dimensional time units. The introduction of the LQG regulator stabilizes the flow, and the pressure measurement is reduced to the background noise level.

Figure 6.6 summarizes the results of the LQG regulator applied at off-design Mach numbers. Results for Mach numbers of 0.4, 0.5, 0.7 and 0.8 are shown – this range of Mach numbers is based on the range over which the Rossiter mechanism (or ‘shear layer mode’) is observed (Rowley *et al.*, 2002). The LQG regulator performs well at the lower Mach numbers, providing closed-loop stability for  $M = 0.4$  and  $M = 0.5$ . At the higher Mach numbers, though, it performs less well: for  $M = 0.7$  and for  $M = 0.8$ , the limit cycle, although reduced in amplitude by the regulator, persists. This poorer performance at higher Mach numbers is a result of the cavity’s modified dynamics, and

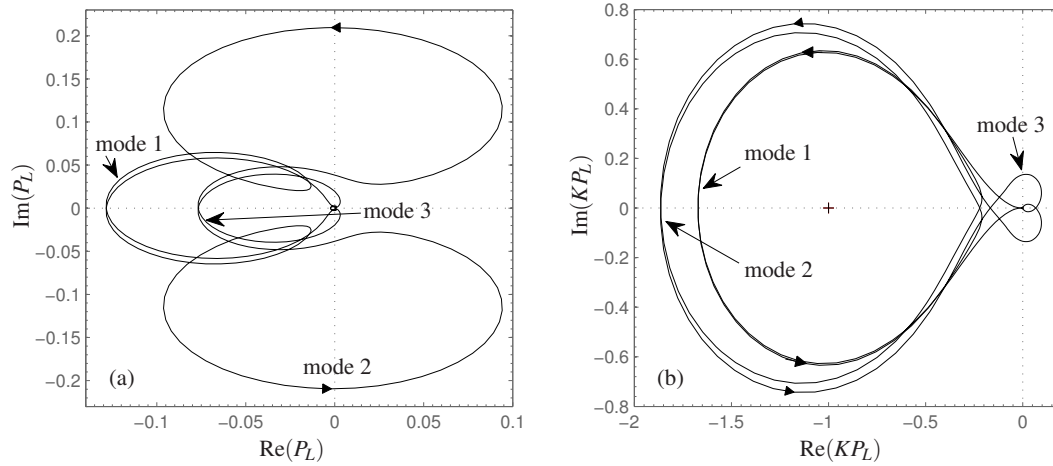


FIGURE 6.4: Nyquist diagrams for LQG control: (a) the open-loop plant  $P_L(s)$ ; and (b) the loop-gain  $K(s)P_L(s)$ . Positive and negative frequencies are shown, and in each plot the three Rossiter modes are indicated.

is not a result of the 8 state reduced order model used: the same limitations would be encountered by the controller if a higher order model of the cavity were used.

These same observations can be made by looking at the time delay phase portraits of the pressure signals, which can help to distinguish between a stable, noise-driven regime and a limit-cycling regime. The phase portrait of a limit-cycling system will be a closed curve (and, with noise, a fuzzy curve). The phase portrait of a stable system, forced by noise, will be concentrated about a point. Figure 6.7 shows the time delay phase portraits for each of the four off-design Mach numbers: both open-loop and closed-loop data are shown. Each of the plots helps clarify the observations made based on figure 6.6. For Mach numbers of 0.4 and 0.5, control transforms the pressure phase portrait from a closed-curve to being concentrated about a point, suggesting closed-loop stability. For Mach numbers of 0.7 and 0.8, the closed-curve nature of the phase portrait remains intact with feedback control activated.

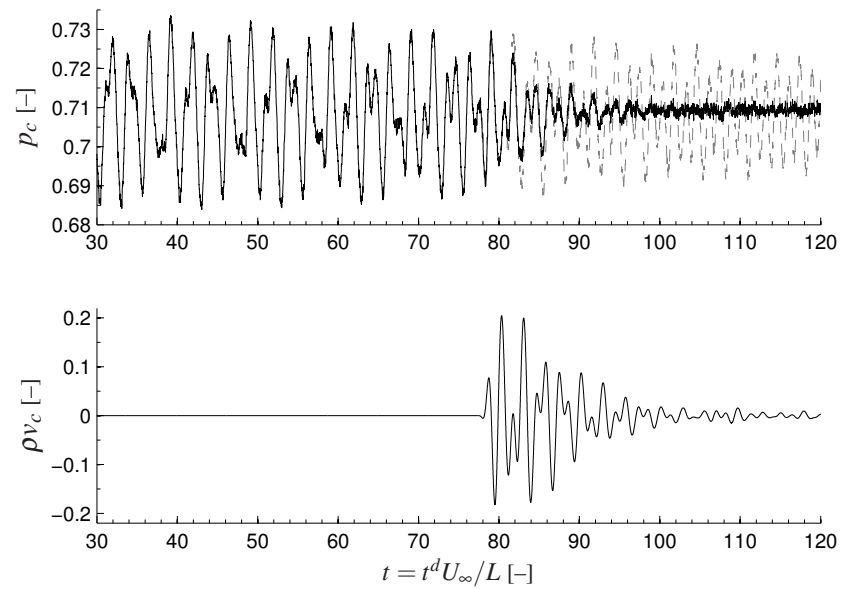


FIGURE 6.5: Closed-loop control using the LQG regulator at the design Mach number of  $M = 0.60$ . The pressure measurement (top) and the control body force (bottom) are shown. For the pressure measurement, the closed-loop case (—) is compared to the open-loop case (---).

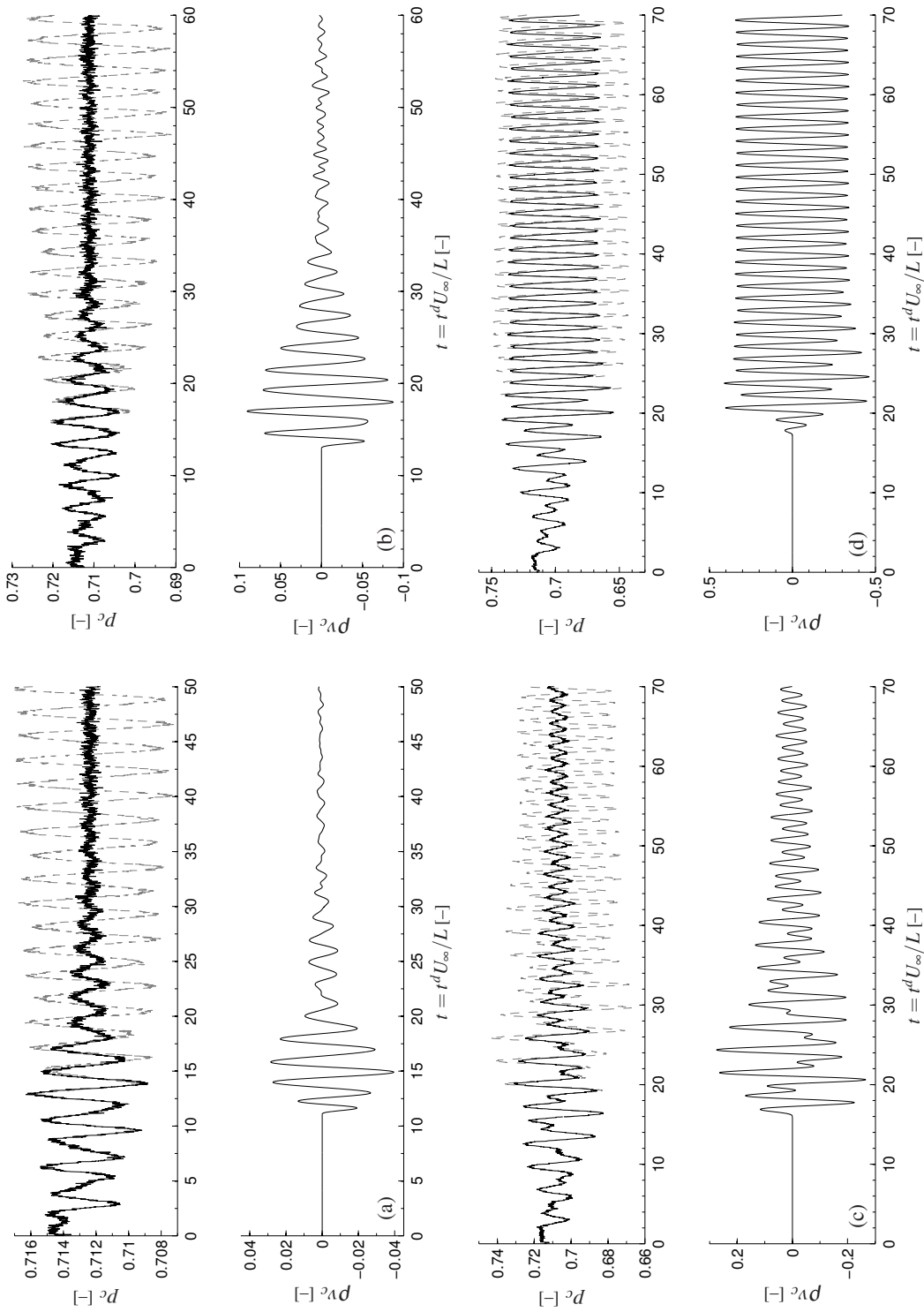


FIGURE 6.6: Performance of the LQG regulator at off-design Mach numbers: for a free stream Mach number of (a)  $M = 0.4$ ; (b)  $M = 0.5$ ; (c)  $M = 0.7$ ; and (d)  $M = 0.8$ . Legend same as figure 6.5.

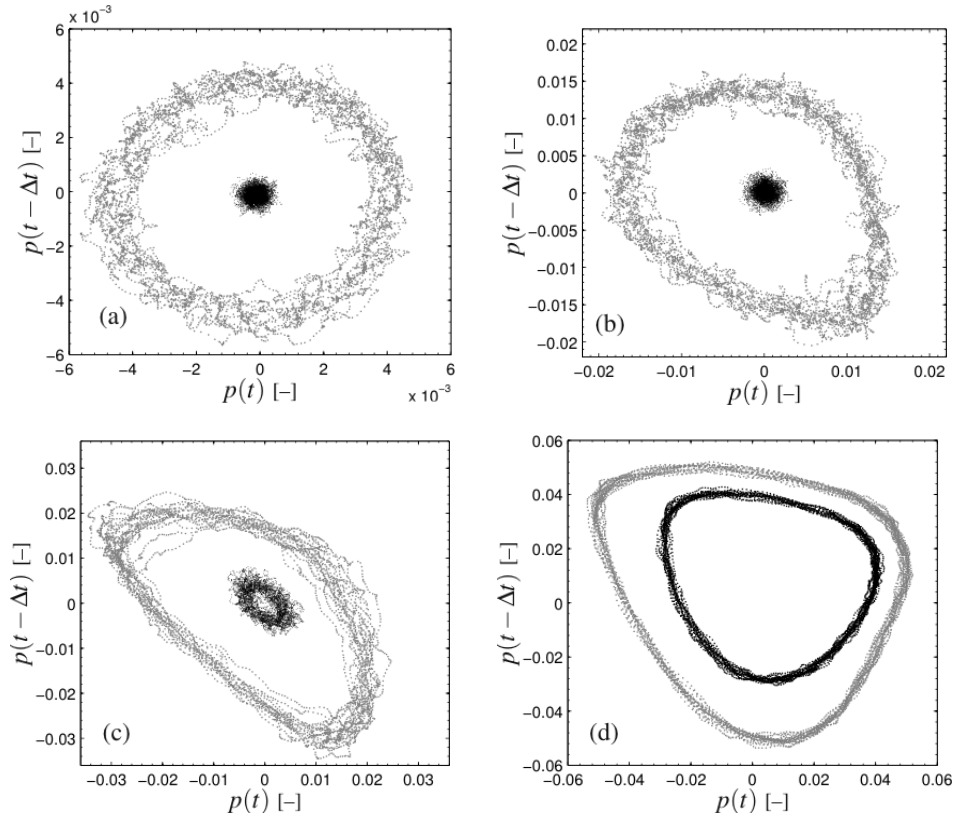


FIGURE 6.7: Time delay phase portraits of the LQG regulator for free stream Mach numbers of (a)  $M = 0.4$ ; (b)  $M = 0.5$ ; (c)  $M = 0.7$ ; and (d)  $M = 0.8$ . Pressure measurements are compared for the closed-loop ( $\bullet$ ) and the open-loop case ( $\circ$ ).

### 6.4.3 GAIN SCHEDULING

In this section we ask a simple question: can Rossiter's formula, used for predicting the frequencies of cavity oscillations, be used to increase the robustness of a feedback controller?

Rossiter's formula (Rossiter, 1964) has proved to be a reliable way of predicting the frequencies of cavity oscillations. Whilst modifications have since been made (Heller *et al.*, 1971), these modifications retain the same underlying mechanism: a disturbance in the free shear layer spanning the cavity is amplified via Kelvin-Helmholtz instability; acoustic scattering of the disturbance at the cavity trailing edge gives rise to further disturbances to the shear layer; for suitable phase change of the disturbance, resonance

occurs. Rossiter's formula predicts resonant modes at Strouhal numbers given by

$$\text{St}_n = \frac{n - \gamma}{M + 1/\kappa}, \quad n = 1, 2, \dots$$

where  $\gamma$  is a constant phase delay, and  $\kappa$  is given by the phase speed of disturbances in the shear layer.

Gain-scheduling is a technique commonly employed in feedback control systems to increase robustness to changing operating conditions. The method involves scheduling the parameters of the feedback controller based on some global system property that can be measured. In our case, this amounts to modifying the LQG regulator in response to the free stream Mach number.

The exact form of the scheduling that we consider is very crude: simply 'stretching' or 'shrinking' the regulator's frequency response along the frequency axis: the stretching factor used is given by Rossiter's formula. Using Rossiter's formula, it is easy to show that, for a given resonant mode number  $n$ , the relationship between the Strouhal number of that resonant mode at two different Mach numbers  $M_1$  and  $M_2$  is given by

$$\frac{\text{St}_{n,M_2}}{\text{St}_{n,M_1}} = \frac{M_1 + 1/\kappa}{M_2 + 1/\kappa}, \quad (6.16)$$

which gives us the stretching factor to use in the gain scheduling: this expression holds for any  $n$ . The result of (6.16) for a Mach number of  $M = 0.8$ , which gives a stretching factor of 0.922, is shown in figure 6.3. The regulator's frequency response is squeezed along the frequency axis to anticipate the reduction in Strouhal number that this new Mach number brings.

We now look at applying this gain-scheduling to the regulator at those Mach numbers where closed-loop stability was not achieved ( $M = 0.7$ ,  $M = 0.8$  – see figure 6.6). The results are shown in figure 6.8. For clarity, the open-loop pressure data are omitted, and only the original regulator and gain-scheduled regulator data are compared. The same scale as that in figure 6.6 is used for the pressure data, however, so comparison with the open-loop data can easily be made.

We see that the gain-scheduled regulator actually performs more poorly at both Mach numbers, with the amplitude of oscillations increased relative to the original

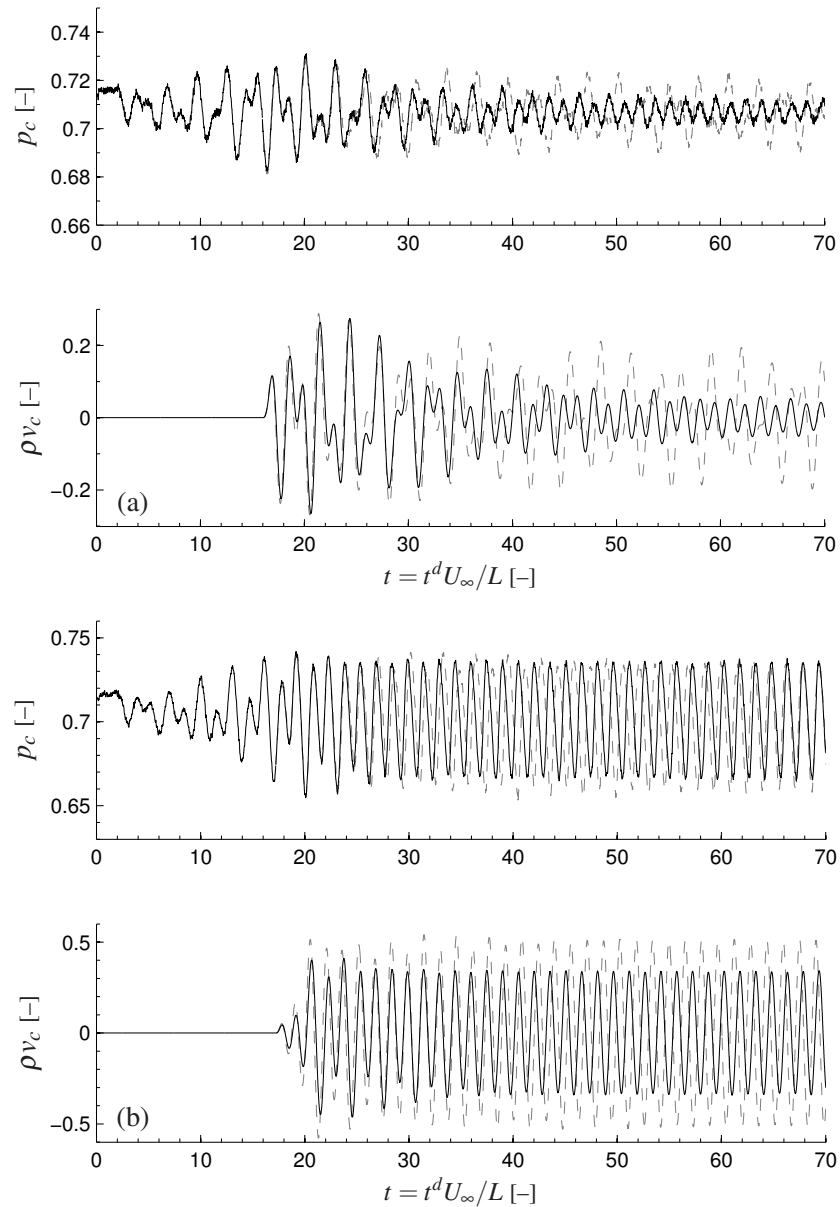


FIGURE 6.8: Performance of the gain-scheduled LQG regulator at off-design Mach numbers: for a free stream Mach number of (a)  $M = 0.7$ ; and (b)  $M = 0.8$ . For both the pressure plots and the body force plots, the original regulator (—) is compared to the gain-scheduled regulator (---).

regulator, despite a larger control body force being provided.

It appears that such a crude form of gain-scheduling is, in fact, too crude. This is perhaps not surprising, since its foundations in Rossiter's formula means that it accounts solely for changes in frequency, and makes no allowance for the changes in growth rates of the modes which will inevitably occur.

These observations provide clear motivation for an adaptive feedback controller, which we look at next.

## 6.5 ADAPTIVE CONTROL

We now look at applying the adaptive controller – developed for combustion oscillations in chapter 3 – to the cavity flow for free stream Mach numbers in the range  $0.40 \leq M \leq 0.80$ . Based on the observations made in § 5.6, we use a collocated control arrangement, so-called because the actuator and pressure sensor are now collocated (see figure 5.13), using which the adaptive controller provides stability at all Mach numbers tested.

With the requirements on  $P_L(s)$  all met using collocated control as shown in § 5.6, we apply the adaptive controller for  $n^* \leq 2$  of § 3.3.1 (equation (3.9)):

$$\begin{aligned}\dot{\mathbf{k}}(t) &= \Gamma \text{sgn}(g_0) p(t) \mathbf{d}_\lambda(t) \\ V(t) &= -\mathbf{k}^T(t) \mathbf{d}(t) - \dot{\mathbf{k}}^T(t) \mathbf{d}_\lambda(t),\end{aligned}$$

(with, as before,  $\mathbf{k} = [k_1 \ k_2]^T$ ,  $\mathbf{d} = [p \ V_z]^T$ ,  $V_z = \frac{V}{s+z_c}$  and  $\mathbf{d}_\lambda = \frac{1}{s+\lambda} \mathbf{d}$ ) to the cavity flow with collocated input and output. The parameter values used for the adaptive controller are  $z_c = 0.3$ ,  $\gamma_1 = 3.0 \times 10^5$ ,  $\gamma_2 = 3.0 \times 10^1$ , and  $\text{sgn}(g_0) = +1$ .

Results of applying the updating rule and control law given by (3.9) to the cavity flow for Mach numbers of 0.40, 0.50, 0.60, 0.70 and 0.80 are shown in figures 6.9–6.13.

To make the adaptive controller's behaviour clear, noise has not been artificially added, although this could be accounted for in the updating rule with a dead-zone like that used in chapter 4 (equation (4.8)). For each Mach number, two pressure signals are plotted: the (collocated) pressure used for feedback control  $p_c$  (see figure 5.13),

and the pressure at probe 3,  $p_3$ , which is included to make comparison with the LQG control results easier, since  $p_3$  was the pressure signal used in that case.

The time scales used are the same as those used in figures 6.5 & 6.6 for LQG control, except for  $M = 0.70$  and  $M = 0.80$ : for these two cases, the adaptation takes longer and therefore the pressure fluctuations take longer to eliminate. Nevertheless, the adaptive controller provides stability at all five Mach numbers. The fixed controller that each of these controllers corresponds to once adaptation has stopped are given in table 6.1.

Although the collocated control arrangement makes the adaptive controller less practical than the LQG regulator, the advantage of adaptive control is clear, with stability provided over the entire Mach number range.

TABLE 6.1: Corresponding fixed controller  $K(s)$  at each of the five Mach numbers.

$M = 0.4$	$M = 0.5$	$M = 0.6$	$M = 0.7$	$M = 0.8$
$25.8 \frac{s + 0.30}{s + 0.36}$	$39.7 \frac{s + 0.30}{s + 0.47}$	$47.4 \frac{s + 0.30}{s + 0.59}$	$34.7 \frac{s + 0.30}{s + 0.47}$	$49.7 \frac{s + 0.30}{s + 0.68}$

## 6.6 CONCLUDING REMARKS

This chapter has built on the linear modeling approach used in chapter 5, and has done so in two ways. First, model reduction using the eigensystem realization algorithm has been used to form a low-order state space model of the cavity flow. Validation of the reduced-order model has been performed in the frequency domain, where its frequency response was compared to that found in chapter 5 using spectral methods. This reduced-order model has been used to design a robust ( $\mathcal{H}_2$ ) feedback controller, which provides stability over a wider Mach number range than seen in previous studies.

Second, by taking advantage of the properties of the cavity flow derived in § 5.5, together with the collocation-based arguments of § 5.6, the adaptive controller of chapter 3 has been applied to the cavity flow. The adaptive controller provides stability over the entire Mach number range, albeit at the cost of a less practical control arrangement.

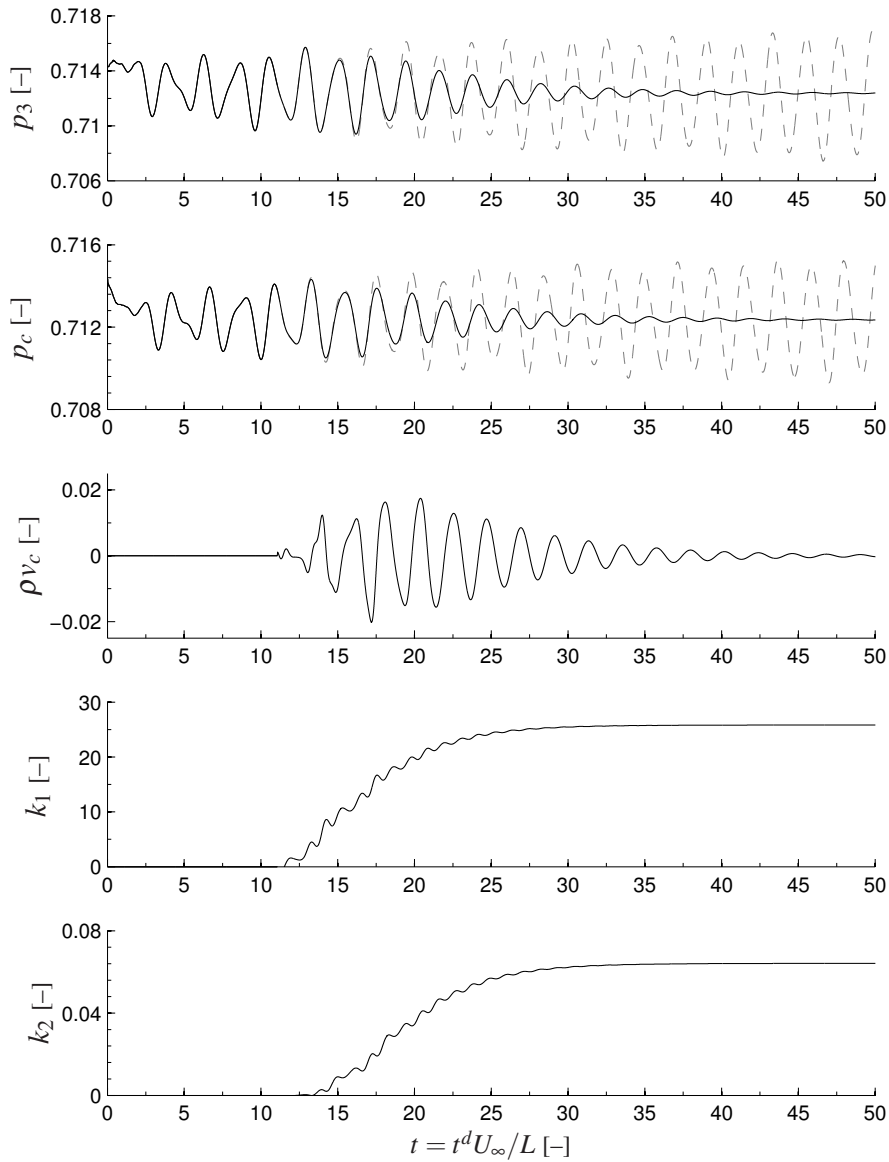
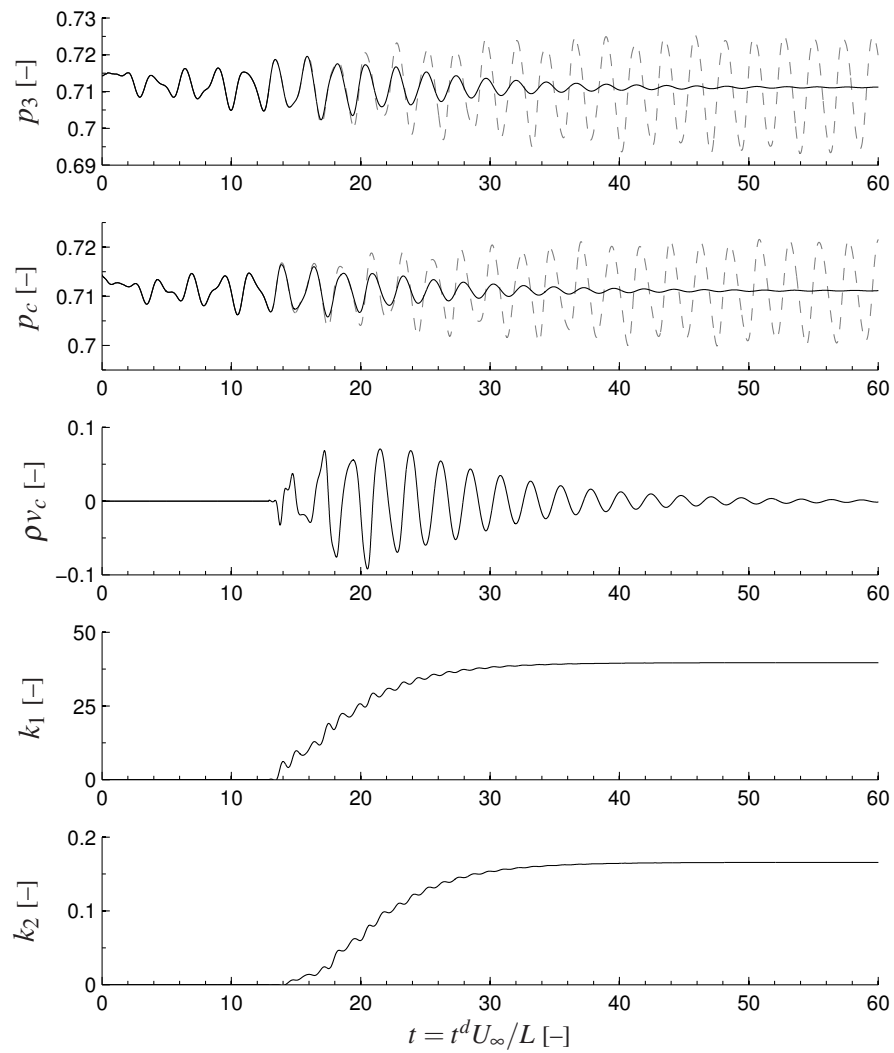
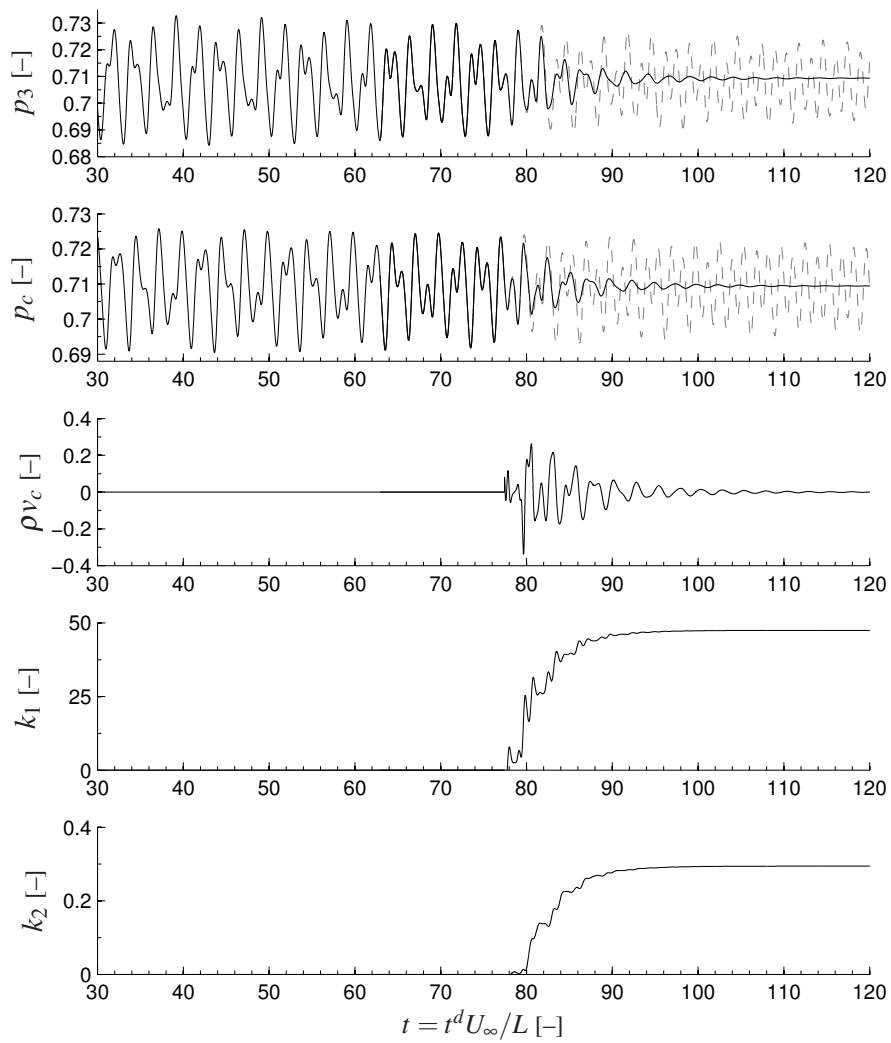
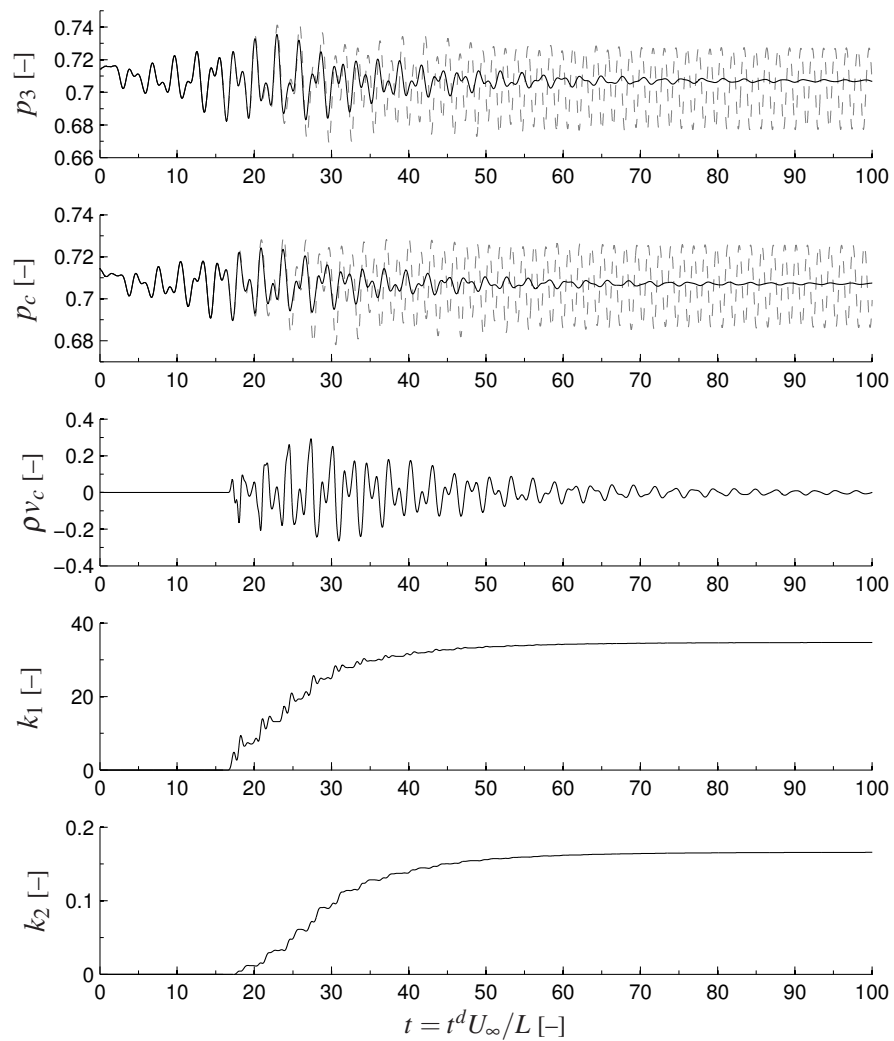
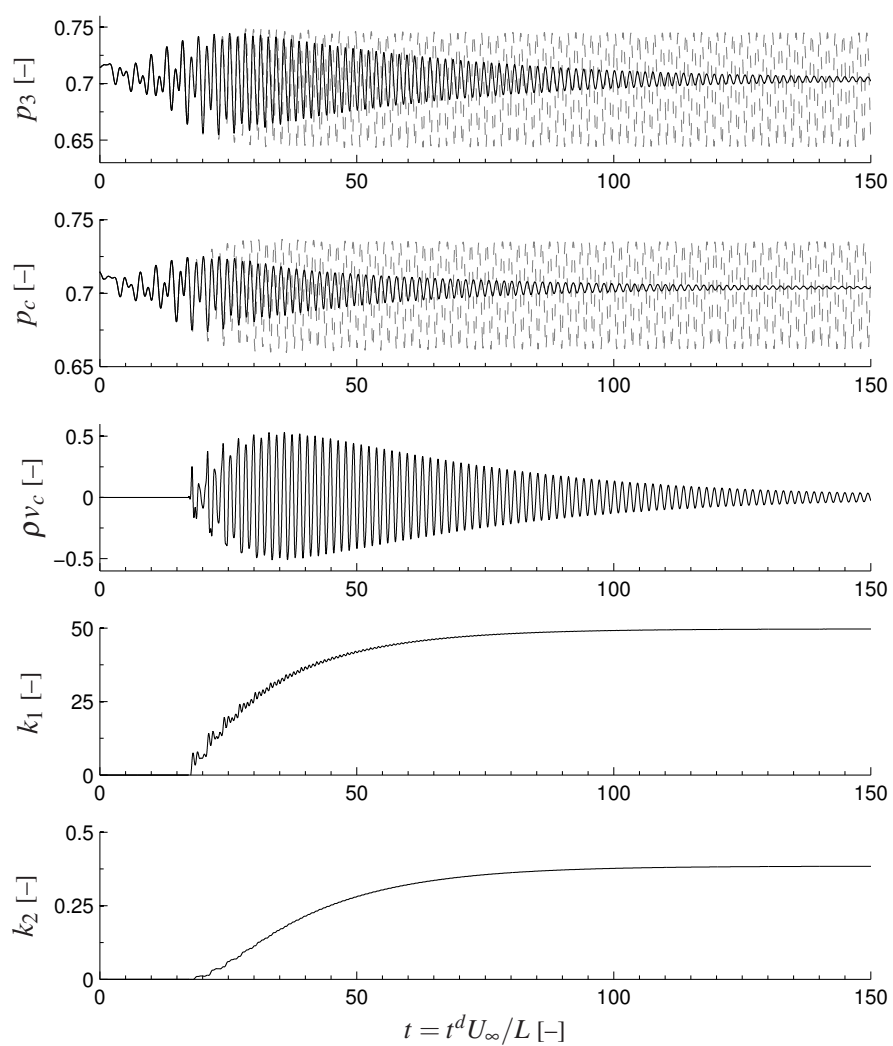


FIGURE 6.9: Adaptive control for  $M = 0.40$ . The top two plots show the pressure measurement at probe 3 and the feedback control pressure measurement  $p_c$  for both the open-loop (---) and closed-loop (—) case; the middle plot shows the control body force; and the bottom two plots show the control parameters  $k_1$  and  $k_2$ .

FIGURE 6.10: Adaptive control for  $M = 0.50$ . Legend same as in figure 6.9.

FIGURE 6.11: Adaptive control for  $M = 0.60$ . Legend same as in figure 6.9.

FIGURE 6.12: Adaptive control for  $M = 0.70$ . Legend same as in figure 6.9.

FIGURE 6.13: Adaptive control for  $M = 0.80$ . Legend same as in figure 6.9.

## CHAPTER 7

### CONCLUSIONS

This chapter contains a summary of the contributions of this thesis, together with some suggestions for future work.

#### 7.1 SUMMARY

The elimination of combustion oscillations using adaptive feedback control has been considered. An adaptive feedback controller for annular combustor geometries has been developed and tested in a low-order thermoacoustic network model called LOTAN. The adaptive controller uses a modal decomposition of the pressure field from a number of azimuthally-spaced pressure transducers for sensing and a number of azimuthally-spaced fuel valves for actuation. The controller stabilizes circumferential modes and longitudinal modes, including the simultaneous control of multiple modes when those modes are uncoupled. Control is maintained following a large change in operating conditions. Finally, the controller still achieves control of a circumferential instability using a reduced number of pressure transducers and fuel valves, which represents a more practicable control arrangement.

One of the requirements of Lyapunov-based adaptive control has then been considered in more detail: that the sign of the high-frequency gain of the open-loop system is known. By using a Nussbaum gain, an adaptive controller that does not require this information has been developed and tested experimentally on a Rijke tube. The Nussbaum gain adaptive controller stabilizes the system, and maintains control following a 13 % change in length of the Rijke tube (which leads to a 10 % change in the

instability's frequency).

Feedback control of a different type of fluid-acoustic resonance has also been considered: the compressible flow past a shallow cavity. First, system identification techniques were used to very accurately determine the cavity's linear dynamics or 'transfer function'. This dynamical model of the cavity – found directly from direct numerical simulations – was then compared to that given by a simple linear model, which models individual components of the cavity physics separately, and which is intended to be useful for feedback control purposes.

Then we looked at using feedback control to eliminate these cavity resonances, and two control strategies were considered. First, standard  $\mathcal{H}_2$  robust control methods – specifically a Linear Quadratic Gaussian regulator – were applied to the cavity flow, the state-space model for which being provided by the Eigensystem Realization Algorithm (ERA). The LQG regulator provides control over a much wider Mach number range than seen previously in the literature. Second, we looked at using the adaptive controller, earlier developed for combustion oscillations, to the cavity flow using collocated control. The adaptive controller achieves closed-loop stability over an even wider Mach number range.

This thesis has considered both robust ( $\mathcal{H}_2$ ) control and adaptive control for stabilizing thermo-acoustic and fluid-acoustic resonances. These two control approaches are distinct, and bring with them their own sets of advantages and inconveniences. Robust control makes no restrictions on the dynamics of the open-loop system, such as the locations of its zeros or its relative degree, and the open-loop system's being observable and controllable is sufficient. This flexibility comes at a price, since an accurate dynamical model of the system must be available, and this can be difficult to obtain, especially for unstable systems. The adaptive controller considered requires no such model of the system, and control can be achieved over a wide range of operating conditions, which has been observed both for combustion systems and for cavity resonances. However, the open-loop system must meet some general properties, and these in themselves can be restrictive: for combustion oscillations, they place demands on the nature of acoustic and entropy disturbances; and for cavity resonances, they could only be met using collocated control.

## 7.2 SUGGESTIONS FOR FUTURE WORK

Although feedback control of combustion oscillations has already been demonstrated at large- and full-scale, most studies involve simple phase-locked loops. It seems, then, that there is scope for more sophisticated controllers – which could include robust and adaptive control – at large- and full-scale, and in particular for annular geometries, allowing the adaptive controller for circumferential modes developed in this thesis to be applied experimentally.

In terms of adaptive control, it seems that it is possible to adaptively stabilize a system without knowledge of the sign of its high-frequency gain, although the controller required to achieve it becomes more complex. The adaptive controller used, though, is slightly at odds with the assumption made earlier in this thesis regarding the relative degree of a general combustion system. For a system with a relative degree not exceeding two, a feedback controller must provide both gain and phase compensation, and yet the Nussbaum gain controller provides only a feedback gain. The development of an adaptive controller which utilizes a Nussbaum-type function and which provides gain and phase compensation would resolve this.

It is encouraging that a simple linear model of cavity resonances can be used to predict the system's transfer function with a reasonable level of success, and which is certainly useful for feedback control purposes. What remains to be seen is whether a feedback controller designed using this simple linear model would be successful in stabilizing the system in direct numerical simulations, and then whether the same strategy could be used to model the system – and therefore to design a model-based controller – at other Mach numbers. The emphasis, as it has been in this thesis, would need to be on providing the information that is important for feedback control. This seems to lend itself to  $\mathcal{H}_\infty$  loop-shaping techniques and to  $v$ -gap metric analysis, which indicates in what sense a model should be accurate if it is to be useful for feedback design (Vinnicombe, 2000).

Finally, it seems that there is still scope for an adaptive controller that is more well-suited to the control of cavity resonances, and which does not rely on collocated control. This could be achieved by further development of the Lyapunov-based adaptive controller, although presumably this will result in a higher-order and therefore

more complex controller. An alternative approach would be to develop a different type of feedback controller which did not rely on any general properties of the open-loop system, and Model Predictive Control (MPC) seems particularly attractive, since it can be applied to systems with many inputs and many outputs; to both linear and non-linear systems; and to systems with constraints (Maciejowski, 2002). MPC has found diverse applications in systems with slow dynamics, in particular in the petrochemical industry. The main barrier to its application to faster processes is the computational burden of the method and therefore its restriction to low sampling frequencies. This constraint is being overcome with more powerful computing capabilities and more efficient optimization algorithms. Of course, such techniques could equally be applied to combustion oscillations, and this seems a promising area for future research.

## APPENDIX A

### GENERAL PROPERTIES OF COMBUSTION SYSTEMS

Here we repeat part of the analysis of Evesque (2000), but consider both longitudinal and circumferential modes. Referring to figure 3.2, for the single-input single-output ( $B = T = 1$ ), longitudinal geometry case, Evesque made some general assumptions about the open-loop transfer function  $P(s)$ . She assumed that the actuator transfer function  $L(s)$  had a relative degree not exceeding two, and that the flame transfer function  $F(s)$  was stable and had limited bandwidth, i.e.

$$\lim_{\omega \rightarrow \infty} F(i\omega) = 0.$$

For the modal open-loop transfer function given by equation (3.2), the actuator transfer function  $L_b(s)$  and the flame transfer function  $F_b(s)$  are both for an individual burner, and so the assumptions on the actuator and the flame are still valid in this case.

Another key part of Evesque's analysis, however, was to use a wave expansion of the acoustic field to characterize the acoustic transfer function  $G(s)$  between the unsteady heat release and the pressure perturbation. By doing so Evesque was able to show that the relative degree of  $P(s)$  was given by the relative degree of the actuator  $L(s)$ , and that all of the zeros of  $G(s)$  (and therefore of  $P(s)$ ) would be in the left half-plane. These results do not necessarily hold for the modal case  $G^n(s)$ , and so we repeat this part of the analysis here, but use a wave expansion that includes circumferential dependence, which is important for the annular geometries of chapter 3.

Figure A.1 shows a general combustion chamber, which could represent a longitudinal geometry, or one half of a circumferential slice through an annular geometry.

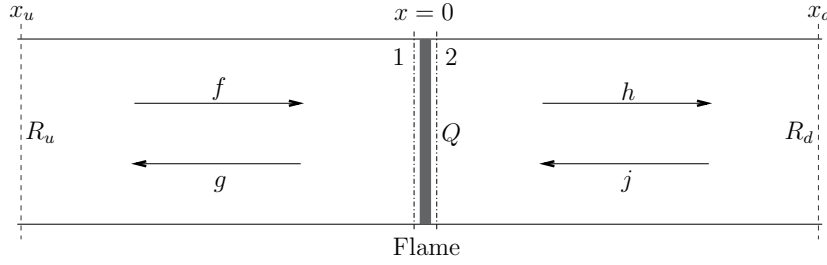


FIGURE A.1: Disturbances in a combustion chamber.

Evesque (2000) looked at the longitudinal case, but we concentrate on the annular case here. Upstream of the flame (zone 1) is a downstream propagating wave  $f$  and an upstream propagating wave  $g$ , and downstream of the flame (zone 2) is a downstream propagating wave  $h$  and an upstream propagating wave  $j$ . For a thin annulus, we can set the radial velocity  $v'$  to zero and ignore radial dependence of the flow parameters. We also assume zero swirl velocity  $w' = 0$ .<sup>1</sup>

We will neglect the conversion of combustion-generated entropy waves into acoustic waves at the downstream nozzle. This will be a good approximation when the time taken for the entropy waves to convect through the duct exceeds their diffusion time. We assume that the reflection coefficients at the upstream and downstream boundaries satisfy  $|R_u(s)| < 1$  and  $|R_d(s)| < 1$ . For linear disturbances, the perturbation in the pressure  $p'$ , density  $\rho'$  and axial velocity  $u'$  are given by (Stow & Dowling, 2001)

$$\begin{aligned} p' &= A_{\pm} e^{i\omega t + ik_{\pm}x + in\theta} \\ \rho' &= \frac{1}{\bar{c}^2} A_{\pm} e^{i\omega t + ik_{\pm}x + in\theta} \\ u' &= -\frac{k_{\pm}}{\bar{\rho}\alpha_{\pm}} A_{\pm} e^{i\omega t + ik_{\pm}x + in\theta}, \end{aligned} \quad (\text{A.1})$$

where  $\bar{c}$  is the mean speed of sound and

$$\bar{c}k_{\pm} = \frac{\bar{M}\omega \mp [\omega^2 - (\frac{\bar{c}n}{R})^2(1 - \bar{M}^2)]^{\frac{1}{2}}}{1 - \bar{M}^2} \quad (\text{A.2a})$$

$$\alpha_{\pm} = \omega + \bar{c}\bar{M}k_{\pm}. \quad (\text{A.2b})$$

<sup>1</sup>Including swirl would not change the equations of conservation of mass, momentum and energy across the flame, but it would change the expression for the wave number.

The + and the – subscripts refer to the  $f, h$  and  $g, j$  waves respectively, depending on which zone the equations are applied to.  $\bar{M}$  is the mean Mach number (assumed to be less than unity) and  $R$  is the mean radius of the annulus. The cut-off frequency  $\omega_c$  is given by

$$\omega_c = \frac{\bar{c}n}{R}(1 - \bar{M}^2)^{\frac{1}{2}},$$

and  $R$  is the combustor radius. For  $\omega < \omega_c$ , the waves decay and mode  $n$  is ‘cut-off’.

The equations of conservation of mass, momentum and energy across the combustion zone can be written in a form independent of downstream density and temperature (Dowling, 1997):

$$\begin{aligned} p_2 - p_1 + \rho_1 u_1 (u_2 - u_1) &= 0 \\ \frac{\gamma}{\gamma - 1} (p_2 u_2 - p_1 u_1) + \frac{1}{2} \rho_1 u_1 (u_2^2 - u_1^2) &= \frac{Q}{A_{\text{comb}}}, \end{aligned}$$

where  $A_{\text{comb}}$  is the cross-sectional area of the combustor. We now set each flow variable to a mean value plus a perturbation ( $u_1 = \bar{u}_1 + u'_1$  for example, with  $\bar{u}_1$  the mean velocity and  $u'_1$  the perturbation). Linearizing these equations, and using the boundary conditions at the upstream and downstream boundaries

$$\begin{aligned} f e^{ik_f x_u} &= R_u g e^{ik_g x_u} \\ j e^{ik_j x_d} &= R_d h e^{ik_h x_d}, \end{aligned}$$

we arrive at a matrix equation in the frequency domain:

$$\begin{bmatrix} X_{11} & X_{12} \\ X_{21} & X_{22} \end{bmatrix} \begin{pmatrix} g \\ h \end{pmatrix} = \begin{bmatrix} Y_{11} & Y_{12} \\ Y_{21} & Y_{22} \end{bmatrix} \begin{pmatrix} R_u g e^{i(k_g - k_f)x_u} \\ R_d h e^{i(k_h - k_j)x_d} \end{pmatrix} + \begin{pmatrix} 0 \\ \frac{Q'}{A_{\text{comb}} \bar{c}_1} \end{pmatrix}. \quad (\text{A.3})$$

The full expressions for the  $X$  and  $Y$  matrices are given in appendix B. Expressed in the time domain, (A.3) would give the time evolution of the outgoing waves  $g(t)$  and  $h(t)$  in terms of the unsteady heat release  $Q'(t)$ . Using (A.3) we can find a frequency-domain expression relating the modal pressure  $p_{\text{ref}}^n$  (at some axial location  $x_{\text{ref}}$ ) to the modal unsteady heat release at the flame  $Q'^n$ . When measuring  $p_{\text{ref}}^n$  downstream of the

flame, we find

$$\begin{aligned}\frac{p_{\text{ref}}^n(s)}{Q^n(s)} &= \frac{[X_{11}(s) - R_u Y_{11}(s) e^{i(k_g - k_f)x_u}] [1 + R_d e^{i(k_h - k_j)(x_d - x_{\text{ref}})}]}{A_{\text{comb}} \bar{C}_1} e^{ik_h x_{\text{ref}}} \\ &= G_0^n(s) e^{ik_h x_{\text{ref}}} \\ &= G^n(s).\end{aligned}\tag{A.4}$$

Giving an expression for  $G^n(s)$  from equation (3.2) as the product of a transfer function  $G_0^n(s)$  and a pure time delay. If the pressure is instead measured upstream of the flame, this becomes

$$\begin{aligned}\frac{p_{\text{ref}}^n(s)}{Q^n(s)} &= \frac{[Y_{12}(s) R_d e^{i(k_h - k_j)x_d} - X_{12}(s)] [1 + R_u e^{i(k_f - k_g)(x_{\text{ref}} - x_u)}]}{A_{\text{comb}} \bar{C}_1} e^{ik_g x_{\text{ref}}} \\ &= G_0^n(s) e^{ik_g x_{\text{ref}}} \\ &= G^n(s).\end{aligned}\tag{A.5}$$

We now concentrate on the upstream-sensing case (A.5). For the longitudinal case ( $n = 0$ ), (A.5) simplifies and the  $X$  and  $Y$  matrices become independent of frequency (see appendix B). By forming a rational approximation to  $G_0^0(s)$  using Padé approximants of its time delays, Evesque showed that, for longitudinal modes

- (i) the relative degree of the overall open-loop transfer function  $P^0(s)$  is equal to the relative degree of the actuator  $L(s)$
- (ii)  $G_0^0(s)$  (and therefore  $P^0(s)$ ) has only left half-plane zeros.

With the additional circumferential dependence of the flow variables, the same Padé approximant technique can be used to find a rational approximation to  $G_0^n(s)$ , and assumption (i) regarding the relative degree of the *modal* open-loop transfer function  $P^n(s)$  can still be made. Assumption (ii) regarding the position of the zeros of  $G_0^n(s)$  is not necessarily met, though, and now we look at this condition in more detail.

We want to show that any zeros of  $G_0^n(s)$  lie in the left half-plane of the Laplace variable  $s = i\omega$ , which is equivalent to their lying in the upper half-plane of the complex

frequency  $\omega$ . For upstream-sensing (A.5), zeros may occur when either

$$|e^{i(k_h - k_j)x_d}| = \frac{|X_{12}(s)|}{|R_d(s)Y_{12}(s)|}, \quad (\text{A.6a})$$

or

$$|e^{i(k_f - k_g)(x_{\text{ref}} - x_u)}| = \frac{1}{|R_u(s)|}. \quad (\text{A.6b})$$

(These conditions are necessary but not sufficient, since the phase of the left hand-side and right hand-side of (A.6a) or (A.6b) must also be equal for a zero to occur.) We will now see that any zeros that lie well above the cut-off frequency  $\omega_c$  (i.e. frequencies for which  $\omega^2 \gg \omega_c^2$ ) must lie in the left half-plane,  $\text{Re}(s) < 0$ .

For frequencies well above cut-off, the  $X$  and  $Y$  matrices simplify to expressions that are independent of frequency (see appendix B), and then  $|X_{12}| > |Y_{12}|$ . Therefore, since  $|R_d(s)| < 1$  and  $|R_u(s)| < 1$  by assumption, a zero can only occur when the magnitude of the exponential term in (A.6a) or (A.6b) is greater than one. Well above cut-off, these two equations become

$$e^{-s\tau_d} = \frac{|X_{12}|}{|R_d(s)Y_{12}|} \quad (\text{A.7a})$$

$$e^{-s\tau_u} = \frac{1}{|R_u(s)|}, \quad (\text{A.7b})$$

where  $\tau_d$  and  $\tau_u$  are acoustic propagation times given by  $\tau_d = 2x_d/(\bar{c}_2(1 - \bar{M}_2^2))$  and  $\tau_u = 2(x_{\text{ref}} - x_u)/(\bar{c}_1(1 - \bar{M}_2^2))$ . Therefore the magnitude of the exponential terms can only be greater than one – and zeros can only occur – in the upper half-plane of  $\omega$ , which corresponds to the left half-plane for the Laplace variable  $s$ . A similar proof can be shown for downstream pressure sensing, if one makes the further assumption that

$$\frac{\bar{u}_2}{\bar{u}_1} \geq \frac{2 - \bar{M}_1}{1 - \bar{M}_1}.$$



## APPENDIX B

### $X$ AND $Y$ MATRICES

Here we collect together the full expressions for the  $X$  and  $Y$  matrices introduced in chapter 2 for two cases: (i) the general case; and (ii) for frequencies well above the cut-off frequency. For simplicity, we drop the over-bar notation for a mean value in the flow parameters  $c$ ,  $M$  and  $u$ , the mean value now being implied.

#### GENERAL CASE

The four terms in the  $X$  matrix introduced in appendix A are

$$\begin{aligned} X_{11}(s) &= -1 + \frac{k_g c_1}{\alpha_g} M_1 \left( 2 - \frac{u_2}{u_1} \right) + M_1^2 \left( \frac{u_2}{u_1} - 1 \right), \\ X_{12}(s) &= 1 - M_2 \frac{k_h c_2}{\alpha_h}, \\ X_{21}(s) &= \frac{\frac{k_g c_1}{\alpha_g} - \gamma M_1}{\gamma - 1} + \frac{k_g c_1}{\alpha_g} M_1^2 + \frac{1}{2} M_1^2 \left( M_1 - \frac{k_g c_1}{\alpha_g} \right) \left( \frac{u_2^2}{u_1^2} - 1 \right), \\ X_{22}(s) &= \frac{c_2}{c_1} \frac{\frac{-k_h c_2}{\alpha_h} + \gamma M_2}{\gamma - 1} - \frac{k_h c_2}{\alpha_h} M_1 M_2 \frac{\rho_1}{\rho_2}, \end{aligned}$$

and the four terms in the  $Y$  matrix are

$$\begin{aligned}
Y_{11}(s) &= 1 - \frac{k_f c_1}{\alpha_f} M_1 \left( 2 - \frac{u_2}{u_1} \right) - M_1^2 \left( \frac{u_2}{u_1} - 1 \right), \\
Y_{12}(s) &= -1 + M_2 \frac{k_j c_2}{\alpha_j}, \\
Y_{21}(s) &= \frac{\frac{-k_f c_1}{\alpha_f} + \gamma M_1}{\gamma - 1} - \frac{k_f c_1}{\alpha_f} M_1^2 - \frac{1}{2} M_1^2 \left( M_1 - \frac{k_f c_1}{\alpha_f} \right) \left( \frac{u_2^2}{u_1^2} - 1 \right), \\
Y_{22}(s) &= \frac{c_2}{c_1} \frac{\frac{k_j c_2}{\alpha_j} + \gamma M_2}{\gamma - 1} + \frac{k_j c_2}{\alpha_j} M_1 M_2 \frac{\rho_1}{\rho_2}.
\end{aligned}$$

#### WELL ABOVE CUT-OFF

For frequencies well above the cut-off frequency  $\omega^2 \gg \omega_c^2$ , the  $X$  and  $Y$  matrices can be approximated by expressions independent of frequency. These are the same expressions that one finds for the longitudinal case, since  $\omega^2 \gg \omega_c^2$  is equivalent to saying that the term  $\frac{\bar{n}}{R} (1 - \bar{M}^2)^{1/2}$  in (A.2a) is negligible. For  $X$  we have

$$\begin{aligned}
X_{11} &= -1 + M_1 \left( 2 - \frac{u_2}{u_1} \right) + M_1^2 \left( \frac{u_2}{u_1} - 1 \right), \\
X_{12} &= 1 + M_2, \\
X_{21} &= \frac{1 - \gamma M_1}{\gamma - 1} + M_1^2 + \frac{1}{2} M_1^2 (M_1 - 1) \left( \frac{u_2^2}{u_1^2} - 1 \right), \\
X_{22} &= \frac{c_2}{c_1} \frac{1 + \gamma M_2}{\gamma - 1} + M_1 M_2 \frac{\rho_1}{\rho_2},
\end{aligned}$$

and for  $Y$

$$\begin{aligned}
Y_{11} &= 1 + M_1 \left( 2 - \frac{u_2}{u_1} \right) - M_1^2 \left( \frac{u_2}{u_1} - 1 \right), \\
Y_{12} &= -1 + M_2, \\
Y_{21} &= \frac{1 + \gamma M_1}{\gamma - 1} + M_1^2 - \frac{1}{2} M_1^2 (M_1 + 1) \left( \frac{u_2^2}{u_1^2} - 1 \right), \\
Y_{22} &= \frac{c_2}{c_1} \frac{1 + \gamma M_2}{\gamma - 1} + M_1 M_2 \frac{\rho_1}{\rho_2}.
\end{aligned}$$

## APPENDIX C

### PROOF OF CLOSED-LOOP STABILITY FOR A NUSSBAUM GAIN

We consider the first order system (4.1). For the more general case of minimum phase,  $n^* = 1$  systems, see Willems & Byrnes (1984). The first order system (4.1) can be written in the time domain as

$$\dot{y}(t) = ay(t) + g_0u(t). \quad (\text{C.1})$$

Suppose the adaptive control law<sup>1</sup>

$$\begin{aligned} \dot{k}(t) &= y^2(t) \\ u(t) &= N(k)y(t) \end{aligned}$$

is used, where  $N(k)$  is the *Nussbaum gain*. The resulting closed-loop system is given by

$$\dot{y}(t) = ay(t) + g_0N(k)y(t) \quad (\text{C.2})$$

$$\dot{k}(t) = y^2(t). \quad (\text{C.3})$$

We want to find a Nussbaum gain that will guarantee closed-loop stability without knowledge of the sign of  $g_0$ . To study the closed-loop stability of the system, we

---

<sup>1</sup>Note the positive feedback convention used here, which is the opposite of that used in chapter 4 (equation (4.3)): the Nussbaum gain is ultimately insensitive to the sign adopted, and we adopt a positive convention for simplicity.

introduce an indicator function,

$$\Lambda(t) = \frac{1}{2}y^2(t). \quad (\text{C.4})$$

Evaluating  $\dot{\Lambda}(t)$  along solutions to (C.2) gives

$$\begin{aligned} \dot{\Lambda}(t) &= y(t)\dot{y}(t) \\ &= \{a + g_0N(k)\}y^2(t) \\ &= \{a + g_0N(k)\}\dot{k}(t) \end{aligned}$$

Integrating over time  $t$  (using  $k(0) = k_0$  and introducing  $\sigma = k(\tau)$ ), we have

$$\int_0^t \dot{\Lambda}(\tau)d\tau = a \int_0^t \dot{k}(\tau)d\tau + g_0 \int_0^t N(\sigma)\dot{k}(\tau)d\tau \quad (\text{C.5})$$

$$= a[k(t) - k_0] + g_0 \int_{k_0}^{k(t)} N(\sigma)d\sigma \quad (\text{C.6})$$

and so

$$\Lambda(t) - \Lambda(0) = [k(t) - k_0] \left\{ a + \frac{g_0}{k(t) - k_0} \int_{k_0}^{k(t)} N(\sigma)d\sigma \right\}. \quad (\text{C.7})$$

Suppose that the Nussbaum gain  $N(\sigma)$  satisfies the two conditions

$$\begin{aligned} \sup_{k > k_0} \frac{1}{k - k_0} \int_{k_0}^k N(\sigma)d\sigma &= \infty \\ \inf_{k > k_0} \frac{1}{k - k_0} \int_{k_0}^k N(\sigma)d\sigma &= -\infty. \end{aligned} \quad (\text{C.8})$$

Seeking a contradiction, suppose that  $k(t) \rightarrow \infty$  as  $t \rightarrow \infty$  (from (C.3),  $k(t)$  is monotone non-decreasing). Since the Nussbaum gain (C.8) takes arbitrarily large positive and negative values as  $k(t) \rightarrow \infty$ , we derive a contradiction at (C.7). Therefore  $k(t)$  must be bounded. From (C.3), this is equivalent to  $y(t) \in \mathcal{L}_2(0, \infty]$ . Then from (C.2)  $\dot{y}(t) \in \mathcal{L}_2(0, \infty]$ . Finally, lemma 2.12, Narendra & Annaswamy (1989) shows that  $y(t)$  is guaranteed to converge asymptotically to zero.

## APPENDIX D

### ADAPTATION RATES FOR THE NUSSBAUM GAIN

The adaptation rates  $\gamma$  and  $\mu$ , introduced into the adaptive controller's updating rule (4.5) and control law (4.6–4.7) in § 4.3.2 are now explained in more detail, together with details of how they are chosen.

#### CHOOSING $\gamma$

Looking at the updating rule (4.5), one can see that  $\gamma$  sets the rate at which  $k$  adapts. Therefore  $\gamma$  can be set by specifying the desired speed of adaptation of  $k$  (Yildiz *et al.*, 2007). If  $k$  starts at zero, this corresponds to  $3\tau_n$  for a 5% band around the set point (where  $\tau_n$  is the period of the unstable mode):

$$\dot{k}(t) = \gamma p^2(t) = \frac{|k^*|}{3\tau_n},$$

and therefore

$$\gamma = \frac{|k^*|}{3\tau_n \hat{p}^2},$$

where  $k^*$  is the value of  $k$  for which closed-loop stability is achieved, and  $\hat{p}$  is a characteristic value of  $p$ . The value of  $k^*$  will depend on whether the Nussbaum gain is initially updated in the right direction. To get around this we assume that the Nussbaum gain is initially updated in the right direction – then  $k^*$  will be similar in size to  $N^*$ , i.e.

$$\gamma = \frac{|N^*|}{3\tau_n \hat{p}^2}.$$

If the Nussbaum gain is instead initially updated in the wrong direction, then this simply means that the controller will take longer to reach  $k^*$  (and therefore  $N^*$ ) and achieve closed-loop stability.

### CHOOSING $\mu$

Looking at the Nussbaum gain used (4.7), one can see that  $\mu$  dictates, via the cosine term, exactly when  $N(k)$  will switch sign. The Nussbaum gain  $N(k)$  provides closed-loop stability by providing a gain that is (i) large enough and (ii) of the right sign. Furthermore,  $N(k)$  only needs to switch sign once (if at all). Therefore it suffices to ensure, via  $\mu$ , that  $N(k)$  sweeps over a sufficiently large gain *before* it switches sign. This will allow the controller to ‘try’ a big enough gain before  $N(k)$  switches sign.

We can ensure that this happens by specifying the turning point of  $N(k)$ , that is by specifying the value of  $N(k)$  at which  $\frac{dN}{dt} = 0$ :

$$\frac{dN}{dt} = \frac{dN}{dk} \frac{dk}{dt} = 0.$$

We already have an expression for  $\frac{dk}{dt}$  (4.5): this is zero when  $p$  is zero. Therefore we are interested in  $\frac{dN}{dk} = 0$ . From (4.7),

$$\frac{dN}{dk} = \cos(\mu|k_t|^{\frac{1}{4}}) - \frac{1}{4}\mu|k_t|^{\frac{1}{4}} \sin(\mu|k_t|^{\frac{1}{4}}) = 0,$$

where  $k_t$  is the  $k$  for which  $\frac{dN}{dk} = 0$ . Letting  $\mu|k_t|^{\frac{1}{4}} = X$ , we have

$$X \tan X = 4,$$

which we can solve for  $X$ . We need two equations for the two unknowns  $\mu$  and  $k_t$ : the second equation comes from specifying  $N_t$ , the value of  $N(k)$  for which  $\frac{dN}{dk} = 0$ , i.e.

$$\begin{aligned} N_t &= N(k) \Big|_{\frac{dN}{dk}=0} = k_t \cos(\mu|k_t|^{\frac{1}{4}}) \\ N_t &= k_t \cos X. \end{aligned}$$

Then  $k_t$  and  $\mu$  can be found using

$$k_t = \frac{N_t}{\cos X}$$
$$\mu = X|k_t|^{-\frac{1}{4}}.$$

Therefore to choose the two adaption rates  $\gamma$  and  $\mu$ , it suffices to have an estimate (to order of magnitude accuracy only) of  $N^*$ ,  $\tau_n$  and  $\hat{p}$ . In addition,  $N_t$  needs to be chosen so that  $N_t > |N^*|$  is guaranteed.



## BIBLIOGRAPHY

- AKAMATSU, S. & DOWLING, A. P. 2001 Three dimensional thermoacoustic oscillation in a premix combustor. *ASME Paper GT-2001-0034*.
- ANNASWAMY, A. M., EL RIFAI, O. M., FLEIFIL, M., HATHOUT, J. P. & GHONIEM, A. F. 1998 A model-based self-tuning controller for thermoacoustic instability. *Combust. Sci. Tech.* **135**, 213–240.
- ANNASWAMY, A. M., FLEIFIL, M., RUMSEY, J. W., PRASANTH, R., HATHOUT, J. & GHONIEM, A. F. 2000 Thermoacoustic instability: model-based optimal control designs and experimental validation. *IEEE Trans. Contr. Syst. Tech.* **8** (6), 905–918.
- ARMITAGE, C. A., RILEY, A. J., CANT, R. S., DOWLING, A. P. & STOW, S. R. 2004 Flame transfer function for swirled LPP combustion from experiments and CFD. *Proc. ASME Turbo Expo 2004*.
- ÅSTRÖM, K. J. 1983 Theory and applications of adaptive control—a survey. *Automatica* **19** (5), 471–486.
- ÅSTRÖM, K. J. 1987 Adaptive feedback control. *Proc. IEEE* **75** (2), 185–217.
- BANASZUK, A., JACOBSON, C. A., Khibnik, A. I. & MEHTA, P. G. 1999 Linear and nonlinear analysis of controlled combustion processes. Part I: Linear analysis. *Proc. IEEE Conf. Contr. Applic.* **1**, 199–205.
- BELLUCCI, V., FLOHR, P., PASCHEREIT, C. O. & MAGNI, F. 2004 On the use of Helmholtz resonators for damping acoustic pulsations in industrial gas turbines. *J. Eng. Gas Turbines Power* **126** (2), 271–275.
- BELLUCCI, V., SCHUERMANS, B., NOWAK, D., FLOHR, P. & PASCHEREIT, C. O. 2005 Thermoacoustic modeling of a gas turbine combustor equipped with acoustic dampers. *J. Turbomachinery* **127** (2), 372–379.
- BILLOUD, G., GALLAND, M. A., HUU, C. H. & CANDEL, S. 1992 Adaptive active control of combustion instabilities. *Combust. Sci. Tech.* **81** (4), 257–283.
- BLAKE, W. K. & POWELL, A. 1986 The development of contemporary views of flow-tone

- generation. In *Recent Advances in Aeroacoustics*, pp. 247–345. Springer-Verlag.
- BLONBOU, R., LAVERDANT, A., ZALESKI, S. & KUENTZMANN, P. 2000 Active control of combustion instabilities on a Rijke tube using neural networks. *Proc. Combust. Inst.* **28** (1), 747–755.
- BLOXSIDGE, G. J., DOWLING, A. P., HOOPER, N. & LANGHORNE, P. J. 1988 Active control of reheat buzz. *AIAA J.* **26** (7), 783–790.
- BRODA, J. C., SEO, S., SANTORO, R. J., SHIRHATTIKAR, G. & YANG, V. 1998 An experimental study of combustion dynamics of a premixed swirl injector. *Proc. Combust. Inst.* **27**, 1849–1856.
- BROUWER, J., AULT, B. A., BOBROW, J. E. & SAMUELSEN, G. S. 1991 Active control for gas turbine combustors. *Proc. Combust. Inst.* **23** (1), 1087–1092.
- CABELL, R. H., KEGERISE, M. A., COX, D. E. & GIBBS, G. P. 2006 Experimental feedback control of flow-induced cavity tones. *AIAA J.* **44** (8), 1807–1815.
- CAMPOS-DELGADO, D. U., SCHUERMANS, B. B. H., ZHOU, K., PASCHEREIT, C. O., GALLESTEY, E. A. & PONCET, A. 2003a Thermoacoustic instabilities: modeling and control. *IEEE Trans. Contr. Syst. Tech.* **11** (4), 429–447.
- CAMPOS-DELGADO, D. U., ZHOU, K., ALLGOOD, D. & ACHARYA, S. 2003b Active control of combustion instabilities using model-based controllers. *Combust. Sci. Tech.* **175** (1), 27–53.
- CANDEL, S. 2002 Combustion dynamics and control: Progress and challenges. *Proc. Combust. Inst.* **29**, 1–28.
- CANDEL, S. M. 1992 Combustion instabilities coupled by pressure waves and their active control. *Proc. Combust. Inst.* **24** (1), 1277–1296.
- CATTAFESTA, L. N., SONG, Q., WILLIAMS, D. R., ROWLEY, C. W. & ALVI, F. S. 2008 Active control of flow-induced cavity oscillations. *Prog. Aerosp. Sci.* **44**, 479–502.
- CHU, B. T. 1964 On the energy transfer to small disturbances in fluid flow (Part I). *Acta Mechanica* **1**, 215–234.
- CHU, Y.-C, GLOVER, K. & DOWLING, A. P. 2003 Control of combustion oscillations via  $\mathcal{H}_\infty$  loop-shaping,  $\mu$ -analysis and integral quadratic constraints. *Automatica* **39** (2), 219–231.
- COHEN, J. M. & BANASZUK, A. 2003 Factors affecting the control of unstable combustors. *J. Prop. Power* **19** (5), 811–821.
- COLONIUS, T. 2001 An overview of simulation, modeling, and active control of flow/acoustic resonance in open cavities. *AIAA Paper 2001–0076*.

- CORREA, S. M. 1998 Power generation and aeropropulsion gas turbines: from combustion science to combustion technology. *Proc. Combust. Inst.* **27**, 1793–1807.
- CROCCO, L. 1965 Theoretical studies on liquid-propellant rocket instability. *Proc. Combust. Inst.* **10**, 1101–1128.
- CROCCO, L. & CHENG, S. 1956 *Theory of Combustion Instability in Liquid Propellant Rocket Motors*. Butterworths Scientific Publications.
- CULICK, F. E. C. 1971 Non-linear growth and limiting amplitude of acoustic oscillations in combustion chambers. *Combust. Sci. Tech.* **3** (1), 1–16.
- DINES, P. J. 1983 Active control of flame noise. PhD thesis, University of Cambridge.
- DOCQUIER, N. & CANDEL, S. 2002 Combustion control and sensors: a review. *Prog. Energy Combust. Sci.* **28** (2), 107–150.
- DORF, R. C. & BISHOP, R. H. 2005 *Modern Control Systems*. Pearson Prentice Hall.
- DOWLING, A. P. 1997 Nonlinear self-excited oscillations of a ducted flame. *J. Fluid Mech.* **346**, 271–290.
- DOWLING, A. P. & FLOWCS WILLIAMS, J. E. 1983 *Sound and Sources of Sound*. Ellis Horwood.
- DOWLING, A. P. & MORGANS, A. S. 2005 Feedback control of combustion oscillations. *Annu. Rev. Fluid Mech.* **37**, 151–182.
- DOWLING, A. P. & STOW, S. R. 2003 Acoustic analysis of gas turbine combustors. *J. Prop. Power* **19** (5), 751–764.
- DUCRUIX, S., SCHULLER, T., DUROX, D. & CANDEL, S. 2003 Combustion dynamics and instabilities: Elementary coupling and driving mechanisms. *J. Prop. Power* **19** (5), 722–734.
- ELDRIDGE, J. D. & DOWLING, A. P. 2003 The absorption of axial acoustic waves by a perforated liner with bias flow. *J. Fluid Mech.* **485**, 307–335.
- EVESQUE, S. 2000 Adaptive control of combustion oscillations. PhD thesis, University of Cambridge.
- EVESQUE, S., ANNASWAMY, A. M., NICULESCU, S. & DOWLING, A. P. 2003a Adaptive control of a class of time-delay systems. *J. Dynam. Syst. Measur. Contr.* **125**, 186–193.
- EVESQUE, S., DOWLING, A. P. & ANNASWAMY, A. M. 2003b Self-tuning regulators for combustion oscillations. *Proc. R. Soc. A* **459** (2035), 1709–1749.
- EVESQUE, S. & POLIFKE, W. 2002 Low-order acoustic modelling for annular combustors: Validation and inclusion of modal coupling. *ASME Paper GT-2002-30064*.
- FLEIFIL, M., ANNASWAMY, A. M., GHONEIM, Z. A. & GHONIEM, A. F. 1996 Response

- of a laminar premixed flame to flow oscillations: A kinematic model and thermoacoustic instability results. *Combust. Flame* **106** (4), 487–510.
- FLEIFIL, M., HATHOUT, J.-P., ANNASWAMY, A. M. & GHONIEM, A. F. 1998 The origin of secondary peaks with active control of thermoacoustic instability. *Combust. Sci. Tech.* **133** (4), 227–265.
- GELBERT, G., MOECK, J. P., BOTHIEN, M. R., KING, R. & PASCHEREIT, C. O. 2008 Model predictive control of thermoacoustic instabilities in a swirl-stabilized combustor. *AIAA Paper 2008-1055*.
- GHARIB, M. 1987 Response of the cavity shear layer oscillations to external forcing. *AIAA J.* **25** (1), 43–47.
- GULATI, A. & MANI, R. 1992 Active control of unsteady combustion-induced oscillations. *J. Prop. Power* **8**, 1109–1115.
- GYSLING, D. L., COPELAND, G. S., MCCORMICK, D. C. & PROSCIA, W. M. 2000 Combustion system damping augmentation with Helmholtz resonators. *J. Eng. Gas Turbines Power* **122** (2), 269–274.
- HARRIS, C. J. & BILLINGS, S. A. 1981 *Self-Tuning and Adaptive Control: Theory and Applications*. Peter Peregrinus.
- HATHOUT, J.-P., ANNASWAMY, A. M., FLEIFIL, M. & GHONIEM, A. F. 1998 A model-based active control design for thermoacoustic instability. *Combust. Sci. Tech.* **132**, 99–138.
- HECKL, M. A. 1988 Active control of the noise from a Rijke tube. *J. Sound Vib.* **124**, 117–33.
- HELLER, H. H. & BLISS, D. B. 1975 The physical mechanism of flow-induced pressure fluctuations in cavities and concepts for their suppression. *AIAA Paper 75-491*.
- HELLER, H. H., HOLMES, D. G. & COVERT, E. E. 1971 Flow-induced pressure oscillations in shallow cavities. *J. Sound Vib.* **18** (4), 545–545.
- HERMANN, J., GLEIS, S. & VORTMEYER, D. 1996 Active instability control (AIC) of spray combustors by modulation of the liquid fuel flow rate. *Combust. Sci. Tech.* **118** (1), 1–25.
- HONG, B.-S., YANG, V. & RAY, A. 2000 Robust feedback control of combustion instability with modeling uncertainty. *Combust. Flame* **120**, 91–106.
- HONG, J. & BERNSTEIN, D. S. 1998 Bode integral constraints, collocation, and spillover in active noise and vibration control. *IEEE Trans. Contr. Syst. Tech.* **6** (1), 111–120.
- HOWE, M. S. 1998 *Acoustics of Fluid-Structure Interactions*. Cambridge University Press.
- ILCHMANN, A. 1999 *Wiley Encyclopedia of Electrical and Electronics Engineering*, vol. 21, chap. Switching Functions, pp. 213–219. Wiley.

- IOANNOU, P. & SUN, J. 1996 *Robust Adaptive Control*. Prentice Hall.
- JOHNSON, C. E., NEUMEIER, Y., NEUMAIER, M., ZINN, B. T., DARLING, D. D. & SATTINGER, S. S. 2001 Demonstration of active control of combustion instabilities on a full-scale gas turbine combustor. *ASME Paper 2001-GT-0519*.
- JUANG, J. N. 1994 *Applied System Identification*. Prentice Hall.
- JUANG, J. N. & PAPPAS, R. S. 1985 Eigensystem realization algorithm for modal parameter identification and model reduction. *J. Guid. Cont. Dyn.* **8** (5), 620–627.
- KEGERISE, M. A., CABELL, R. H. & CATTAFESTA III, L. N. 2007a Real-time feedback control of flow-induced cavity tones—Part 1: Fixed-gain control. *J. Sound Vib.* **307**, 906–923.
- KEGERISE, M. A., CABELL, R. H. & CATTAFESTA III, L. N. 2007b Real-time feedback control of flow-induced cavity tones—Part 2: Adaptive control. *J. Sound Vib.* **307**, 924–940.
- KELLER, J. J. 1995 Thermoacoustic oscillations in combustion chambers of gas turbines. *AIAA J.* **33**, 2280–2287.
- KJÆR, M. A., JOHANSSON, R. & ROBERTSSON, A. 2006 Active control of thermoacoustic oscillation. *IEEE Internat. Confer. Contr. Applic.*, pp. 2480–2485.
- KOOK, H., MONGEAU, L. & FRANCK, M. A. 2002 Active control of pressure fluctuations due to flow over Helmholtz resonators. *J. Sound Vib.* **255** (1), 61–76.
- KRISHNAMURTY, K. 1956 Sound radiation from surface cutouts in high speed flow. PhD thesis, California Institute of Technology.
- KRSTIC, M., KRUPADANAM, A. & JACOBSON, C. 1999 Self-tuning control of a nonlinear model of combustion instabilities. *IEEE Trans. Contr. Syst. Tech.* **7** (4), 424–436.
- LANDAU, L. D. & LIFSHITZ, E. M. 1959 *Fluid Mechanics*. Pergamon Press.
- LANG, W., POINSOT, T. & CANDEL, S. 1987 Active control of combustion instability. *Combust. Flame* **70** (3), 281–289.
- LANGHORNE, P. J., DOWLING, A. P. & HOOPER, N. 1990 A practical active control system for combustion oscillations. *J. Prop. Power* **6** (3), 324–333.
- LIEUWEN, T., NEUMEIER, Y. & ZINN, B. T. 1998 The role of unmixedness and chemical kinetics in driving combustion instabilities in lean premixed combustors. *Combust. Sci. Tech.* **135**, 193–211.
- LIEUWEN, T. & ZINN, B. T. 1998 The role of equivalence ratio oscillations in driving combustion instabilities in low NO<sub>x</sub> gas turbines. *Proc. Combust. Inst.* **27**, 1809–1816.
- LIU, G. P. & DALEY, S. 1999 Output-model-based predictive control of unstable combustion

- systems using neural networks. *Contr. Eng. Pract.* **7** (5), 591–600.
- LUMLEY, J. L. 1970 *Stochastic Tools in Turbulence*. Academic Press.
- MA, Z., AHUJA, S. & ROWLEY, C. W. 2009 Reduced order models for control of fluids using the Eigensystem Realization Algorithm. *Theor. Comp. Fluid Mech.* (submitted).
- MACIEJOWSKI, J. M. 2002 *Predictive Control with Constraints*. Prentice Hall.
- MATVEEV, K. 2003 Thermoacoustic instabilities in the Rijke tube: experiments and modeling. PhD thesis, California Institute of Technology.
- MCMANUS, K. R., POINSOT, T. & CANDEL, S. M. 1993 A review of active control of combustion instabilities. *Prog. Energy Combust. Sci.* **19** (1), 1–29.
- MCMANUS, K. R., VANDSBURGER, U. & BOWMAN, C. T. 1990 Combustor performance enhancement through direct shear layer excitation. *Combust. Flame* **82** (1), 75–92.
- MOORE, B. C. 1981 Principal component analysis in linear systems: controllability, observability, and model reduction. *IEEE Trans. Automat. Contr.* **26** (1), 17–32.
- MORAN, A. J., STEELE, D. & DOWLING, A. P. 2000 Active control of combustion and its applications. *Proc. RTO AVT Symp. Active Control Tech. Enhanced Performance Operational Capabilities of Military Aircraft, Land Vehicles Sea Vehicles*.
- MORGANS, A. S. & ANNASWAMY, A. M. 2008 Adaptive control of combustion instabilities for combustion systems with right-half plane zeros. *Combust. Sci. Tech.* **180** (9), 1549–1571.
- MORGANS, A. S. & DOWLING, A. P. 2007 Model-based control of combustion instabilities. *J. Sound Vib.* **299**, 261–282.
- MORGANS, A. S. & STOW, S. R. 2007 Model-based control of combustion instabilities in annular combustors. *Combust. Flame* **150**, 380–399.
- MORSE, A. S. 1983 Recent problems in parameter adaptive control. *Outils et Modèles Mathématiques pour l'Automatique, l'Analyse de Systèmes et le Traitement du Signal* **3**, 733–740.
- MURUGAPPAN, S., ACHARYA, S., ALLGOOD, D. C., PARK, S., ANNASWAMY, A. M. & GHONIEM, A. F. 2003 Optimal control of a swirl-stabilized spray combustor using system identification approach. *Combust. Sci. Tech.* **175** (1), 55–81.
- NARENDRA, K. S. & ANNASWAMY, A. M. 1989 *Stable Adaptive Systems*. Dover Publications.
- NEUMEIER, Y. & ZINN, B. T. 1996 Experimental demonstration of active control of combustion instabilities using real-time modes observation and secondary fuel injection. *Proc. Combust. Inst.* pp. 2811–2818.
- NIEDERBERGER, A. S. P., GUZZELLA, L., FRITSCH, D. & BOULOUCHOS, K. 2009 Ther-

- moacoustic instability suppression by gain-delay and  $\mathcal{H}_\infty$  controllers designed for secondary fuel injection. *IEEE Trans. Contr. Syst. Tech.* **17** (5), 1028–1042.
- NOIRAY, N., DUROX, D., SCHULLER, T. & CANDEL, S. 2008 A unified framework for nonlinear combustion instability analysis based on the flame describing function. *J. Fluid Mech.* **615** (1), 139–167.
- NUSSBAUM, R. D. 1983 Some remarks on a conjecture in parameter adaptive control. *Syst. Contr. Letters* **3** (5), 243–246.
- PASCHEREIT, C. O., GUTMARK, E. & WEISENSTEIN, W. 1998 Structure and control of thermoacoustic instabilities in a gas-turbine combustor. *Combust. Sci. Tech.* **138**, 213–232.
- POINSOT, T., BOURIENNE, F., CANDEL, S., ESPOSITO, E. & LANG, W. 1989 Suppression of combustion instabilities by active control. *J. Prop. Power* **5** (1), 14–20.
- POWELL, A. 1953 On edge tones and associated phenomena. *Acustica* **3**, 233–243.
- PRASANTH, R. K., ANNASWAMY, A. M., HATHOUT, J. P. & GHONIEM, A. F. 2002 When do open-loop strategies for combustion control work? *J. Prop. Power* **18** (3), 658–668.
- RAYLEIGH, J. W. S. 1945 *The Theory of Sound*. Macmillan and Co.
- RICHARDS, G. A. & JANUS, M. C. 1998 Characterization of oscillations during premix gas turbine combustion. *J. Eng. Gas Turbines Power* **120** (2), 294–302.
- RICHARDS, G. A., YIP, M. J., ROBEY, E., COWELL, L. & RAWLINS, D. 1997 Combustion oscillation control by cyclic fuel injection. *J. Eng. Gas Turbines Power* **119** (2), 340–343.
- RILEY, A. J., PARK, S., DOWLING, A. P., EVESQUE, S. & ANNASWAMY, A. M. 2004 Advanced closed-loop control on an atmospheric gaseous lean-premixed combustor. *J. Eng. Gas Turbines Power* **126**.
- ROCKWELL, D. & NAUDASCHER, E. 1978 Review—self-sustaining oscillations of flow past cavities. *J. Fluids Eng.* **100**, 152–165.
- ROSHKO, A. 1955 Some measurements of flow in a rectangular cutout. *Tech. Rep.*. NACA TN 3488.
- ROSSITER, J. E. 1964 Wind-tunnel experiments on the flow over rectangular cavities at subsonic and transonic speeds. *Aeronaut. Research Council Reports & Memoranda, No. 3438*.
- ROWLEY, C. W. 2001 Modeling, simulation, and control of cavity flow oscillations. PhD thesis, California Institute of Technology.
- ROWLEY, C. W. 2005 Model reduction for fluids, using balanced proper orthogonal decomposition. *Int. J. Bifurc. Chaos* **15** (3), 997–1013.
- ROWLEY, C. W., COLONIUS, T. & BASU, A. J. 2002 On self-sustained oscillations in two-

- dimensional compressible flow over rectangular cavities. *J. Fluid Mech.* **455**, 315–346.
- ROWLEY, C. W. & JUTTIJUDATA, V. 2005 Model-based control and estimation of cavity flow oscillations. *44th IEEE Confer. Decis. Contr.* **15**, 512–517.
- ROWLEY, C. W., WILLIAMS, D. R., COLONIUS, T., MURRAY, R. M. & MACMYNOWSKI, D. G. 2006 Linear models for control of cavity flow oscillations. *J. Fluid Mech.* **547**, 317–330.
- SAMIMY, M., DEBIASI, M., CARABALLO, E., SERRANI, A., YUAN, X., LITTLE, J. & MYATT, J. H. 2007 Feedback control of subsonic cavity flows using reduced-order models. *J. Fluid Mech.* **579**, 315–346.
- SARNO, R. L. & FRANKE, M. E. 1994 Suppression of flow-induced pressure oscillations in cavities. *J. Aircr.* **31** (1), 90–96.
- SAROHIA, V. & MASSIER, P. F. 1977 Control of cavity noise. *J. Aircr.* **14** (9), 833–837.
- SATTINGER, S. S., NEUMEIER, Y., NABI, A., ZINN, B. T., AMOS, D. J. & DARLING, D. D. 2000 Sub-scale demonstration of the active feedback control of gas-turbine combustion instabilities. *J. Eng. Gas Turbines Power* **122** (2), 262–268.
- SCHUERMANS, B. 2003 Modeling and control of thermoacoustic instabilities. PhD thesis, Ecole Polytechnique Fédérale de Lausanne.
- SEUME, J. R., VORTMEYER, N., KRAUSE, W., HERMANN, J., HANTSCHK, C.-C., ZANGL, P., GLEIS, S., VORTMEYER, D. & ORTHMANN, A. 1998 Application of active combustion instability control to a heavy duty gas turbine. *J. Eng. Gas Turbines Power* **120** (4), 721–726.
- SHAW, L. & NORTHCRAFT, S. 1999 Closed loop active control for cavity acoustics. *AIAA Paper 99–1902*.
- SIROVICH, L. 1987 Turbulence and the dynamics of coherent structures, Parts I–III. *Q. Appl. Math.* **45**, 561–590.
- SMITH, OTTO J. M. 1959 A controller to overcome dead time. *ISA J.* **6** (2), 28–33.
- STANEK, M. J., RAMAN, G., KIBENS, V., ROSS, J. A., ODEDRA, J. & PETO, J. W. 2000 Control of cavity resonance through very high frequency forcing. *AIAA Paper 2000-1905*.
- STEELE, R. C., COWELL, L. H., CANNON, S. M. & SMITH, C. E. 2000 Passive control of combustion instability in lean premixed combustors. *J. Eng. Gas Turbines Power* **122** (3), 412–419.
- STOW, S. R. & DOWLING, A. P. 2001 Thermoacoustic oscillations in an annular combustor. *Proc. ASME Turbo Expo 2001*.
- STOW, S. R. & DOWLING, A. P. 2004 Low-order modelling of thermoacoustic limit cycles.

- ASME Paper GT-2004-54245.*
- STOW, S. R. & DOWLING, A. P. 2009 A time-domain network model for nonlinear thermoacoustic oscillations. *J. Eng. Gas Turbines Power* **131** (3).
- STOW, S. R., DOWLING, A. P. & HYNES, T. P. 2002 Reflection of circumferential modes in a choked nozzle. *J. Fluid Mech.* **467**, 215–239.
- TACHIBANA, S., ZIMMER, L., KUROSAWA, Y. & SUZUKI, K. 2007 Active control of combustion oscillations in a lean premixed combustor by secondary fuel injection coupling with chemiluminescence imaging technique. *Proc. Combust. Inst.* **31** (2), 3225–3233.
- TIERNO, J. E. & DOYLE, J. C. 1992 Multi mode active stabilization of a Rijke tube. *Active Control of Noise and Vibration, 1992: presented at the ASME Winter Annual Meet.*, vol. DSC-Vol. 38.
- TSIEN, H. S. 1952 Servo-stabilization of combustion in rocket motors. *J. Am. Rocket Soc.* **22**, 256–263.
- VINNICOMBE, G. 2000 *Uncertainty and Feedback:  $\mathcal{H}_\infty$  loop-shaping and the  $v$ -gap metric.* Imperial College Press.
- WILLEMS, J. C. & BYRNES, C. I. 1984 Global adaptive stabilization in the absence of information on the sign of the high frequency gain. *Lect. Notes Control. Inform. Sci.* **62**, 49–57.
- WILLIAMS, D. R., FABRIS, D. & MORROW, J. 2000 Experiments on controlling multiple acoustic modes in cavities. *AIAA Paper 2000–1903.*
- YAN, P., DEBIASI, M., YUAN, X., LITTLE, J., ÖZBAY, H. & SAMIMY, M. 2006 Experimental study of linear closed-loop control of subsonic cavity flow. *AIAA J.* **44** (5), 929–938.
- YILDIZ, Y., ANNASWAMY, A. M., YANAKIEV, D. & KOLMANOVSKY, I. 2007 Adaptive idle speed control for internal combustion engines. *Am. Contr. Confer.*, pp. 3700–3705.
- ZHOU, K. & DOYLE, J. C. 1998 *Essentials of Robust Control.* Prentice Hall.